Size-dependent magnetic properties of $LaCoO_3$ and $La_{1-x}Sr_xMnO_3$ nanoparticles

Zur Erlangung des akademischen Grades eines

DOKTORS DER NATURWISSENSCHAFTEN

von der Fakultät für Physik am

Karlsruher Institut für Technologie (KIT)

genehmigte

DISSERTATION

von

Cornelia E. Hintze

aus München

Tag der mündlichen Prüfung: 30. Juni 2017

Referent: Prof. Dr. Hilbert von Löhneysen
Koreferentin: Prof. Dr. Annie Powell

Erklärung zur Selbstständigkeit

Ich versichere, dass ich diese Arbeit selbstständig verfasst habe und keine anderen als die angegebenen Quellen und Hilfsmittel benutzt habe, die wörtlich oder inhaltlich übernommenen Stellen als solche kenntlich gemacht und die Satzung des KIT zur Sicherung guter wissenschaftlicher Praxis in der gültigen Fassung vom 17.05.2010 beachtet habe.

Karlsruhe, den 14. Juni 2017, _____

Cornelia E Hintze

Abstract

Systematic studies of perovskite nanoparticles require several batches of preferably monodisperse, single-crystal nanoparticles of different sizes with comparable crystal quality and oxygen stoichiometry. The microemulsion method resulting in control of the nanoparticle size by adjusting the water-to-surfactant ratio makes it possible to obtain batches of differently sized nanoparticles while using identical calcination conditions. The resulting batches were used to study the size-dependent magnetic properties of $LaCoO_3$ and $La_{1-x}Sr_xMnO_3$ nanoparticles. In both materials reducing the nanoparticle size increases the unit-cell volume and the metal-oxygen bond length. This increase scales linearly with the surface-to-volume ratio, and is most likely related to surface adsorption of water. As the adsorbate binding energy seems to depend both on the transition-metal ion and its valence, the expansion is larger in $La_{1-x}Sr_xMnO_3$ than in $LaCoO_3$. By decreasing the crystal field splitting for Co^{3+}, the elongation of the cobalt-oxygen bond length stabilizes the magnetic high-spin (HS) state (S=2). As a consequence, the average magnetic moment of $LaCoO_3$ increases linearly with increasing surface-to-volume ratio. The Co^{3+} HS concentration is too low to establish long-range ferromagnetic order, and the nanoparticles behave paramagnetically. In $La_{1-x}Sr_xMnO_3$ nanoparticles, the increase of the Mn-O bond length and decrease of the Mn-O-Mn bond angle weakens the double-exchange coupling and hence reduces the ferromagnetic ordering temperature T_C. T_C is reduced further by the intrinsic finite-size effect. The observed size-induced changes of magnetic properties may allow for a controlled manipulation of magnetism in $LaCoO_3$ and $La_{1-x}Sr_xMnO_3$ nanoparticles by varying the particle size.

Zusammenfassung

Systematische Untersuchungen an Perowskit-Nanopartikeln erfordern mehrere Chargen von möglichst monodispersen, einkristallinen Nanopartikeln unterschiedlicher Größe, aber mit vergleichbarer Kristallgüte und Sauerstoffstöchiometrie. Durch die Mikroemulsionssynthese ist es möglich, die Nanopartikelgröße durch das Wasser/Tensid-Verhältnis zu regeln. Somit können Chargen mit unterschiedlicher Partikelgröße unter gleichen Kalzinierungsbedingungen entstehen. Anhand der so hergestellten Chargen wurden die magnetischen Eigenschaften von $LaCoO_3$ und $La_{1-x}Sr_xMnO_3$ Nanopartikeln untersucht. In beiden Materialien führt die Reduzierung der Nanopartikelgröße zu einer Vergrößerung der Einheitszelle und einer Verlängerung der Übergangsmetall-Sauerstoff-Bindungslänge. Diese Veränderungen skalieren linear mit dem Oberfläche/Volumen-Verhältnis (S/V) und sind wahrscheinlich eine Konsequenz von Wasseradsorption an der Oberfläche. Da die Bindungsenergie der Adsorbate sowohl vom Übergangsmetallion als auch dessen Valenz abhängig ist, dehnt sich das Kristallgitter in $La_{1-x}Sr_xMnO_3$ stärker aus als in $LaCoO_3$. Durch Verringerung der Kristallfeldaufspaltung am Co^{3+} ion führt die Vergrößerung des Kobalt-Sauerstoff-Abstands zur Stabilisierung des High-Spin-Zustandes (HS, S=2). Demzufolge steigt das magnetische Moment in $LaCoO_3$ linear mit S/V an. Im Gegensatz zu Studien an dünnen Schichten von $LaCoO_3$ [1] ist die Co^{3+}-HS-Konzentration in Nanopartikeln zu gering, um langreichweitige ferromagnetische Ordnung zu etablieren, und die Nanopartikel zeigen paramagnetische Verhalten. In $La_{1-x}Sr_xMnO_3$ Nanopartikeln schwächt die Verlängerung der Mn-O-Bindungslänge und Verringerung des Mn-O-Mn-Bindungswinkels den Doppelaustausch und reduziert somit die ferromagnetische Ordnungstemperatur T_C. T_C wird weiter verringert durch den intrinsischen finite-size-Effekt. The beobachteten größeninduzierten Änderungen der magnetischen Eigenschaften könnten die kontrollierte Veränderung der magnetischen Eigenschaften in $LaCoO_3$- und $La_{1-x}Sr_xMnO_3$-Nanopartikeln gewährleisten.

Contents

List of Figures

List of Tables

1 Introduction

1.1 Motivation

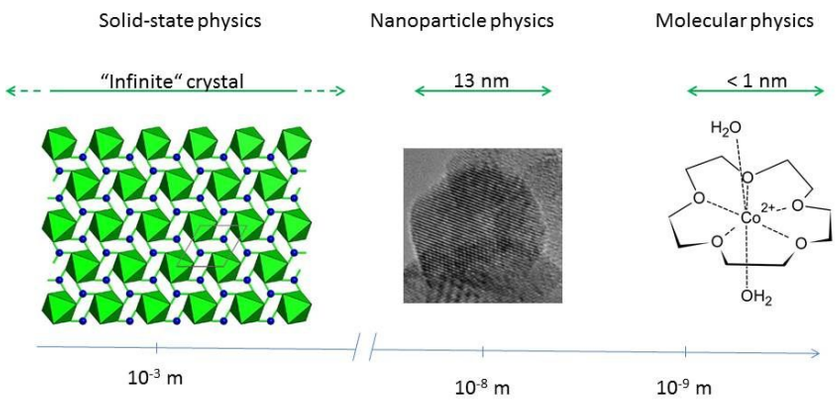

Figure 1.1: Whereas large single crystals can be well described by solid-state physics assuming an infinite periodicity, and molecules such as this cobalt complex are well understood in the framework of molecular physics discussing individual atoms, the physics of nanoparticles can be different from either [2].

Nanoparticles often exhibit properties different from bulk material of the same composition, because their size is too small to show the properties of an "infinite" crystal (see Fig. 1.1). Firstly, it has to be kept in mind that nanoparticle synthesis often requires soft synthesis conditions (i.e. moderate tempratures), which tend to produce more defective crystals than high-temperature crystal growth. If synthesis-related effects can be ruled out, reducing the size of a crystal to nanoparticles (i.e. all three dimensions $\leq$ 100 nm) changes the physical properties by two main mechanisms: firstly the crystallite size may approach the length scale of correlations and, secondly, as the number of atoms at the surface increases with respect to the number of atoms in bulk, the properties of the surface will have a stronger influence. The two effects will be briefly discussed.

1.1.1 Decrease of crystallite size

Miniaturisation can intrinsically alter electronic and magnetic properties. According to Landau theory of ferromagnetism, the spin correlation length ξ diverges as the temperature approaches the Curie temperature T_C following $\xi = |T - T_C|^{-\nu}$, where ν is a critical exponent [3, pp.131–133]. Once the crystal dimensions become smaller than

the correlation length close to T_C, T_C is suppressed to lower temperatures according to $1 - T_{C,n}/T_{C,b} \propto s^{\zeta}$, where $T_{C,n}$ and $T_{C,b}$ are the Curie temperatures of the nanoparticle sample and the bulk material, respectively, and s is the nanoparticle size [4]. The exponent ζ was found to be 1 for $La_{0.67}Ca_{0.3}MnO_3$ [5] and $La_{0.7}Sr_{0.3}CoO_3$ thin films [6].

The reduced size of nanoparticles (NPs) can lead to additional effects: The small volume of nanocrystals changes the energy balance, which can lead to effects governed by kinetics such as superparamagnetism: If long-range ferromagnetism is established in nanoparticles with a size less than 100 nm, the cost of energy to maintain a domain wall is higher than the energy due to demagnetizing fields if all of the nanoparticle ions have aligned spins. Therefore, nanoparticles tend to be single-domain structures and no coercivity is observed. However, superparamagnetism (SPM) can be established at small sizes. The nanoparticle then behaves as one single macrospin, resulting in paramagnetic behaviour with large magnetic moment, exceeding the single-atom moment by up to four orders of magnitude [3, p.297]. The energy barrier to spin flip, ΔE, becomes comparable to the thermal energy $k_B T$, and the macrospin-flip time τ follows an Arrhenius-type of activation law [7], being a product of the attempt frequency τ_0^{-1}, which depends on temperature, saturation magnetization, gyromagnetic ratio, energy barrier, and the damping constant [7], and the probability of having high enough thermal energy [3, pp. 296–298]:

$$\tau = \tau_0 \exp\left(\frac{\Delta E}{k_B T}\right) \tag{1.1}$$

If the temperature drops below the so-called blocking temperature T_B, the magnetic relaxation slows down and the magnetic response changes. T_B is defined as:

$$T_B = \frac{\Delta E}{k_B \ln(\frac{\tau_m}{\tau_0})} \tag{1.2}$$

where τ_m is the time scale of the experiment [8]. The energy barrier ΔE is defined as $\Delta E = KV$, with K the magnetic anisotropy constant and V the volume of the nanoparticle. Consequently, the blocking temperature $T_B \propto V$, for a given material with fixed magnetic anisotropy constant K. Here, spherical particles are assumed and hence shape anisotropy can be neglected.

In the blocked state, $\tau_m \ll \tau$ or $T \leq T_B$, the time between flips is large with respect to the measurement time. Therefore, the particles are in a well defined state. On the other hand, in the superparamagnetic regime, where $\tau_m \gg \tau$ or $T \geq T_B$, the fluctuating state results in zero net moment in the absence of an external field. As soon as an external magnetic field is switched on, the ensemble behaves as a paramagnet, but with a much larger moment, up to temperatures of the order of the Curie temperature T_C, above which it becomes just a normal paramagnet.

1.1.2 Increase of the surface-to-volume ratio

Apart from the reduced size of the crystal volume, NPs also have a significant fraction of atoms located on the nanoparticle surface, where they are no longer coordinated in the

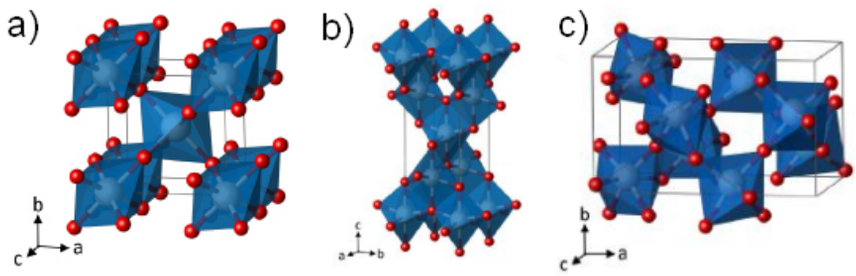

Figure 1.2: a) Rutile b) anatase and c) brookite crystal structures of TiO_2 with O^{2+} ions in red and Ti^{4+} ions inside the octahedra.

same way as atoms in the centre of the particle. In general, the large surface-to-volume ratio of NPs (S/V) results in reduced coordination of metal ions at the surface, which can lead to an increase of the unit-cell volume in oxide nanoparticles [9, 10]. Nanoparticle surfaces can be strained, i.e. the inter-atomic distances are larger than in the bulk, due to the small size [11, 12] and the strain can induce oxygen deficiency [13–16] or chemical segregation [17].

Ferromagnetic long-range order can equally be influenced by S/V. Firstly, the magnetic couplings at the surface of NPs can be highly frustrated and hence form a ferromagnetically dead layer or a spin-glass state, reducing the magnetic moment with decreasing particle size [7, 10, 18, 19]. On the other hand, the reduction of the number of nearest neighbours at the surface may lead to a decrease of the band width and hence to magnetic order. For instance, ferromagnetism has been shown for NiO nanoparticles [20], as well as metallic clusters [7, 21, 22]. In antiferromagnetic NiO, the surface becomes ferromagnetic due to reduced coordination, and changes in the crystal structure, mostly in the rhombohedral distortion and lattice strain, leading to an increase of the sublattice spin order. The reason for nanoparticle ferromagnetism in nominally non-magnetic metals is not yet fully understood, but could be an effect of surface coordination, too [23], or a consequence of reduction of the dimensionality [21, 22].

In the simplest assumption, the surface can be created by splitting the crystal along the bonds: for the surface atoms this means missing partners after the split. The unsaturated – dangling – bonds are responsible for high surface energy, which influences structural, electronic and magnetic properties. Despite surface reconstruction, the free energy of the surface $\gamma_S A$ remains higher than the free energy of the bulk. Ref. [10, p.41] therefore suggests to add a surface term to the Gibb's free energy G:

$$G = H - TS - \gamma_S A \tag{1.3}$$

where H, T and S are the enthalpy, temperature and entropy, respectively. With A the surface per mol and γ_S the surface energy – taking surface reconstruction into account –, the importance of the surface in thermodyanmic considerations of nanoparticles becomes clear. Most prominently, TiO_2 nanoparticles have been shown to exhibit stable structural phases (anatase and brookite) that are unstable for bulk TiO_2 (see Fig. 1.2). This is related to the fact that anatase and brookite have higher bulk enthalpies H, but lower

surface energies $\gamma_S A$ than the bulk stable phase rutile [24, 25]. Since the surface becomes dominant at small sizes, the overall energy of the system can be lowered by adopting a structural phase with a higher bulk enthalpy H, balanced against reduced surface energy. At the nanoscale, the most stable structure with the lowest free energy can therefore be the one with higher bulk enthalpy but lower surface energy.

Simulations tend to consider clean surfaces, but in reality, the broken bonds of the atoms at the surface are saturated, e.g. by hydroxides, which changes the value of γ_S in Equation 1.3. Depending on the surface-to-volume ratio (S/V), this hydroxide layer can contribute to the electronic properties as well as change the crystal structure, e.g. stretching the interatomic bonds. Adsorbates or surface-specific defects can influence the properties significantly. In transition-metal oxides, for example, the surface tends to be slightly oxygen deficient, which can influence the lattice structure [26, 27]. Via the surface energy γ_S adsorption can crucially affect the question whether the crystal lattice will expand or contract [28, 29]. In polycrystalline NPs strains at the grain boundaries may also affect structural and therefore magnetic properties [30].

As the crystal structure largely determines the physical properties of the material, the increase of S/V can lead to a modification of physical properties indirectly via lattice changes. These changes in the crystal lattice may include uniform expansion of the unit cell [9], modification of the ratio of the unit-cell c-axis length to a-axis length [31] or complete phase transitions as in TiO_2 mentioned above.

In the present thesis, nanoparticles of two systems with perovskite crystal structure will be investigated, whose bulk properties are well documented. The first material studied is $LaCoO_3$, which at low temperatures is non-magnetic in bulk form since Co^{3+} is in the low spin (LS) state ($S = 0$). However, $LaCoO_3$ nanoparticles have been shown to be magnetic (see below). Magnetism in $LaCoO_3$ arises from the superexchange coupling, i.e. the delocalization of an e_g electron between a Co^{3+} LS and a Co^{3+} HS ion via the orbitals of the connecting O^{2-}. The driving energy is the lowering of the kinetic enery by distributing the electrons across the entire metal-oxygen-metal chain [32, pp.274–278]. Understanding the mechanism of emergent ferromagnetism at the nanoscale can provide a whole series of new magnetic materials for nano-devices. $La_{1-x}Sr_xMnO_3$ on the other hand, is a ferromagnetic colossal magnetoresistance (CMR) material, where the CMR effect arises in the vicinity of $x = 0.33$ from the transition from ferromagnetic metal to paramagnetic insulator in an applied magnetic field [33]. Recently, this material has been explored for applications in magnetic hyperthermia treatments in its nanoparticle form [34–39] and thin-film structures have been considered for applications as spin-valve sensors and in magnetic random-access memories [40, 41]. Ferromagnetic coupling in $La_{1-x}Sr_xMnO_3$ is established by delocalizing the e_g electron of the Mn^{3+} across an O^{2-} ion to the Mn^{4+} ion by simultaneous hopping. This mechanism is called double exchange, where the ferromagnetic nature is due to Hund's first rule between localized t_{2g} electrons and the hopping, mobile e_g electrons [32, pp. 279–281]. In both materials, the size-dependent magnetic properties will be examined systematically. As the nanoparticle size can easily be manipulated, material-independent tunability of physical properties may be achieved.

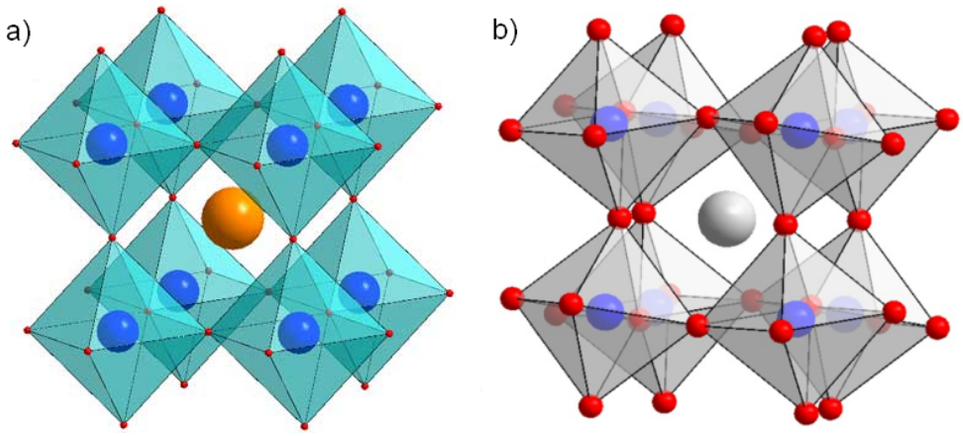

Figure 1.3: a) The cubic crystal structure of perovskite ABO_3 and b) the $R\bar{3}c$ rhombohedral crystal structure with tilted $[MO_6]$ octahedra. The oxygen ions (O^{2-}) are shown in red, the central yellow (a) or grey (b) ion represents A^{3+}, and the blue ions are the trivalent transition metal ions B^{3+}.

1.2 Background

1.2.1 $LaCoO_3$

1.2.1.1 Bulk $LaCoO_3$

$LaCoO_3$ has the $R\bar{3}c$ rhombohedral structure shown in Fig. 1.3, and tends to twin along the (100) and (110) pseudocubic lattice planes [42]. The structure can be derived from the cubic perovskite by tilting all oxygen octahedra about the [111] pseudocubic axes ($a^-a^-a^-$ tilt system). The deviation from cubic symmetry is due to the size of the central La^{3+} ion and can be quantified using the Goldschmidt tolerance factor f [41, 43]:

$$f = \frac{r_A + r_O}{\sqrt{2}(r_B + r_A)} \tag{1.4}$$

where r_A, r_B, and r_O are the radii of the ion in the centre of the pseudocubic cell, the ion inside the octahedra and the O^{2-} ion, respectively, in a generalized ABO_3 perovskite crystal structure.

As the tolerance factor $f \leq 1$, the structure distorts by tilting the $[CoO_{6/2}]^{3-}$ octahedra. The rhombohedral distortion of the pseudo-cubic cell can be analysed by the parameter δy, which describes the deviation of the 6e Wykoff position from the cubic one. In this framework, δy is defined for the position of the 6e atom, in this case oxygen, as $(1/4 - \delta y, 1/4 + \delta y, 3/4)$ [44]. The effect of the rhombohedral distortion δy on the electronic structure was calculated with density functional theory, yielding a critical value $\delta y = 0.052$, below which $LaCoO_3$ is magnetic, where

$$\delta y = \frac{d}{a}\cos(\theta/2) \tag{1.5}$$

with d the Co-O bond length, a the hexagonal lattice parameter, and θ the Co-O-Co bond angle [45].

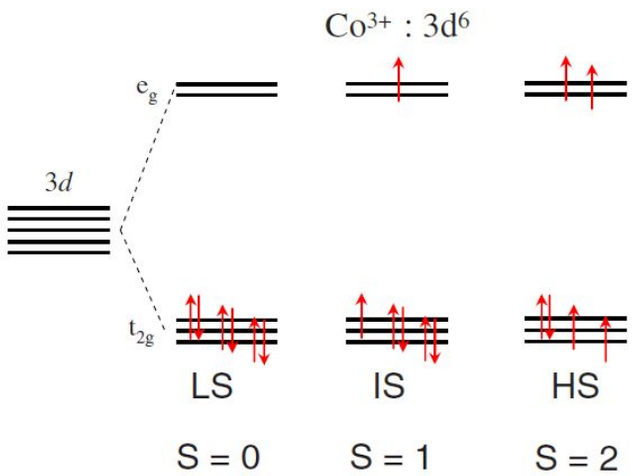

Figure 1.4: The e_g and t_{2g} $3d$ electronic energy levels are split by the crystal field. The Co^{3+} ion can occupy the low-spin (LS), intermediate spin (IS), or high spin (HS) states due to the small energy difference between these states [46].

Pure $LaCoO_3$ is non-magnetic ($S = 0$) at temperatures below 100 K [47, 48] and shows a transition to paramagnetic above [49], which is due to a spin transition: The Co^{3+} ion in $LaCoO_3$ has the $3d^6$ valence state and can be present in low-spin (LS), high-spin (HS) or intermediate-spin (IS) configuration. All three possibilities are shown schematically in Fig. 1.4. The spin configuration in $LaCoO_3$ is governed by the balance of crystal field splitting $\Delta_{cf} = 10\ Dq \approx 0.7$ eV [50, 51] and the intraatomic (Hund) exchange energy Δ_{ex} [52].

Table 1.1: The properties (spin quantum number, electronic configuration, effective magnetic moment m_{eff}, and atomic radius r_a) of low-spin (LS), high-spin (HS), and intermediate-spin (IS) states of the Co^{3+} ion $LaCoO_3$.

	LS	IS	HS
spin	S=0	S=1	S=2
configuration	$t_{2g}^6 e_g^0$	$t_{2g}^5 e_g^1$	$t_{2g}^4 e_g^2$
m_{eff} (μ_B)	0	2.11	3.16 [53, 54]
r_a (Å)	0.545	0.56	0.61 [55, 56]

The ground state of the Co^{3+} ion is thus low spin (LS, $S = 0$), with a transition to an excited state with higher spin at about 100 K. The HS or IS configurations are stable at higher temperatures due to thermal excitation and also lattice expansion, which tilts the balance between Δ_{cf} and Δ_{ex} towards the latter [52, 53]. It has long been a controversial

issue, whether the excited state is the IS or HS state, and what the energy differences between LS-IS and LS-HS are. The energy difference between LS and HS and between LS and IS have been calculated and measured by a range of techniques. Local density approximation (LDA+U) predicts that LS lies 0.08 eV under the excited high spin state (HS, $S = 2$) ([53] and references therein). The LS-IS difference is around 20 meV (232 K) [52, 57], and the LS-HS difference has been found at 125 meV (1450 K) [57]. As the large energy difference between LS and HS seemed incompatible with the low transition temperature between non-magnetic and paramagnetic behaviour, many researchers classified the transition at about 100 K as a LS⟶IS transition [58–62], which might be stabilized by hybridization of oxygen $2p$ states with cobalt $3d$ states [52] in violation of the Tanabe-Sugano diagram.

Instead of an isolated IS state, Ref. [63] have found a LS to LS/HS ordered state transition, with the order melting at high temperatures. The driving energy behind this phenomenon is proposed to be charge fluctuations, present at low temperatures. Considering a mixed state, Ref. [50] have used a thermodynamic approach and considered entropy of mixing. This shifted the energy balance in favour of a LS-HS mixed state (0.05 eV above pure LS) instead of the LS-IS mixed state (0.2 eV) [64]. This calculation predicted a Co^{3+} HS concentration of 33% at T=300 K [50]. Recently, a number of experiments provided strong evidence in favour of a LS⟶HS transition at 100 K, without an intermediate IS state. The degeneracy of the HS state is lifted by spin-orbit coupling, leading to a pseudo-orbital moment ($\tilde{L} = 1$) associated with the t_{2g} orbitals [51]. The coupling leads to a pseudo total momentum of $\tilde{J} = 1$ as the lowest lying triplet. This is in contrast to $LaCoO_3$ in the LS state, where orbital momentum is quenched and spin moment is fully compensated leading to $S = 0$. The spin-orbit coupling in Co^{3+} HS leads to $g = 3.5$ for the spin orbit triplet with $\tilde{J} = 1$ [65]. The expected magnetic moment μ_{eff} with these values is $\mu_{\text{eff}} = g_{\tilde{J}}\sqrt{\tilde{J}(\tilde{J}+1)} = 4.74$, which incidentally almost equals the expected moment for the spin-only contribution with $g_{\text{J}} = 1.95$ [66]. Electron paramagnetic studies found $g = 3.35$ [65, 67], whereas inelastic neutron scattering yields $g \approx 3$ [68] and Ref. [51] used X-ray magnetic circular dichroism and near-edge X-ray absorption (XA) analysis in combination with a configuration interaction cluster model to obtain $g = 3.2$. These results confirm the high-spin nature of the excited spin state in $LaCoO_3$, since $g_{\text{IS}} \approx 2.0$ [68]. These findings have been confirmed by multiplet fits on XA spectra of thin films [47, 69], as well as single crystals [59]. The IS state was found to lie about 0.1 eV above the LS and HS levels, which cross at $\Delta_{\text{cf}} = 1.7$ eV [69]. Eder used the variational cluster approach to confirm the HS excited state and also showed that, as the population of e_g bands increases at the expense of t_{2g}, there is a slight net charge transfer from Co to O. This is due to the admixture of HS $t_{2g}^4 e_g^2$ with the LS t_{2g}^6. As the e_g orbitals hybridize with O via the stronger σ bonds, the admixture results in a decrease of covalency, resulting in charge transfer back to oxygen.

An alternative way to differentiate between the IS and HS states is Jahn-Teller distortions. Due to the Jahn-Teller effect, systems with a single electron in a degenerate level will tend to split these levels by spontaneously distorting the octahedral environment. The change in energy is $\Delta E = -A\varepsilon + B\varepsilon^2$, where ε is the local strain and the first and second terms are the crystal-field stabilization energy and the elastic energy, respectively.

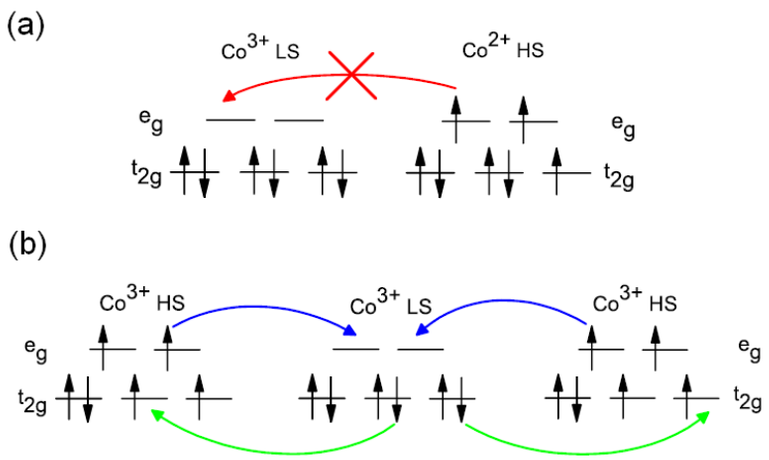

Figure 1.5: (a) The exchange between Co^{3+} LS and Co^{2+} HS is prohibited due to spin blocking. (b) Superexchange between Co^{3+} LS and Co^{3+} HS without charge transfer [47].

Clearly, the Co^{3+} LS is not Jahn-Teller (JT) active, because all the t_{2g} levels are occupied by two electrons each. The IS state, on the other hand, is JT active, as it only has one electron in the degenerate e_g states [56], whereas the JT effect is expected to be extremely weak in the HS state, since the only possibility to lower the energy is by splitting the t_{2g} levels, which are unequally occupied. The JT distortion reduces the symmetry of the environment, which can lift the quenching of the orbital moment and induce spin-orbit coupling [3, p.120]. As there is no experimental evidence for Jahn-Teller distortions in $LaCoO_3$ [70, 71], the "direct" cross-over from LS to HS can be confirmed, as well.

As the LS-HS energy difference is very low, entropy-based calculations predict 10% HS population as the ground state [72], and the population of the σ^* e_g bands (HS) at the expense of the π^* t_{2g} band occupation is a gradual cross-over instead of one sharp transition [73], centred around 90 K [74], with about 70% of all Co^{3+} ions in the high-spin state at 100 K [66]. The magnetic order is established between Co^{3+} HS and LS ions by superexchange, which according to the Goodenough-Kanamori-Anderson rules is ferromagnetic [3, p.139]. The redistribution of the spin moments of the t_{2g} electrons along the Co^{3+}HS–O–Co^{3+}LS bond allows the interchange of HS and LS without charge transfer [47]. This is shown in Fig. 1.5(b), whereas Fig. 1.5(a) shows that the presence of Co^{2+} cannot lead to ferromagnetic order by double exchange due to spin blocking. Long-range ferromagnetic order requires a continuous network of Co^{3+}HS–O–Co^{3+}LS bonds to allow electron hopping between Co^{3+} HS ions and Co^{3+} LS ions throughout the material. According to bond percolation theory this is achieved at a minimum concentration of 25% Co^{3+} HS [75], but since the Curie temperature T_C = 85 K, the necessary concentration is reached only at temperatures where the correlations are no longer strong enough in single-crystal $LaCoO_3$.

Even small changes to the bond length and the Co-O-Co angle can sensitively alter the balance between crystal field splitting and Hund coupling [47]. Parameter δy in

Equation 1.5 can serve as a critical parameter to determine whether the ground state of $LaCoO_3$ is non-magnetic ($\delta y \geq 0.052$) or magnetic with a magnetic moment of 1.3 μ_B if $\delta y \leq 0.052$ [44]. The sensitive correlation between crystal structure and magnetic moment has been confirmed in high-pressure experiments: the magnetic moment decreases as the pressure increases [57, 76, 77].

The sensitivity of magnetic properties of $LaCoO_3$ to the crystal structure is also reflected in the sensitivity to oxygen stoichiometry. As most perovskite oxides, $LaCoO_3$ shows a certain tendency to form oxygen vacancies. This property, like many others, can be size-dependent: First-principle calculations show that the oxygen-vacancy formation energy, as well as the adsorption energy, increase significantly if biaxial, tensile strains exceed $\varepsilon \geq 0.03$ [78]. This leads to an increase in structural anisotropy, as the Co-O bonds are stretched non-uniformly. Oxygen vacancy creation and ordering is observed in thin films under tensile strain [79, 80]. Oxygen stoichiometry plays a large role both in controlling structural and electronic properties [81, 82]. Oxygen vacancies V_O result in expansion of the lattice, but are equally reported to drive the rhombohedral structure towards cubic symmetry [42]. Elongation of the c-axis [17, 83] seems to lead to reduced conductivity [84] due to changes in the Co oxidation state [85–87] and disorder introduced by oxygen vacancies [85].

Oxygen vacancies in $LaCoO_3$ can lead to the reduction of Co^{3+} to Co^{2+}, and also the transferred electrons fill the unoccupied Co *3d* states. Co^{2+} can lead to a distorted tetrahedral coordination at the surface [79, 80], in which case the spins order antiferromagnetically [79]. Although Co^{2+} HS carries a magnetic moment ($t_{2g}^5 e_g^2, S = 3/2$), it cannot couple ferromagnetically to Co^{3+} HS due to the spin blockade effect [47]. Defects like Co^{2+} can act as nucleation sites for Co^{3+} IS or HS clusters [46, 88]. Oxygen vacancies [89, 90] can form magnetic polarons leading to a higher magnetic moment at low temperatures.

In polycrystalline samples, an increase of the ferromagnetic moment has been measured, as well as a larger difference between field-cooled and zero-field cooled curves [45], indicating association of ferromagnetic coupling with surface and interface defects. The interface between grains in polycrystalline materials makes them different from free-standing nanoparticles, the properties of which are discussed below. Androulakis et al. have identified two different kinds of ferromagnetic interactions depending on the temperature range, both related to Co^{4+} impurities which result from La vacancies [91]. A cluster glass with short-range ferromagnetic ordering was also observed [56].

1.2.1.2 Thin Films of $LaCoO_3$

A large concentration of Co^{3+} at low temperatures due to epitaxial strain was first observed by Fuchs et al. [1] and confirmed by Refs. [92, 93]. The stretching of the Co-O bond by epitaxy stablizes a 75% high-spin/25% low-spin mixed state which leads to ferromagnetic behaviour at $T \leq 85$ K [1, 94]. As polycrystalline, unstrained films do not show ferromagnetism, the possibility of surface-based ferromagnetism is eliminated. Choi et al. showed that only positive epitaxial strain can lead to a ferromagnetic $LaCoO_3$ low-temperature state [92]. For extremely thin films (15 unit cells) on $SrTiO_3$ the ferromagnetic

state is stabilized at $T \leq 55$ K [55], which is probably due to the intrinsic size effect discussed above.

1.2.1.3 Nanoparticles of $LaCoO_3$

An elongation of $d_{\text{Co-O}}$ by up to 0.2% and increase of the unit-cell volume by up to 0.3% has been measured for nanoparticles with diameter $24 \leq \langle s \rangle \leq 500$ nm, achieved by varying the calcination temperature $600 \leq T_{\text{calc}} \leq 1100$°C [76, 77, 95–97]. Calcination means the heat treatment at high temperatures to induce crystallization. The changes seem to scale linearly with S/V. A summary is provided in Table 1.2. Similarly to the high-pressure experiments and the epitaxially strained thin films described above, the structural changes could lead to ferromagnetic behaviour in nanoparticles of $LaCoO_3$.

Several groups have indeed observed ferromagnetic order at $T \leq 85\ K$ in nanoparticles of $LaCoO_3$ [76, 77, 95–97, 100, 101]. The transition temperature seems to be independent of the particle size. Wei et al. identify $s = 130$ nm as the critical size below which ferromagnetic behaviour occurs [97], but Zhou et al. reported ferromagnetic behaviour up to particle sizes as large as 450 nm [96].

Several mechanism for NP ferromagnetism were considered. An overview over the magnetic properties of $LaCoO_3$ NP measured so far is given in Table 1.2. Although all studies show an increase of magnetic moment with decreasing nanoparticle size, there seems to be little consistency in the value of magnetic moment and the general magnetic behaviour.

Firstly, it was suggested that the ferromagnetism arises mainly at the surface of $LaCoO_3$ nanoparticles [102], which is supported by single-crystal studies [100]. Fuchs et al., on the other hand, have shown that the ferromagnetic moment increases with film thickness in thin films, which shows that the epitaxial strain induces ferromagnetism in the bulk of thin films, with negligible surface contribution [1].

Durand et al. have also related the ferromagnetic interactions in $LaCoO_3$ nanoparticles to moments at interfaces due to the presence of Co_3O_4. These moments are supposed to order at low temperatures due to tensile stress in the material [100, 101]. The increase of the c lattice parameter is described as a consequence of ferromagnetic cluster formation, not as the origin [45]. An alternative explanation can be found in the Jahn-Teller (JT) distortion of the octahedra [95] by surface tension [97]. As pointed out above, the IS state of Co^{3+} is not expected to be occupied at all, but instead the competition is between LS and HS states. Since none of these are JT active, explanations involving the JT effect are less likely.

As has been shown for thin films, the transition to the higher spin state can be induced by lattice expansion which has been systematically studied on epitaxially strained $LaCoO_3$ thin films deposited on different substrates [47, 69, 103], and Co^{3+} HS state was also suggested in nanoparticles [76, 77, 95, 97]. Refs. [95–97] find a ferromagnetic and paramagnetic phase co-existence, with increased magnetic moment at smaller particle sizes due to expansion of the unit cell [95]. Ref. [76, 77] have shown a size-dependent increase of ferromagnetic order alongside expansion of the unit-cell volume, and, just as Ref. [99], they suggest magnetic phase separation into a ferromagnetic and an antiferro-

Table 1.2: Summary of $LaCoO_3$ studies published on nanoparticles: Reference, synthesis technique, range of nanoparticle sizes, information on oxygen stoichiometry and size-related changes of the crystal structure, as well as magnetic properties such as the magnetization at an applied field of 5 T, the trend of magnetization vs. surface-to-volume ratio S/V, the Curie temperature T_C, its change with S/V, and the suggested mechanism of size-induced magnetism in $LaCoO_3$ NP.

Ref.	synthesis technique	size (nm)	oxygen	structural changes
[76, 77]	citrate method, $600 \leq T_{calc} \leq 900°C$	25–38	$\delta = 0.05 \pm 0.05$, by EDX and XRD Rietveld	• a(25 nm)=5.445 Å, c(25 nm)=13.14 Å • V_{uc}(25 nm)= 337.38 Å^3, • $(\Delta a/a_b = 0.1\%, \Delta c/c_b = 0.6\%$, $\Delta V_{uc}/V_{uc,b} = 0.7\%)$ • V_{uc}, $d_{Co\text{-}O} \propto 1/D$, mainly $V_{[CoO_{6/2}]^{3-}}$ increase, not rotation
[96, 98]	sol-gel, $600 \leq T_{calc} \leq 900°C$	60–450	NA	• $a_{nano} = a_b$, c(60 nm)= 13.122 Å • V_{uc}(60 nm)= 336.83 Å^3 • $\Delta c/c_b = 0.2\%, \Delta V_{uc}/V_{uc,b} = 0.3\%$
[97]	sol-gel, $600 \leq T_{calc} \leq 1100°C$	40–500	NA	• $a_{nano} = a_b$, c(40 nm)= 13.10 Å • V_{uc}(40 nm)= 335.81 Å^3 • $\Delta c/c_b = \Delta V_{uc}/V_{uc,b} = 0.2\%$
[99]	coprecipitation	18-500	NA, but up to 28% Co_3O_4	• a & c expanded • $\Delta a/a_b = 0.2\%$

Ref.	$M_{\mu_0 H=5\,\mathrm{T}}$ (emu/g)	trend of M	T_C (K)	trend of T_C	explanation
[76, 77]	3.2	$dM/d(S/V) \geq 0$, $dM/d(V_{uc}) \geq 0$	85	NA	•unit-cell expansion reduces crystal field splitting and stabilizes IS state •FM moment of $\mu_{eff} = 2.44\ \mu_B$/Co •AFM interactions indicate IS Co^{3+} •phase separation between IS-rich ferromagnetic and LS-rich non-magnetic phases
[96, 98]	2.2	$dM/d(S/V) \geq 0$	≈ 85	NA	•FM in the bulk due to higher amount of HS Co^{3+} resulting from unit-cell expansion •PM due to LS Co^{3+} at the surface, some IS character due to virtual excitations •PM and FM phase behaviour does not depend on size •phase separation by ordering of IS-rich and LS-rich regions
[97]	3	at $\mu_0 H$ =5 T, $dM/d(S/V) \geq 0$, at $\mu_0 H$ =10 mT $dM/d(S/V) \leq 0$	35–85	$dT_C/d(S/V) \leq 0$	•surface IS states •orbital order IS at the surface •unit-cell expansion weakens superexchange, resulting in progressive growth of PM fraction at the expense of the FM phase
[99]	$\approx$3.7 ($\mu_0 H$ =6 T)	$dM/d(S/V) \geq 0$, and M increases for increasing Co_3O_4-content	75	$dT_C/d(S/V) \leq 0$	•short-range AFM in core, highly frustrated below 40 K •long-range FM in interface regions (2D Heisenberg) •tensile strain by $Co_3O_4/LaCoO_3$ interfaces •does not take magnetic moment of Co_3O_4 into account

magnetic part. They have also shown that the ferromagnetic moment can be reduced by applying isostatic pressure to the nanoparticles.

Alternatively, Co^{3+} HS ions could be present only at the particle surface, which could explain why the transition temperature does not change with particle size. However, since the lattice expansion as observed from X-ray diffraction is a bulk effect of the entire NP, it cannot be related to surface magnetization. Moreover, Ref. [69] have ruled out the surface effect by comparing surface-based (Auger spectroscopy) results to bulk results. The thickness dependence of magnetization in $LaCoO_3$ thin films, as shown by Ref. [1], is in contradiction to surface-based magnetism, too.

All references cited in Table 1.2 assume phase separation into two micro-regions, but a deeper understanding of $LaCoO_3$ at the nanoscale seems to be lacking. Although several references have suggested a relationship between unit-cell expansion and increase of magnetic moment due to stabilization of the HS state, to the best of my knowledge there have been no studies directly assessing the size-dependent concentration of Co^{3+} HS. Additionally, there seems to be no agreement in the quantitative relationship between size and structural parameters and size and magnetic properties.

Some of the discrepancies could be a result of synthesis procedures. One possibility to prepare nanoparticles of $LaCoO_3$ is co-precipitation [99], but this leads to significant amounts (up to 28%) of Co_3O_4. Alternative methods, such as the citrate method [77], and the sol-gel method [95, 97], require a variation of calcination temperature T_{calc} to obtain different particle sizes. At $T_{calc} \geq 600°C$, particles start to sinter, forming polycrystalline material with grain boundaries, which are different both from the crystallite in the particle bulk and from the free surface [104]. In addition, impurity phases start to form at higher calcination temperatures [105, 106], which suggests thermodynamic instability of the pure $LaCoO_3$ phase, and hence it is quite likely that even at lower temperatures impurities or defects form without being seen in the X-Ray diffraction pattern, because the impurity pattern is smeared out due to the small NP size and cannot be separated from the background. Nonetheless, the defect density due to impurities will be more pronounced for nanoparticles treated at higher calcination temperatures, yielding different properties compared to samples treated at lower temperatures. These differences are not intrinsically related to the NP size. On the other hand, increasing the calcination temperature tends to anneal crystalline defects such as vacancies, dislocations and stacking faults, which also leads to different properties for differently calcined samples. Even oxygen stoichiometry can be a function of the calcination temperature [107] or cooling rate [108, 109]. Consequently, any variation in physical properties, e.g. magnetism, could be either due to nanoparticle size or due to the difference in calcination procedure.

Therefore, the samples prepared in the present study are all calcined at the same temperature. This separates purely size-induced effects on physical properties from other effects such as defect densities related to calcination temperature. The increasing Co-O distance $d_{Co\text{-}O}$ with increasing S/V is thus shown to be an intrinsic consequence of reduced NP size.

1.2.2 $La_{1-x}Sr_xMnO_3$

1.2.2.1 The effects of Sr substitution in $LaMnO_3$

Similarly to $LaCoO_3$, the structure of $LaMnO_3$ can be derived from the cubic ABO_3 perovskite, but instead of the rhombohedral structure, pure $LaMnO_3$ has the orthorhombic structure *Pbnm*. Replacing a fraction x of the La^{3+} ions by the larger Sr^{2+} ions results in a reduction of the Mn-O bond length d and an increase of the Mn-O-Mn bond angle θ towards 180°. At room temperature, the transition from orthorhombic *Pbnm* to rhombohedral R$\bar{3}$c occurs at $x = 0.17$ [26, 110, 111].

Due to charge neutrality, replacing La^{3+} by Sr^{2+} increases the maganese valence from Mn^{3+} to Mn^{4+} for the same fraction x of the manganese ions. Besides thin-film preparation, the rich phase diagram (Fig. 1.6) and magnetoelastic coupling in $La_{1-x}Sr_xMnO_3$ has triggered strong research activity into $La_{1-x}Sr_xMnO_3$ nanoparticles [19, 36, 112–126].

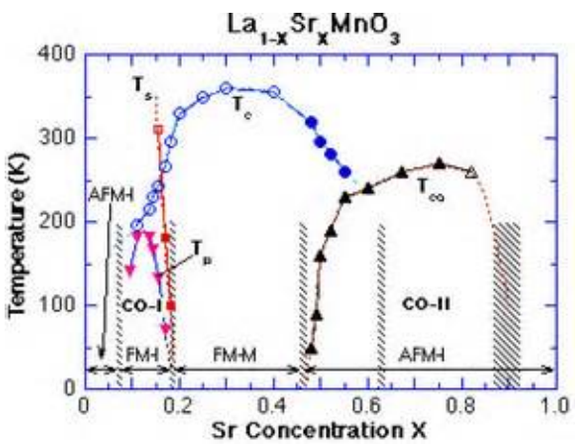

Figure 1.6: Phase diagram of $La_{1-x}Sr_xMnO_3$ [127].

Since the crystal-field splitting in $La_{1-x}Sr_xMnO_3$ is $\Delta_{cf} = 1.5$ eV, but the exchange energy is $\Delta_{ex} = 2.5$ eV, the Mn^{3+} ions are in the high-spin state with $S = 2$, and $S = 3/2$ for Mn^{4+} [40]. As described above, the Jahn-Teller distortion can lift the degeneracy, and lower the energy of the Mn^{3+} ion (Mn^{4+} is not JT-active). While the distortion is often observed in manganites with $x \leq 0.17$, it is strongly reduced at higher levels of Sr substitution [40].

The presence of both Mn^{4+} and Mn^{3+} ions results in e_g double exchange between Mn^{3+} and Mn^{4+} via Mn *3d* and O *2p* orbitals [129–131], as illustrated schematically in Fig. 1.7. For a doping level exceeding $x = 0.175$ [110, 127], the material transits from a paramagnet (PM) to a ferromagnet (FM) at room temperature (see Fig. 1.6). Since double exchange is very sensitive to the orbital overlap, positive pressure and strain can increase the magnetic ordering temperature [41, 132–134], whereas anisotropic or negative strain can reduce T_C [40, 41, 134–137] or modify the orbital order [138, 139], and the octahedra tilt [140–145]. Tensile strain of the lattice can lead to an increase of the Mn-O-Mn bond towards 180 °, which has been observed experimentally [31, 113, 146–148]. Equation (1.6) correlates the

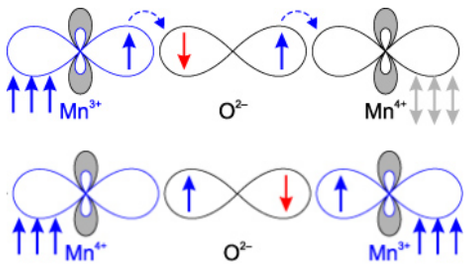

Figure 1.7: Schematic representation of double-exchange coupling between Mn^{3+} and Mn^{4+} ions in $La_{1-x}Sr_xMnO_3$. Electron hopping is only possible if the t_{2g} spins on the left and right ions are aligned [128].

Curie temperature under strain ($T_C(\varepsilon_B, \varepsilon_{JT})$) with the bulk compressive strain ε_B, the JT distortion ε_{JT} and the Curie temperature for unstrained samples, T_{C0} [149]:

$$T_C(\varepsilon_B, \varepsilon_{JT}) = T_{C0}\left(1 + \frac{\varepsilon_B}{T_C}\frac{dT_C}{d\varepsilon_B} - \frac{\varepsilon_{JT}^2}{2T_C}\frac{d^2T_C}{d\varepsilon_{JT}^2}\right) \tag{1.6}$$

Hence, the magnetic properties of $La_{1-x}Sr_xMnO_3$ show a sensitivity to structural parameters, too, but in contrast to $LaCoO_3$ the relationship is based on the double-exchange mechanism rather than the spin-state transition in $LaCoO_3$.

Delocalization of the e_g electrons via double exchange leads to electrical conductivity as well as ferromagnetism. Electrical conduction in these manganites is metal-like below T_C with a high spin polarization [40, 144, 150] and changes to activated transport above: both small polaron and variable range hopping have been observed [151, 152]. It has been found that this metal-insulator transition temperature, i.e. Curie temperature T_C, shifts with applied fields to higher temperatures [33, 41, 110, 153]. At temperatures close to T_C, it is therefore possible to observe a resistivity drops by several orders of magnitude if a magnetic field of several Tesla is applied, because the metal-insulator transition temperature increases when applying a field. This behaviour is termed colossal magnetoresistance (CMR).

Within the double-exchange picture introduced by C. Zener [154], the CMR effect is explained by localization of the electrons on Mn ions, resulting from the three t_{2g} electrons. The mobile e_g electrons, on the other hand, have a transfer interval based on the angle Θ between two neighbouring localized $S = 3/2$ spins [40]. The transfer intergral $t = t_0 \cos\Theta/2$ can be influenced by a magnetic field if it is strong enough to align the core moments [41]. Millis et al. have shown that the behaviour of CMR manganites cannot fully be understood in the double-exchange picture, and electron-phonon coupling both to Jahn-Teller and breathing-type modes has to be considered, which leads to an increased sensitivity to applied strain [149, 155]. This is reflected by lattice contraction when cooling through T_C [41]. The wide band-gap manganites such as $La_{1-x}Sr_xMnO_3$ with $0.25 \leq x \leq 0.5$ can be described quite realistically using a pure double-exchange picture, whereas manganites with low T_C and high magnetoresistance are far away from a pure double-exchange behaviour [41].

1.2.2.2 $La_{1-x}Sr_xMnO_3$ nanoparticles

Despite the possible influence of particle size on structural and therefore magnetic properties in $La_{1-x}Sr_xMnO_3$ NPs, reliable systematic studies are lacking. Research published so far is often contradictory, mostly with respect to the influence of nanoparticle size on the structural parameters.

Towards the nanoscale, an increase of the Mn-O-Mn bond angle towards 180° and a decrease in the bond length Mn-O was observed [113, 133, 156], both of which strengthen the double-exchange coupling [157, 158]. An overall expansion of the lattice was observed for nanoparticles with 50 nm diameter [133] and down to 16 nm attributed to reduced surface coordination and disorder [121]. In contradiction, unit-cell contraction has been measured in $La_{0.7}Sr_{0.3}MnO_3$ nanoparticles synthesized by the same method and with diameters less than 22 nm [156, 159]. The reasons behind this discrepancy are not fully understood, but possible explanations will be discussed below.

As mentioned on page 3, the surface of nanoparticles is often found to be magnetically frustrated [7], which results in a reduced magnetic moment compared to bulk. However, in $La_{1-x}Sr_xMnO_3$ other effects can be responsible for reduced magnetization at the surface [35, 115, 118–120, 133, 156, 159–162] for nanoparticles below 50 nm diameter [112, 163]. Cation redistribution – i.e. accumulation of Sr on the surface – due to electrostatic reasons and lattice strain from the difference in atomic radii between La^{3+} and Sr^{2+} have been reported in thin films [164] and nanoparticles. This could be one of the reasons behind non-magnetic shells on $La_{0.7}Sr_{0.3}MnO_3$ particles [165]. On the other hand, magnetic core-shell structures have been observed without any indication of structural changes in TEM micrographs [166].

Although some studies found that $La_{1-x}Sr_xMnO_3$ nanoparticles down to 15 nm size have the same T_C as bulk single crystals [167, 168], mostly a decrease of the Curie temperature has been observed [35, 36, 113, 117, 124, 159, 163, 169]. A selection of results is presented in Table 1.3:

Table 1.3: Some studies on nanoparticles with different size and Sr concentration x showing structural changes, relative change of T_C (ΔT_C) and explanation.

Ref.	size (nm)	x	structural changes	$\Delta\ T_C$ (%)	explanation
[113, 117]	15	1/3	NA	-8	NA
[163]	50	1/3	no change	-13	chemical inhomogeneity
[124]	20–95	1/3	$\frac{\Delta V_{uc}}{V_{uc}} = -0.46\%$	-18 – 0	finite-size effect
[35]	30–49	0.25	NA	-8 – -5	magnetically dead layer
[36]	11–14	0.45	NA	-23 – -7	NA
	& 12–16	& 0.25	NA	& -18 – -1	NA
[118]	37–90	0.3	$\frac{d\Delta a}{d(S/V)} \geq 0$	no change	NA
[169]	15	1/3	no change	-4	NA
[159]	19–34	0.3	$\frac{d\Delta V_{uc}}{d(S/V)} \leq 0$	-8 – 0	finite-size effect

Table 1.3 clearly reveals a lack of consistency in the relationship between T_C reduction and nanoparticle size, and detailed structural analysis was not always performed. Variation in experimental values is typical of perovskite manganites, as these materials can tolerate significant deviation from stoichiometry without structural phase transitions, while their properties are extremely sensitive to stoichiometry and defect structures [135]. As for $LaCoO_3$, the preparation techniques for $La_{1-x}Sr_xMnO_3$ nanoparticles largely involve a variation of the calcination temperatures [35, 36, 113, 117, 118, 121, 124, 133, 159], which makes it difficult to isolate the influence of the nanoparticle size. For example, varying the calcination temperature between 700 and 1100°C for $La_{1-x}Ca_xMnO_3$ can change the concentration of oxygen vacancies by up to 10% [107, 170] (although the crystal lattice parameters only differ by up to 0.3%). The Mn-O-Mn bond angle may shrink by up to 1.2% (Ref. [148]). Refs. [122] and [39] used the glycine nitrate process to produce $La_{1-x}Sr_xMnO_3$ nanoparticles, and found that the change in T_C is different depending on whether $x < 0.25$ or $x > 0.25$. In the former case, nanoparticles have an increased T_C compared to bulk values, whereas in the latter case T_C was lowered for nanosized particles ($d \approx 26$ nm) due to oxygen excess. In thin films, the reduced T_C is possibly related to disorder, which can lead to a less efficient double-exchange coupling and localize charge carriers [171].

Different critical nanoparticle sizes to achieve single-domain behaviour have been reported for $x = 1/3$: 22 nm [159], 36 nm [113], or 50 nm [172]. The discrepancy could be related to defect density. Decreasing the size further, the superparamagnetic limit can be reached at sizes of ≈ 10 nm [173] to 16 nm [162, 174] with a blocking temperature T_B (see Equation 1.2) of 110 K for NPs of 12 nm [115] and 320 K for $La_{1-x}Sr_xMnO_3$ nanoparticles with $s \approx 20$ nm, and with $x = 0.3$ [175]. In the present study, all samples of $La_{1-x}Sr_xMnO_3$ are outside the superparamagnetic regime because their size is too large ($\langle s \rangle \geq 20$ nm) or because the Curie temperature is too low ($T_C \leq 320$ K).

Similarly to $LaCoO_3$ the $La_{1-x}Sr_xMnO_3$ NP samples in the present work are synthesized using the same calcination conditions for different average NP sizes. This allows the direct comparison of nanoparticle size and magnetic properties without any influence of calcination temperature.

2 Methods

2.1 Synthesis

The two main methods to produce transition-metal oxide NPs are sol-gel synthesis and microemulsion synthesis (ME). While sol-gel synthesis is widely applied to produce perovskite NPs, varying the concentration of precursor species allows only a very limited control over particle size. To produce a wider range in sizes, calcination temperatures are varied from 600-1100°C for $LaCoO_3$ [76, 77, 95, 97, 98], and between 700-1200°C for $La_{1-x}Sr_xMnO_3$ [113, 118, 121, 126, 133, 159].

Although this is an easy way to change the NP size [36], it has also a pronounced effect on crystal quality, defect density, and oxygen stoichiometry [27, 48, 107], making a comparison of NP with respect to their structural and magnetic properties difficult.

In the end, ME was employed to produce NP batches with different average sizes using comparable synthesis conditions. While having the advantage of producing a range of NP sizes under similar conditions, ME has the drawback of extremely low yield, which prevented he use of some characterization techniques, such as quantitative chemical analysis or surface area measurement by adsorption.

2.1.1 Microemulsion Synthesis

A microemulsion generally contains four components: a hydrophobic phase (e.g. hexanol), a hydrophilic phase (water), a surfactant and a co-surfactant (usually short to medium chain alcohols [176, 177]). The right amount of surfactant leads to the formation of reverse micelles which can be considered ”nanoreactors” [178], limiting the size of the nanoparticles. The micelles form as a compromise between increase in energy due to non-homogeneous distribution of surfactant molecules and energy gain due to ion-dipole interaction by bringing the hydrophilic chain ends into contact with the water fraction and hydrophobic chain ends into contact with the non-aqueous portion.

2.1.1.1 Size Control

The size of the ”nanoreactor”, which influences the expected nanoparticle size, is difficult to predict. A simple estimate of the micellar radius R_m given in Ref. [179] is based on the electric double layer due to the surfactant molecules at the water-oil interface, ΔG_{edl}, the entropy contribution ΔG_E and the interfacial tension γ_{ME}:

$$R_m = \frac{0.99 \times \gamma_{ME}}{\Delta G_E - \Delta G_{edl}} \tag{2.1}$$

This implies that microemulsions are thermodynamically stable in certain regimes of water-to-surfactant ratio and temperature, since the orientation of molecules minimizes the interfacial tension [179, 180].

The walls of these "nanoreactors" are not rigid and hence mixing two microemulsions with different species contained in the water phase leads to exchange of these species between micelles. The wall energy can be optimized by adding co-surfactants, which act as spacers between the positively charged surfactant heads [180], influencing both γ_{ME} and ΔG_{edl}.

The general procedure for ME synthesis requires at least two microemulsions with the same water-to-surfactant ratio. One ME contains the nitrate salts of the elements required for the product dissolved in the water phase, the second one contains a precipitating agent, e.g. NaOH or $(CH)_4NOH$. Mixing the two microemulsions leads to the precipitation of hydroxides (low solubility in water) within the micelles. The size of the precipitate can be controlled by the size of the micelle and the concentration of the precursors, i.e. by the amount of material available inside the micelle for growth of the nuclei. The hydroxide particles are covered by surfactant molecules, which largely prevent contact between hydroxide particles and thus minimizes further coalescence and growth.

In traditional precipitation in the supersaturation regime the particle size distribution becomes Gaussian: the evolution of the mean particle size $\overline{r}$ is a function of the molar concentration of precursors C_0, decreasing with time t, the molar volume V_{m}, and the diffusion coefficient [181].

$$\overline{r} = \sqrt{2DV_{\mathrm{m}}C_0}\sqrt{t} \tag{2.2}$$

In stationary conditions this leads to the distribution $P(r)$:

$$P(r) \propto \exp \frac{-K(r - r^*)^2}{k_{\mathrm{B}}T} \tag{2.3}$$

where r^* is the critical radius, and K is a constant. However, for the case of microemulsion synthesis, the conditions are not stationary, and a sharp size distribution can be achieved with

$$\overline{r} \propto t^{0.33} \tag{2.4}$$

The time allowed for reaction is therefore a balance between providing enough time for the micromicelles to exchange their content and stopping the reaction in time to avoid coarsening.

The size of the micelle (radius R_{M}) can be controlled by the water-to-surfactant ratio R_w within a certain range. Considering the micellar molar volume V_{M} as a function of the moles of surfactant and water per micelle, n_{S} and n_{w}[180]:

$$V_{\mathrm{M}} = \frac{4\pi R_{\mathrm{M}}^3}{3} = n_{\mathrm{s}}V_{\mathrm{s}} + n_{\mathrm{w}}V_{\mathrm{w}} \tag{2.5}$$

where V_{w} is the volume of water in the micelle.

The surface area S_{M} of the micelle can be approximated as:

$$S_{\mathrm{M}} = 4\pi R_{\mathrm{M}}^2 = n_{\mathrm{s}} S_{\mathrm{s}} \tag{2.6}$$

where S_{s} is the molar interfacial area at the surfactant-oil boundary. Fixing the volume of the system, $R_w = n_{\mathrm{w}}/n_{\mathrm{S}}$, the micelle radius becomes:

$$R_{\mathrm{M}} = \frac{3V_{\mathrm{s}}}{S_{\mathrm{s}}} + \frac{3V_{\mathrm{w}} R_w}{S_{\mathrm{s}}} \tag{2.7}$$

The inner radius of the micelle, i.e. the radius of the water droplet, is:

$$R_{\mathrm{M,i}} = \frac{3V_{\mathrm{W,t}}}{S} \tag{2.8}$$

where $V_{\mathrm{W,t}}$ is the total water volume and S is the total interfacial area per unit mass of microemulsion [182]. Assuming only monolayers of surfactant molecules and neglecting the ones at the surface of the microemulsion, S can be calculated as:

$$S = a_{\mathrm{h}} \times \frac{(\gamma - c\mu c) m N_{\mathrm{A}}}{M_{\mathrm{S}}} \tag{2.9}$$

where a_{h} is the specific surfactant molecule area, on the order of ≈ 0.5 nm^2, $c\mu c$ the critical microemulsion concentration, γ the weight fraction of the surfactant ($\gamma = m_{\mathrm{surf}}/m_{\mathrm{total}}$), N_{A} Avogadro's constant and M_{S} the molecular mass of the surfactant.

Eq. 2.8 is valid for $R_w \geq 10$, as at smaller values V_{w}, V_{S} and S_{S} are no longer independent of R_w[180]. On the other hand, increasing the water content too much tends to form a two-phase system where the curvature of the boundary between continuous phases of oil and water is constant throughout the system [183]. In this bicontinuous regime the amount of molecules available for particle growth is no longer limited by a "nanoreactor" boundary, and time, temperature and precursor concentration become the only controlling factors, usually leading to much larger nanoparticle sizes compared to the ME regime. The ME stability range is also influenced by temperature, the precursor concentration [184], and the nature of the precursors [180].

This simple picture of size control by micelle size neglects the influence of micelle wall flexibility. While Brownian motion leads to frequent collisions between micelles, not every collision results in the exchange of matter. Depending on the surfactant (molecule size, ionic charge, chain rigidity and branching), the probability for exchanging contents upon collision can be higher or lower, influencing the reaction time of precipitation and growth and hence influencing the size of the nanoparticles at a given reaction time [183]. Furthermore, the rigidity of the micelle wall influences the micelle size and hence changing the surfactant or the co-surfactant or the ratio of surfactant to co-surfactant can change the range of possible micelle sizes and expand the possible range of nanoparticle sizes. However, using ethylene glycols (Synthesis A) or cetyl trimethyl ammonium bromide (Synthesis B) as surfactants, the same R_w resulted in similar nanoparticle sizes. For example, using $R_w = 8$, Synthesis A yields $\langle s \rangle = 19.5$ nm, and Synthesis B results in $\langle s \rangle = 19$ nm for $LaCoO_3$. The ratio of surfactant to co-surfactant cannot be varied indefinitely, as systems with two or more different micelle

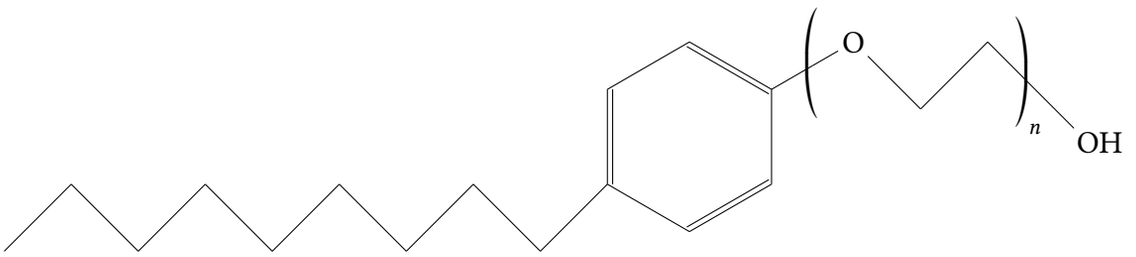

Figure 2.1: Molecular formula of nonylphenol *n*-ethylene glycol ether, with $n = 5$ for Tergitol-NP5®and $n = 9$ for Tergitol-NP9®

sizes can develop, leading to a large size distribution or element-specific segregation of the precursors.

In addition to the sensitive thermodynamic balance of ME, the choice of surfactant can lead to chemical reactions between surfactant and precursors, changing the ratio of the elements in the final product, or leading to secondary phases [180]. Therefore, thorough washing is required when using CTAB to avoid the formation of $LaBr_3$.

2.1.1.2 Procedure

In the present work, the samples were prepared using microemulsions with nonylphenol polyethylene glycol ether [185] (Fig. 2.1) and cetyl trymethyl ammonium bromide (CTAB, see Fig. 2.2), obtained from VWR International)[186] as surfactants, respectively. In the former case, a 2:1 mixture of nonylphenol pentaethylene glycol ether (Tergitol-NP5®) and nonylphenol nonaethylene glycol ether (Tergitol-NP9®) was used (shown in Fig. 2.1). Synthesis procedures for NP5/NP9-based (A) and CTAB-based (B) microemulsions were slightly different, and Synthesis A could be optimized to yield smaller diameter NP than Synthesis B, but was also prone to impurity phases such as Co_3O_4 and La_2O_3. Only samples without any Co_3O_4 and less than 10 wt.% La_2O_3 were characterized.

For Synthesis A, three microemulsions were synthesized with the same water-to-surfactant ratio R_w per batch. Water-in-oil microemulsion 1 (ME1) contained $La(NO_3)_3.6\,H_2O$ and microemulsion 2 (ME2) contained $Co(NO_3)_3 \cdot xH_2O$. Both salts were obtained from VWR International and used as delivered. The ratio of La:Co was set to 11:10, as excess La reduces the formation of Co_3O_4. The total concentration of precursor salts in water, C_0, was varied between 109 g/l $\leq C_0 \leq$ 365 g/l. The solubilities in water of $La(NO_3)_3 \cdot 6\,H_2O$ and $Co(NO_3)_3 \cdot xH_2O$ being 1580 g/l [187] and 1338 g/l [188], respectively, the salts are fully dissolved in ME1 and ME2. Microemulsions 1 and 2 were mixed for 30 minutes at room temperature. The formation of the microemulsion reduces the temperature of the mixture to 4°C.

Then, microemulsion 3 (ME3), containing 0.1 mol/l NaOH and 0.013 wt.% H_2O_2 was added dropwise under constant stirring. The amount of ME3 was adjusted depending on the concentration of $La(NO_3)_3 \cdot 6\,H_2O$ in the water fraction of ME1, so that the La^{3+}/OH^- ratio was constant for all batches synthesized with Synthesis A. The increase of the pH-value induces precipitation of hydroxides according to:

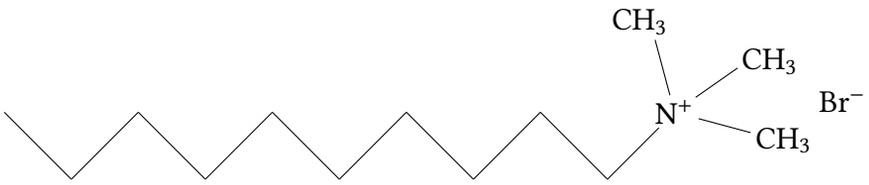

Figure 2.2: Molecular formula of the cetyl trimethyl ammonium bromide (CTAB) surfactant.

$$La^{3+} + 3NO_3{}^- + 3Na^+ + 3OH^- \longrightarrow La(OH)_3\downarrow + 3Na^+ + 3NO_3{}^+ \quad (2.10)$$

$$Co^{2+} + 2NO_3{}^- + 2Na^+ + 2OH^- \longrightarrow Co(OH)_2\downarrow + 2Na^+ + 2NO_3{}^+ \quad (2.11)$$

Initially, the precipitate appears green. Most likely this is a complex formed with a reaction product of the ether-based surfactant in basic environment. For instance, the ether could be split by basic hydrolisation [189], followed by oxidation of the alkohol to oxalate by H_2O_2. The $[Co(ox)_3]^{3-}$ complex has an olive colour, but is unstable as the basicity grows due to matter exchange between micromicelles from ME1/ME2 and ME3. As the complex dissociates into $Co(OH)_2$, the green colour disappears progressively.

The kinetics of the reaction is greatly reduced since the exchange rate between micromicelles (usually on the order of 10^6-10^8 dm^3/mol/s [190]) is the determining factor. The reaction was allowed to proceed for another hour at room temperature before adding methanol in a volume ratio of 2:1. This leads to agglomeration and settling of brownish-black NP agglomerates, formed as a result of the reaction of $Co(OH)_2$ with H_2O_2:

$$2\overset{+II}{Co}(OH)_2 + H_2O_2 \longrightarrow \overset{+III}{Co}_2O_3 \cdot xH_2O + (x-1)H_2O \quad (2.12)$$

where $\overset{+III}{Co}_2O_3 \cdot xH_2O$ has a brown colour [191]. The black tone indicates that some of the products have oxidised to $\overset{+IV}{Co}O_2 \cdot xH_2O$. Heating in oxygen above 500°C tends to reduce Co in oxygen-containing compounds [191], hence no $\overset{+IV}{Co}$ is expected to remain after calcination at 600°C.

After the reaction, the mixture was centrifuged to recover the amorphous NP covered in surfactant. Washing cycles were completed as follows: stirring in the washing solution, 10 minutes of ultrasonication, and centrifuging for 25 minutes at 3500 rpm. Using this procedure, the NP were washed three times in water and two times in methanol. Before centrifugation, NH_3 was added each time to induce agglomeration. NP were then dried under vacuum ($p \leq 0.001$ mbar) at 180°C in order to decompose remaining organic molecules. Two hours of ultrasonication results in a stable dispersion of the NP in water, whereas the carbon residue settles and can be separated.

Synthesis B (using CTAB as surfactant) was carried out with three microemulsions prepared with the same water–to–surfactant ratio R_w, one containing the dissolved precursors $La(NO_3)_3 \cdot 6\,H_2O$ and $Co(NO_3)_3 \cdot xH_2O$ with a La/Co ratio of 1.1, the second one with tetramethyl ammonium hydroxide ($(CH_3)_4NOH$), and the third one with H_2O_2 dissolved in the water fractions, respectively. The precursor salt concentration was 0.076 mol/l in

total. The concentrations of $(CH_3)_4NOH$ and H_2O_2 were 0.5 mol/l and 30 wt%, respectively. Establishing the microemulsion decreased the temperature to 4°C. In the case of low water-to-surfactant ratio R_w, i.e. high concentration of CTAB, the acidity decreased to the point where $[Co(H_2O)_6]^{3+}$ complex could form, giving microemulsion 1 a blue colour. The microemulsion containing $(CH_3)_4NOH$ was then slowly added to the salt-containing microemulsion until pH = 12.0, leading to the formation of hydroxides according to Equations 2.10–2.11. The strong basic environment produces $[Co(H_2O)_6]^{4+}$ and $[Co(H_2O)_6]^{3+}$ complexes of dark blue colour. The ammonium salt stabilizes these complexes, hence precipitation does not occur until the addition of the third microemulsion with H_2O_2. In Synthesis B, the precipitate maintains a green shade, which is probably due to $CoBr_2$ formed with CTAB. As the halogen salt is continuously washed out, the colour changes to brown. NP were washed in water, containing a few drops of NH_3, followed by washing them twice in pure water and twice in a mixture of water and acetone. Lastly, the NPs were washed again in pure water and in ethanol. Then the ethanol was evaporated and the remaining solids heated under vacuum ($p < 0.001$ mbar) up to 180°C for two hours in order to break down the organic ligands.

Varying R_w in Synthesis A from 5 to 30 and the precursor salt concentration from 0.11 mol/l to 0.43 mol/l (Ref. [192]), resulted in NP samples with average diameter $9.5 \leq \langle s \rangle \leq 19.5$ nm. In Synthesis B, different R_w resulted in NP samples with average diameter $12 \leq \langle s \rangle \leq 37$ nm.

For $La_{1-x}Sr_xMnO_3$ nanoparticles, only Synthesis B was used. The precursor salts were $La(NO_3)_3 \cdot 6\,H_2O$ and $Mn(NO_3)_2 \cdot 4H_2O$, obtained from Sigma Aldrich. The synthesis was done exactly as decribed above, the only difference being the direct precipitation of brown hydroxides upon adding the second microemulsion with $(CH_3)_4NOH$ [193].

$$Mn^{2+} + 2OH^- \longrightarrow Mn(OH)_2 \downarrow \tag{2.13}$$

$$\overset{+II}{Mn}(OH)_2 \xrightarrow{O_2} \overset{+III}{Mn}O(OH) \tag{2.14}$$

Although $Mn(OH)_2$ oxidises using oxygen from air, adding the third microemulsion with H_2O_2 speeds up the reaction and was found to avoid the formation of Mn_3O_4 [194]. Different R_w resulted in NP samples with average diameter $19 \leq \langle s \rangle \leq 32$ nm.

In order to obtain the perovskite oxides from the amorphous hydroxide precipitates, heating under oxygen flow is performed. The reactions are summarized as follows:

$$2La(OH)_3 + Co_2O_3 \cdot xH_2O \xrightarrow{O_2,600^\circ C} 2LaCoO_3 + (3+x)H_2O \uparrow \tag{2.15}$$

$$(1-x)La(OH)_3 + xSr(OH)_2 + MnO(OH) + \frac{x}{4}O_2 \xrightarrow{O_2,850^\circ C} La_{1-x}Sr_xMnO_3 + (2-\frac{x}{2})H_2O \uparrow \tag{2.16}$$

2.1.2 Agglomeration Prevention

A large drawback of the microemulsion method is the amorphous character of nanoparticles precipitated at room temperature. To induce crystallization, $LaCoO_3$ has to be heated to at least 550°C [195] and $La_{1-x}Sr_xMnO_3$ to at least 750°C. As ionic mobilities are high enough for diffusion at these temperatures, crystallization is accompanied by sintering and particle growth at the expense of smaller particles. Several methods have been applied to avoid sintering and particle growth.

Firstly, nanoparticles can be dispersed in an organic liquid that decomposes at high temperatures to carbon [196, 197]. The carbon matrix is thought to prevent diffusion, but burn off at higher temperatures. It was found that in the present set-up this approach neither prevents agglomeration and sintering, nor does the carbon react fully with the provided oxygen, hence there is an excessive carbon residue contaminating the product.

Secondly, Ref. [126] and Ref. [38] suggest coating $La_{1-x}Sr_xMnO_3$ nanoparticles in SiO_2 by the Stober process, and remove it after calcination by HF etching. It was found, however, that this method results in LaF_3 as the primary phase, not $La_{1-x}Sr_xMnO_3$. Furthermore, a study on the variation of calcination temperature shows clearly that Si-Sr phases crystallize at lower temperatures than $La_{1-x}Sr_xMnO_3$, hence severely changing the composition of the amorphous material and preventing the perovskite formation.

Finally, the only method to achieve a high surface-to-volume ratio is freeze-drying, as suggested by Refs. [198, 199]. A dispersion of amorphous nanoparticles in water (dispersion was achieved by long ultrasonication) is sprayed into liquid nitrogen. The rapid freezing avoids re-arrangement of nanoparticles and they remain well separated by ice. Raising the temperature to -15°C at pressure $p \leq 0.008$ mbar leads to sublimation of the water. By avoiding the liquid phase, nanoparticles stay far apart as no capillary pressure is exerted on the loosely connected network. This does not avoid the formation of soft agglomerates, but it ensures a high porosity and hence high surface area.

2.2 Morphological and Structural Characterization

2.2.1 Scanning Electron Microscopy

Although the samples have a low conductivity and charging under the electron beam makes imaging with SEM difficult, no conductive coating of carbon or gold could be applied due to the small NP size. All SEM measurements were conducted using a Leo 900 microscope with field-emission gun.

Size analysis was performed by the image analysis software ImageJ, which makes it possible to manually select a brightness threshold to differentiate between pixels belonging to a particle and pixels belonging to the background. On average, 50-130 NPs could be investigated per sample. Using the SEM scale bar, the projected particle cross-section area in pixels can be converted to the area in nm^2. Assuming spherical nanoparticles, this area can be converted to an approximate average diameter $\langle s \rangle_{SEM}$. The size of the particles is thus underestimated, since TEM analysis shows clearly non-spherical particles. Additionally, SEM is not sensitive to crystallinity which can lead to a difference in observed nanoparticle size and crystallite size. The resolution limit for this type of

material is about 6 nm, which limits the accuracy of measurement at small sizes. Both materials were investigated in SEM and TEM, but for $LaCoO_3$ the nanoparticle size was too small and the conductivity too low to allow high resolution imaging with SEM. Here, transmission electron microscopy (TEM) is required.

2.2.2 Transmission Electron Microscopy

Transmission electron microscopy (TEM) and high-angle annular dark-field scanning transmission electron microscopy (HAADF-TEM) were performed on a Titan 800, alongside electron-energy loss spectroscopy (EELS) and energy dispersive X-ray spectroscopy (EDX). $LaCoO_3$ samples were imaged by Dorothée Vinga Szabó, whereas $La_{1-x}Sr_xMnO_3$ measurements were taken by Houari Amari, both members of the Kübel group at the Institute of Nanotechnology, KIT.

The particle size can be measured in bright-field (BF), as well as dark-field (DF) modes. In TEM DF, the direct electron beam path is blocked, and only electrons diffracted by a crystal structure are used to create the image. In dynamic DF, the position of the aperture permitting the beam to pass is rotated along one of the diffraction circles faster than the aquisition time. This results in all crystallites lighting up in the image, as during the aquisition time each of them is favourably oriented at least once, so that crystals with different orientations could be included in the analysis. Amorphous parts, on the other hand, would remain dark, as they do not diffract. Therefore the $LaCoO_3$ NP size $\langle s \rangle_{\mathrm{TEM}}$ is the average size of the NP crystallites assuming isotropic angular orientation of NPs, which can be weakly agglomerated. The size analysis was carried out using the software package ImageJ, where the size of the bright spots are used as the projected cross-section area of the NP. For each sample, 15-100 NP were measured to compute the average size $\langle s \rangle_{\mathrm{TEM}} = 2 \times (3A/4\pi)^{1/3}$, assuming spherical shape.

Energy-dispersive X-ray (EDX) spectroscopy was carried out with TEM, as well. The incident electron beam results in the loss of an electron from the core level of an atom in the sample. When a higher-level electron recombines with the hole, the energy difference is emitted as X-rays with element-specific energies. This procedure allows for the identification of elements in the sample. With careful calibration, semi-quantitative analysis is also possible for elements with $Z \geq 9$. For La:Co, the different atomic weights of La and Co result in a difference of scattering angle and therefore the intensity ratio can be expected to vary as a function of tilting angle of the sample surface with respect to the detector. Since the machine is not calibrated with respect to the La:Co ratio, EDX cannot be used to determine this ratio. For $La_{1-x}Sr_xMnO_3$ on the other hand, calibration was available, and therefore the La:Sr ratio derived from Rietveld refinement of XRD spectra could be checked against TEM-EDX measurements.

Quantitative information on oxygen content cannot be obtained by EDX because the atomic number is too small. An alternative technique is electron-energy loss spectroscopy (EELS), where the difference in energy of emitted electrons and detected electrons is used to identify the energy of absorbed electrons. This energy is element-specific as it corresponds to inter-band transitions. The oxygen deficiency is quantized using parameter δ, i.e. the deviation from the ideal oxygen stoichiometry in the more detailed chemical formula $La_{1-x}Sr_xMnO_{3-\delta}$. In the present case, the oxygen stoichiometry could only be

measured relatively between different locations on one sample or between samples, since $\delta \approx 0$ and the δ detection limit of EELS in the present case is ± 0.1.

2.3 Structural Analysis

2.3.1 X-Ray Diffraction

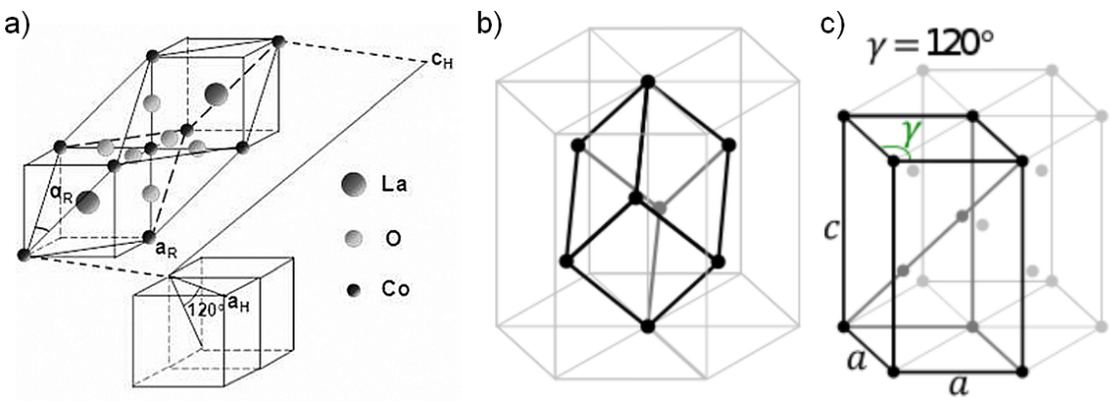

Figure 2.3: a) The definition of the rhombohedral unit cell in the pseudocubic crystal structure [200]. The $[CoO_{6/2}]^{3-}$ octahedron is shown where the two original cubic unit cells meet. c_H and a_H are the lattice parameters of the trigonal unit cell shown in (c). b) The definition of the rhombohedral unit cell within the hexagonal crystal structure and c) the trigonal unit cell in the hexagonal crystal structure.

As mentioned in the introduction, $LaCoO_3$ and $La_{1-x}Sr_xMnO_3$ (for $x \geq 0.175$) both have pseudocubic, rhombohedral crystal structure: The tilting of the octahedra results in doubling of the original cubic unit cell, and instead of a cubic symmetry, a rhombohedral one is obtained. This is shown in Fig. 2.3 (a), with the $[CoO_{6/2}]^{3-}$ octahedron in the centre. The rhombohedral lattice parameter $a_R = \sqrt{2}a_C$ is the face diagonal of the cubic unit cell. Instead of the rhombohedral setting, the trigonal setting can be used, which results in defined angles $\alpha = \beta = 90°$, $\gamma = 120°$. The relationship between the rhombohedral and the trigonal settings is shown in Fig. 2.3. The trigonal lattice parameters a and c are marked in Fig. 2.3(a) as a_H and c_H. These are the lattice parameters used below.

Powder X-ray diffraction (XRD) was carried out at room temperature in transmission mode using a STOE two-circle X-ray diffractometer employing Mo K_α radiation. The powder patterns were measured in the 2θ range between 5 and 50°, and Rietveld refinement was employed by Michael Merz using the FULLPROF program package [201] to obtain the lattice parameters and the atomic positions, as well as the La:Sr ratio for $La_{1-x}Sr_xMnO_3$. This is an iterative technique to refine diffraction profiles by varying the position of the atoms in a pre-defined space group, in this case $R\bar{3}c$. The refined parameters are the positions of the atoms in relative coordinates of the unit cell and the site occupancy factor based on fitting the intensity of the peaks.

2.3.1.1 La/Sr ratio

Analytical techniques determining the chemical composition include atomic absorption spectroscopy (AAS) and inductively-coupled plasma optical emission spectroscopy (ICP-OES). AAS could not be performed because of the low amount of $La_{1-x}Sr_xMnO_3$ obtained from microemulsion synthesis, and ICP-OES was attempted, but led to results with the Sr concentration x measured to be $x \leq 1\%$. This is not only inconsistent with the values obtained from XRD and TEM-EDX, but also with the magnetic properties discussed below. Instead, the La:Sr ratio was analysed using Rietveld refinement on XRD patterns, based on refining the atomic scattering factors $f_j(\mathbf{q})$. The following two expressions consider the scattering factor $f_j(\mathbf{q})$ and the scattering density $f_j(\mathbf{x})$ for the j-th electron of an atom along vector $\mathbf{x}$:

$$f_j(\mathbf{q}) = \int \rho_j(\mathbf{x}) \exp(\mathbf{q} \cdot \mathbf{x}) \mathrm{d}x \tag{2.17}$$

$$f_j(\mathbf{x}) = \int \rho_j(\mathbf{x}) \exp(-2\pi i d_{hkl} \cdot \mathbf{x}) \mathrm{d}x \tag{2.18}$$

where the scattering vector $\mathbf{q}$ can be expressed as a function of d_{hkl}, the lattice spacing. The total intensity of the coherent scattering, I_{coh} is then a function of the sum over all the atom's electrons [202]:

$$I_{\mathrm{coh}} = \left(\sum_{j=1}^{Z} f_j \right)^2 I_{\mathrm{Thompson}} \tag{2.19}$$

Being a function of the electron density distribution taken from the origin, i.e. the atomic nucleus, the scattering factors are characteristic of elements. Their refinement can therefore yield the ratio of atoms of different elements in the same crystallographic position.

2.3.1.2 Crystallite size analysis

Additionally, XRD patterns are used to calculate the crystallite size. According to Scherrer's equation, the peak profile is broadened on top of the instrumental broadening if the crystal size is very small ($\langle s \rangle \leq 10^{-7}$ m). The relationship between the additional peak broadening β_{D} (in addition to the instrumental broadening) and the crystallite size measured perpendicularly to the incoming X-ray beam D is as follows [203, 204]:

$$\beta_{\mathrm{D}} = \frac{K\lambda}{D \cos\theta} \tag{2.20}$$

where K is a constant between $0.87 \leq K \leq 1.0$ depending on particle shape and crystal symmetry. The $LaCoO_3$ and $La_{1-x}Sr_xMnO_3$ nanoparticles studied here have a rhombohedral crystal structure and aspect ratio close to 1. Here, $K \approx 1$ for simplicity, as the variation in calculated size for $0.87 \leq K \leq 1.0$ is well within the uncertainty from the

fitting. λ is the wavelength of the Mo K_α radiation used ($\lambda = 0.707$ Å) and θ the diffraction angle.

However, the diffraction lines are not just broadened by the small NP size, but also by the fact that the lattice plane distance d_{hkl} is not always the same throughout the nanoparticles due to surface strain and crystal defects. The defect density can be much higher in nanoparticles due to the soft synthesis conditions used in order to avoid crystal growth. Broadening due to strain, β_e can be calculated by differentiating Bragg's Law [205, p. 264], leading to:

$$\beta_e = \Delta 2\theta = -2\frac{\Delta d}{d}\tan\theta \tag{2.21}$$

These relationships allow the two effects to be separated according to Ref. [206], where the expression on the right-hand side of Eq. 2.21 is replaced by its double and absolute value, since the relative change of the lattice spacing $\Delta d/d$ involves both tensile and compressive strain:

$$\beta_{NP} = \beta_D + \beta_e \tag{2.22}$$

$$\beta_{NP} = \frac{K\lambda}{D\cos\theta} + 4\varepsilon\tan\theta \tag{2.23}$$

$$\beta_{NP}\cos\theta = \frac{K\lambda}{D} + 4\varepsilon\sin\theta \tag{2.24}$$

Therefore, plotting $\beta_{NP}\cos\theta$ against $\sin\theta$ and fitting a linear equation to the data allows estimating the average nanoparticle size and the internal strain from the intercept and the slope, respectively. An exemplary Williamson-Hall-Plot is shown in Fig.

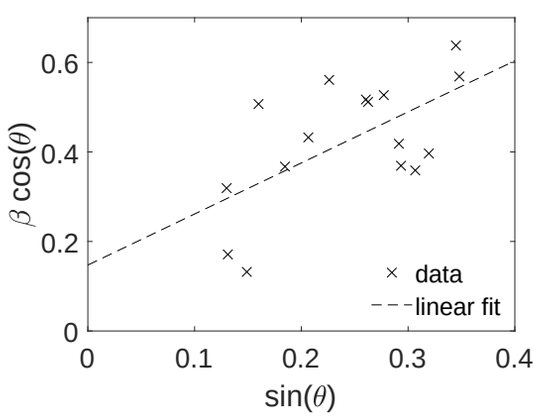

Figure 2.4: Williamson-Hall-Plot for a $LaCoO_3$ sample with $\langle s\rangle = 9.5$ nm.

The resulting nanoparticle size is double-checked against the size seen in electron microscopy images (TEM and SEM).

From the analysis a mean particle size $\langle s\rangle_{XRD}$ and fitting error Δs_{XRD} were obtained. The surface-to-volume ratio S/V used hereafter was calculated for each sample using

the average diameter $\langle s \rangle_{\mathrm{XRD}}$ as deduced from XRD, again assuming spherical NPs, i.e. S/V= $(6\pi \langle s \rangle^2_{\mathrm{XRD}})/(\pi \langle s \rangle^3_{\mathrm{XRD}}) = 6/\langle s \rangle_{\mathrm{XRD}}$.

2.3.2 X-Ray Absorption Spectroscopy

2.3.2.1 Near Edge X-Ray Absorption Fine Structure Spectroscopy

When incoming X-ray photons have the same energy as the energy required to excite a core electron into the lowest empty state, there is a sharp rise in the absorption, called the absorption edge [207]. In XAS, the linear absorption coefficient is measured [208]:

$$I(t) = I_0 e^{-\frac{\mu}{\rho}\rho t} \tag{2.25}$$

with the mass absorption coefficient

$$\frac{\mu}{\rho} = \sum_i w_i \left(\frac{\mu}{\rho}\right)_i \tag{2.26}$$

A Lorentzian broadening is the result of finite lifetime of the core hole, which according to Heisenberg's uncertainty principle leads to an uncertainty of the energy [209]. The transition probability of an electron is described by Fermi's Golden Rule [210]:

$$I \propto |\langle \psi_{\mathrm{f}} | \hat{e}r | \psi_{\mathrm{i}} \rangle|^2 \delta(E_{\mathrm{f}} - E_{\mathrm{i}} - h\nu) \tag{2.27}$$

where $\hat{e}r$ is the squared dipole matrix element and $|\psi_{\mathrm{i}}\rangle$ and $|\psi_{\mathrm{f}}\rangle$ are the initial and final states, respectively.

In the dipole approximation, which works reasonably well for the K edges, the shape of the absorption spectrum maps the partial density of empty states projected onto the absorption site. For L edges, the core wave functions strongly overlap with the valence wave functions, which results in multiplet effects between core holes and partially filled valence bands. The absorption spectrum of $3d$ ions is therefore sensitive to the multiplet structure given by the $3d$-$3d$ and $2p$-$3d$ Coulomb and exchange interactions. Additionally, the local crystal field and degree of hybridization with the O $2p$ ligands influences the spectrum [51, 207]: The spin-orbit coupling results in a splitting of the energy levels according to the value of J, $|L-S| \leq J \leq L+S$, with a degeneracy of $2J+1$. Assuming the transition-metal state $3d^n$, the core hole, $2s$ or $3p$ will result in configurations $2s^1 3d^{n+1}$ and $3p^5 3d^{n+1}$. If $n = 3$, the possible spin states are a doublet and a quartet state. The intensity of the spectral peak then depends on the degeneracy, i.e. the multiplicity of the final state and the selection rules. The relative energy of the configuration terms is calculated from the matrix elements of the electron-electron interaction and the spin-orbit coupling, with the general formula [207]:

$$\langle {}^{2S+1}L_J | \frac{e^2}{r_{12}} | {}^{2S+1}L_J \rangle = \sum_k f_k F^k + \sum_k g_k G^k \tag{2.28}$$

Here, $F^k(f_k)$ and $G^k(g_k)$ are the Slater-Condon parameters for the direct Coulomb repulsion and the Coulomb exchange interaction, respectively, with f_k and g_k only non-

zero for specific values of k. The left part of the equation corresponds to the matrix element in Equation 2.27, i.e. $|\psi_f\rangle = |^{2S+1}L_J\rangle$.

During X-ray absorption, an electron from the $2p$ state is transferred to a $3d$ orbital. The energy of the final state is a function of the Slater-Condon parameters, the spin-orbit coupling of $2p$ and $3d$, and the transition matrix elements for the X-ray absorption can be calculated using [207]:

$$I_{XAS} \propto \langle 3d^n | \overrightarrow{r} | 2p^5 3d^{n+1} \rangle^2 \tag{2.29}$$

The number of final states $|2p^5 3d^{n+1}\rangle$ is determined by the dipole selection rules, which state that $\delta J = \pm 1$ or 0, unless $J' = J = 0$. The overall spectral shape is then determined by the ratio of the core spin-orbit coupling and the Slater-Condon parameter F^2. Finite values of both result in the existence of a pre-peak [207]. Hybridization effects can be taken into account, leading to satellites [211].

Applying the analysis to XAS spectra of $LaCoO_3$, the spin states of $LaCoO_3$ can be analysed by Near-Edge X-ray Absorption Fine Structure (NEXAFS) spectroscopy. With reasonably well studied compounds such as $LaCoO_3$, analysis of structural parameters can be done relative to the known parent compound [74]. The measurements were carried out at IFP's beam line WERA at the synchrotron light source ANKA at KIT by members of the Schuppler group at the Institute for Solid State Physics. Multiplet fits were done by Michael Merz and Meng-Jie Huang.

2.3.2.2 X-ray Circular Magnetic Dichroism

If the same absorption spectra are measured once with right circularly polarized light and once with left circularly polarized light, the spectra are different if the sample is magnetically polarized. The X-ray Circular Magnetic Dichroism (XMCD) is the difference between the two spectra [212]. In a simplified model, the $2p$ core level is split into a state with $j = 3/2$ (L_3 edge) and a state with $j = 1/2$ (L_2 edge). Spin and orbital moments for the two states are coupled parallel and anti-parallel, respectively. Therefore, if the light helicity vector is parallel (antiparallel) to the $2p$ orbital moment, the excited electrons are preferentially spin up (spin down). As these excited electrons have to match holes on the $3d$ level, the availability of spin up and spin down holes at the $3d$ level determines whether L_3 and L_2 are positive or negative [211]. Consequently, the amount of dichroism is directly related to the strength of spin-orbit coupling, since part of the angular momentum of the photoelectron can be transferred to the spin by spin-orbit coupling [213].

The absorption coefficients for right and left circularly polarised light, μ^+ and μ^-, respectively, are obtained after subtracting the background [212]. Since the polarized light couples to the orbital moment, spin and orbital moments can be analysed separately, using sum rules [47]:

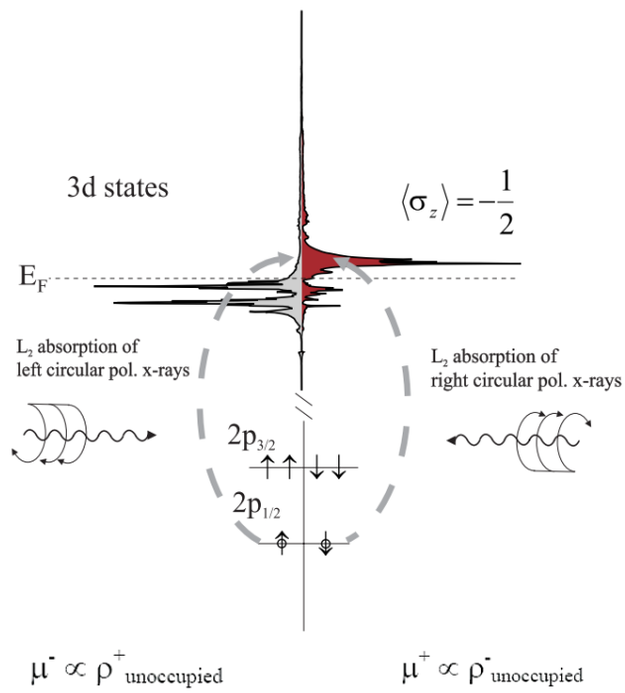

Figure 2.5: Schematic representation in the one-electron picture of L_2 absorption using left and right circularly polarized light in a $3d$ compound [214].

$$m^{\phi}_{\text{orb}} = -4\frac{(\Delta A_{L_3} + \Delta A_{L_2})_{\phi}}{3(A_{L_3} + A_{L_2})} n_h \tag{2.30}$$

$$m_{\text{eff}} = m_{\text{spin}} + 7m^{\phi}_{\text{T}} = -\frac{(2\Delta A_{L_3} - 4\Delta A_{L_2})_{\phi}}{A_{L_3} + A_{L_2}} n_h \tag{2.31}$$

where m^{ϕ}_{orb}, m_{spin}, m^{ϕ}_{T}, and m_{eff} are in units of μ_{B}/atom and describe the orbital and spin magnetic moments, the magnetic dipole moment, and the effective magnetic moment, respectively. $n_h = 10 - n_{3d}$, with n_{3d} being the $3d$ electron occupation number, and ΔA_{L_3} and ΔA_{L_2}, and A_{L_3} and A_{L_2} are the XMCD and NEXAFS intensities integrated over the L_3 and L_2 edge, respectively. Sample measurement and spectrum analysis was conducted by Meng-Jie Huang, Schuppler Group.

NEXAFS and XMCD measurements were carried out at IFP's beam line WERA at the synchrotron light source ANKA at KIT.

2.4 Magnetic Measurements

Superconducting quantum interference devices (SQUIDs) use Josephson junctions to measure small magnetic moments at high sensitivity. When Cooper pairs tunnel through

a Josephson junction resulting in a supercurrent $I = I_0 \sin\delta$, there is a phase change δ across the boundary. A superconducting loop with two Josephson junctions in path A and path B leads to screening currents in the presence of the external field, because superconductors expel magnetic fields according to the Meissner-Ochsenfeld effect. The screening current I_S modifies the currents in the two branches. In branch A, the current is now $I/2 + I_S$ and in branch B the current is $I/2 - I_S$. As soon as the critical current I_C is exceeded in one of the branches, a voltage is generated across the junction.

The high sensitivity comes from the change in direction of the screening current if the external flux exceeds half the magnetic flux quantum ϕ, because a superconducting ring can only enclose integer numbers of flux quanta, hence the system adds flux if $\phi_{ext} \geq \phi/2$. With a shunt resistance R, the voltage drop due to a change in current is $\Delta V = R\Delta I = R/L \times \Delta\phi$, with L being the inductance of the superconducting ring.

Both field- and temperature-dependent magnetization measurements were first performed without any sample to obtain reference curves for the diamagnetic sample holder. These background curves were subtracted from the measured data before analysis. Each measurement was preceded by heating the sample to $T = 300$ K and cooling to the measurement temperature in zero magnetic field. NPs can have superparamagnetic behaviour, in which case a large magnetic moment but no hysteresis is expected. As shown in Table 3.1, the highest average magnetic moment that was measured is only 0.18 μ_B/Co at 7 T and 5 K, taking into account that XRD patterns such as the one shown in Fig. 3.1 confirm that all of the measured material is $LaCoO_3$. Hence, the low magnetic moment indicates paramagnetic behaviour, which can be described by a Brillouin function.

$$m_{Co^{3+}} = N_{Co^{3+}} g_J J \mu_B \mathcal{B}_J(x) \tag{2.32}$$

where $N_{Co^{3+}}$ is the number of contributing ions, $\mathcal{B}_J$ is the Brillouin function for J and x the dimensionless ratio of the Zeeman energy $\mu_0 g \mu_B M_j H$ to the thermal energy $k_B T$. The Brillouin function is defined as follows:

$$\mathcal{B}_J(x) = \frac{2J+1}{2J} \times \coth\left(\frac{2J+1}{2J}x\right) - \frac{1}{2J} \times \coth\left(\frac{1}{2J}x\right) \tag{2.33}$$

In an octahedral environment ligand field theory predicts fully quenched orbital moments leading to $J = S = 2$ for Co^{3+} HS. This is in contrast to the results of Ref. [51], and XMCD measurement on one of the nanoparticle samples, where the ratio of orbital moment to spin contribution was $m_{orb}^{av}/m_{spin} = 0.5$ and $m_{orb}^{av}/m_{spin} = 0.7$, respectively. Therefore, J is chosen as $\tilde{J} = 1$, with the Landé factor $g = 3.2$.

In order to fully describe the measured curves, H in Equation 2.32 has to be replaced by $H + H_i$, where H_i is an internal field and a free fitting parameter. The fitting is performed using MathWorks®Matlab's "*fmincon*" problem minimizer: the fitting parameters of a given function are modified until a minimum in the difference between data and fit is reached. For stability, the "*sqp*" algorithm is used, and boundary values are specified. Typical R^2 values are of the order of 1×10^{-4} and the parameters are evaluated with an accuracy of $R^2 = 10^{-3}$.

2.5 Thermogravimetry

In order to analyse the surface adsorption characteristics of $La_{1-x}Sr_xMnO_3$ and $LaCoO_3$, thermogravimetric analysis was carried out using a SSC/5200 analyser from Seiko Instruments. The mass of the sample is monitored against the reference mass of an empty crucible made from the same material (Al_2O_3) as the temperature is increased from room temperature to 600°C at a rate of 10°C/min. Once the maximum temperature is reached, the sample is held for 20 min before cooling down at the same rate of 10°C/min. The measurement is performed in air. The measured curves are normalized to the total mass of the sample at the beginning of the analysis. Prior to sample analysis, a zero measurement with empty crucibles was conducted to obtain the baseline, which is then subtracted from the measured data.

3 Results

3.1 Morphology, chemistry, and crystal structure

In order to relate physical properties such as magnetic moment or T_C to the nanoparticle (NP) size, the uniformity of NP batches has to be confirmed first: The variation of size within one batch has to be low enough to quantify the relationship between NP size and physical properties. Another important aspect is crystal quality: defects can have a strong influence on both structure and magnetism. Therefore, if the defect density varies between batches, it is no longer possible to talk of purely size-dependent changes in physical properties. Additionally, each NP batch has to be single-phase and contain no significant amount of amorphous material: the magnetization measurements are related to the sample mass, assuming all of the material is $LaCoO_3$ or $La_{1-x}Sr_xMnO_3$, respectively. Significant amounts of impurities lead to an underestimation of the magnetic moment. Clearly, there can be no variation in chemistry within one batch either. The above conditions result in strict selection of synthesized samples: only 7 out of 24 batches were analysed for $LaCoO_3$ and 6 out of 8 for $La_{1-x}Sr_xMnO_3$ NPs.

3.1.1 $LaCoO_3$

3.1.1.1 Crystal quality

The low calcination temperature used to control the nanoparticle size during crystallization can lead to significant amounts of crystalline defects and impurity phases such as La_2O_3 and Co_3O_4 both in crystalline and amorphous forms. An XRD pattern of a $LaCoO_3$ nanoparticle powder sample with $\langle s \rangle_{XRD}$ = 9.5±2 nm is shown as an example in Fig. 3.1. While displaying excellent phase purity without any secondary crystalline phases, this pattern has a high background, which could be related to amorphous material, carbon residue or indicate the large amount of surface, which is different from bulk. If there is amorphous material, it is the same for all samples, because the relative intensity of the background is the same for all XRD patterns. Additionally, TEM DF images could reveal the presence of amorphous matter by showing areas which are never bright during rotation of the aperture along the diffraction circle. Moreover, amorphous material would result in continuous circles in the selected-area diffraction patterns, which was not observed in Fig. 3.2(e) and (f) in the insets. For the samples analysed, no amorphous matter was found, which suggests that the high background in XRD spectra is due to nanoscopic size and/or differently ordered or disordered surface material.

High resolution transmission electron microscopy was used to identify defects such as stacking faults or dislocations. In $LaCoO_3$, NPs are fully crystalline with no visible amorphous shells. In Fig. 3.2 TEM-BF, TEM-DF, and high resolution TEM images are shown

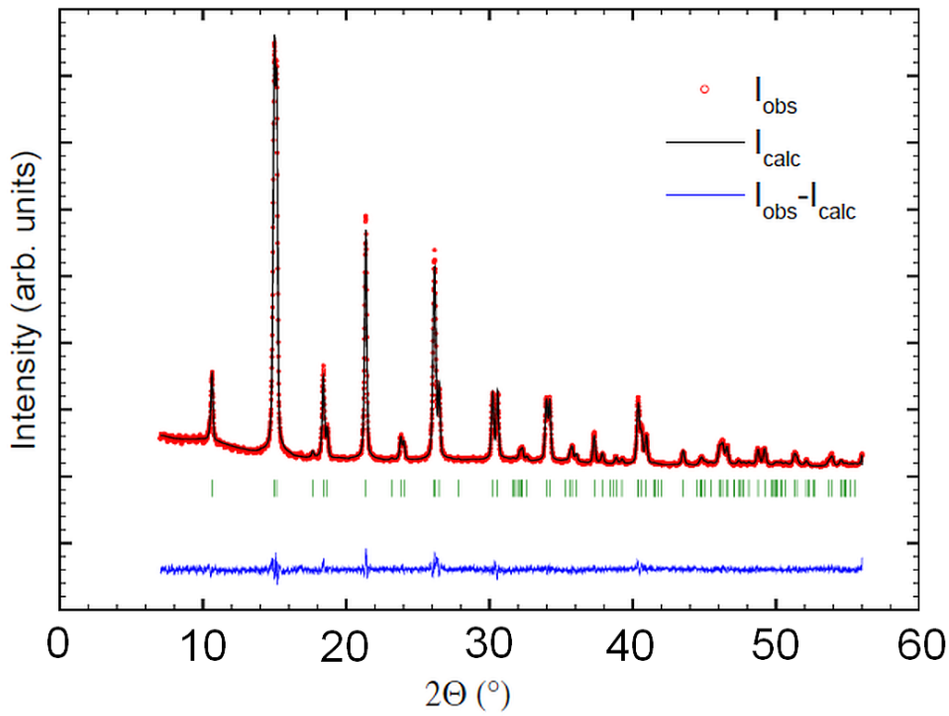

Figure 3.1: XRD pattern of a $LaCoO_3$ nanoparticle powder sample with $\langle s \rangle_{XRD} = 9.5 \pm 2$ nm (open circles) The Rietveld refinement (black line), and their difference (blue line). The refined position of the peaks is marked by green bars.

along with selected area electron diffraction (SAED) patterns for $LaCoO_3$ nanoparticles with $\langle s \rangle = 37$ nm and $\langle s \rangle = 13.5$ nm. The stacking faults seen for $LaCoO_3$ nanoparticles with $\langle s \rangle = 37$ nm are induced by electron-beam irradiation. The large particles in the overview images are made up of small crystallites, as revealed in dark-field images.

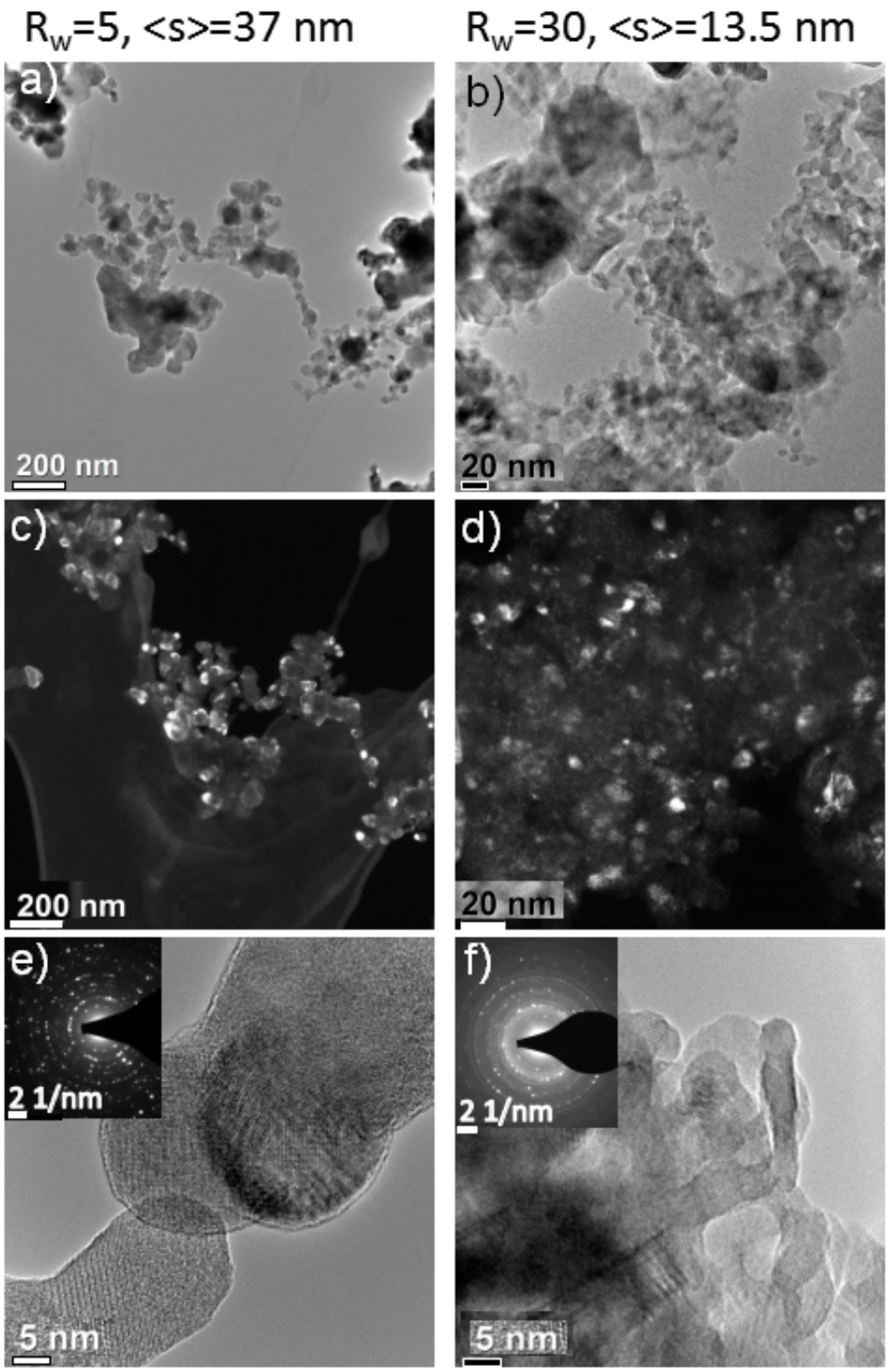

Figure 3.2: (a) and (b) Bright-field transmission electron microscopy images of NP powder samples at low magnification, (c) and (d) dark-field images and (e) and (f) high-resolution bright-field images with selected-area electron diffraction patterns in the insets for a sample with $LaCoO_3$ nanoparticles with $\langle s \rangle = 37$ nm ((a),(c) and (e)) and $\langle s \rangle = 13.5$ nm ((b),(d) and (f)).

3.1.1.2 Chemical composition

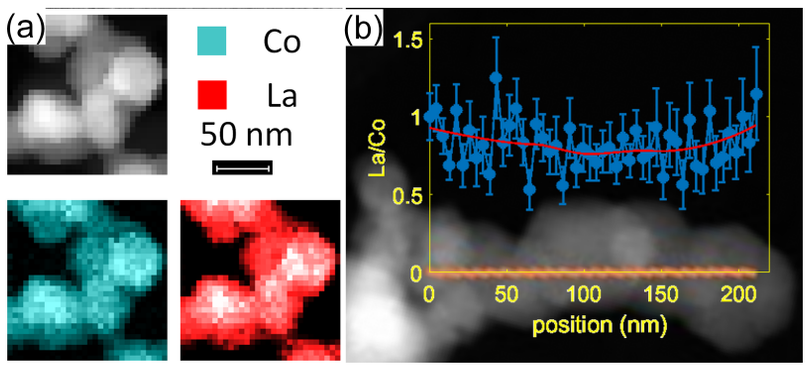

Figure 3.3: Energy-dispersive X-ray spectroscopy (a) map with split channels for Co (blue) and La (red) for a sample with $\langle s \rangle_{XRD}$ = 25 nm and (b) ratio of the intensities of the La-peak in the EDX spectrum to the intensity of the the Co-peak in the EDX spectrum as a function of position along a linear arrangement of nanoparticles shown in the background with $\langle s \rangle_{XRD}$ = 37 nm. The mean of the intensity ratio is plotted as a red line.

$LaCoO_3$ nanoparticles were studied in Transmission Electron Microscopy and EDX line scans and maps were recorded to show the chemical homogeneity of the samples on a microscopic scale. Exemplarily, the EDX map of a sample with $\langle s \rangle_{\mathrm{XRD}}$ = 25 nm is shown in Fig. 3.3(a). All the nanoparticles seen in the scanning transmission electron microscopy image (STEM) in grayscale, contain both Co and La. If the sample had a significant amount of Co_3O_4, some of the material would be invisible in the red image, as it contains no La. This confirms the X-ray diffraction results in Fig. 3.1, where no crystalline impurity phase was found, but also indicates that there are no amorphous impurities or impurity nanoparticles which are too small to be seen in diffraction, at least for the samples studied using TEM. Since only very small volumes of the sample can be analysed, the results cannot be confidently extrapolated to the entire sample.

Fig. 3.3(b) shows the ratio of the intensity of the La-related X-ray emission peak in the EDX spectrum to the intensity of the the Co-peak as a function of position along a linear arrangement of nanoparticles shown in the background. Since the EDX is not calibrated, the measured La:Co intensity ratio of slightly $\leq$ 1:1 is not a quantitative measure of the relative amounts of La and Co. The mean of the intensity ratio is plotted as a red line and appears to be changing slightly with position. This is most likely due to differences in angular scattering due to the different atomic masses of La and Co atoms. Within experimental accuracy, no significant variation of the La/Co ratio could be found. As there is also no indication for secondary phases in XRD, a homogeneous distribution of La and Co will be assumed in the following.

The high probability of oxygen stoichiometry deviation in perovskite materials [41] and the influence of oxygen vacancies on structural [215, 216] and magnetic properties [100, 101, 217] makes the parameter δ in $LaCoO_{3-\delta}$ and $La_{1-x}Sr_xMnO_{3-\delta}$ an important property.

However, chemical techniques such as titration could not be performed due to the low yield of NP from microemulsion synthesis.

For $LaCoO_3$, multiplet fits of NEXAFS at the Co L edge yields the concentration of Co^{3+} ions in the high-spin and in the low-spin states, and the concentration of Co^{2+} ions, which are formed in case of oxygen deficiency. Hence, the concentration of Co^{2+} ions can be used to calculate the parameter δ in $LaCoO_{3-\delta}$ by assuming double-positively charged oxygen vacancies $O_V^{\bullet\bullet}$. In this case, each Co^{2+} ion is balanced by $\frac{1}{2}O_V^{\bullet\bullet}$ due to charge neutrality. The resulting parameter δ is displayed in Table 3.3, and amounts to $\delta = 0.04 \pm 0.01$ and $\delta = 0.045 \pm 0.01$ for a sample with $\langle s \rangle = 9.5$ nm and a sample with $\langle s \rangle = 37$ nm, respectively. Therefore δ is not size-dependent within experimental accuracy.

3.1.1.3 Nanoparticle size

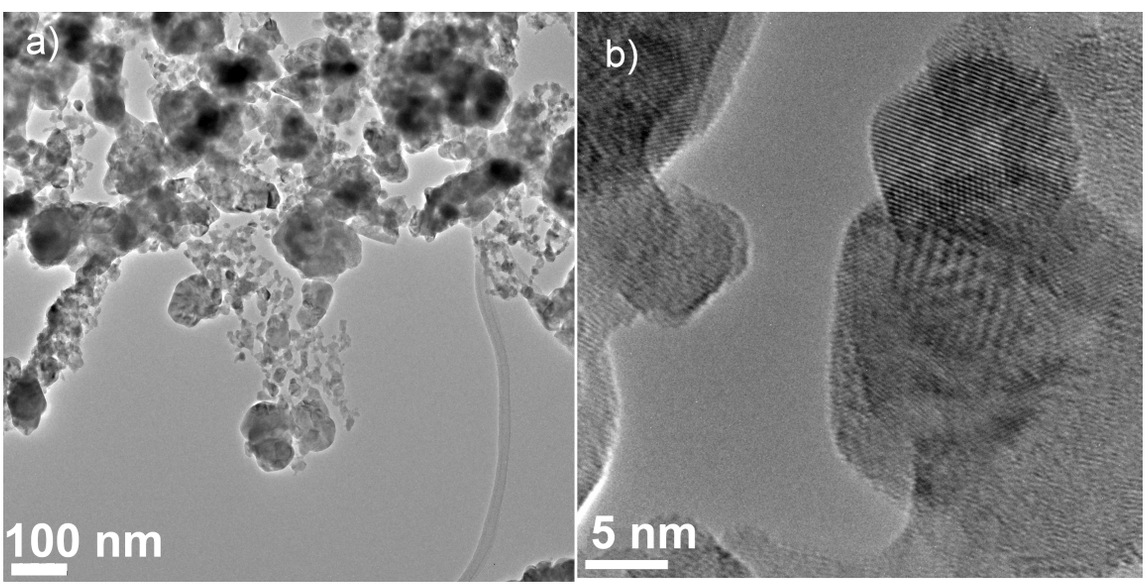

Figure 3.4: Transition Electron Microscope (TEM) bright-field (BF) image of a $LaCoO_3$ NP ensemble (a) at low magnification and (b) at high magnification.

The observed morphology of $LaCoO_3$ nanoparticle powders consists of individual crystallite grains with low aspect ratio. Although agglomeration of nanoparticles cannot be fully prevented, the individual nanocrystallites are well separated and no fusion occurred during sintering. An example of a $LaCoO_3$ ensemble is shown in Fig. 3.4. Particularly Fig. 3.4 (a) shows agglomeration and possibly coarsening into larger crystallites. Fig. 3.4(b), on the other hand, shows a faceted NP consisting of a single crystallite, and without any amorphous surface.

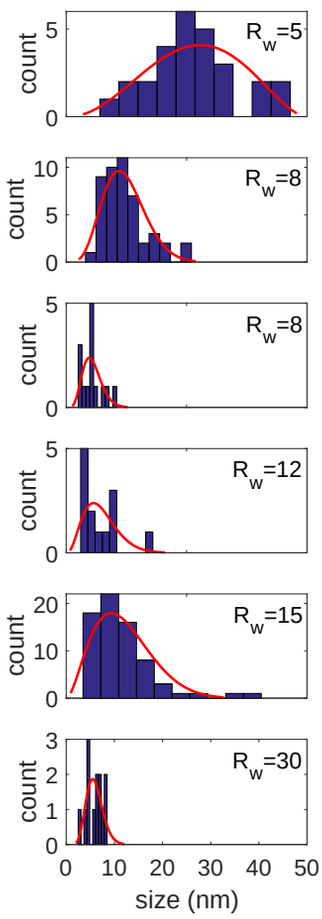

Figure 3.5: Number N of NPs vs s_{TEM} as obtained from TEM dark-field images for sample batches synthesized with different water-to-surfactant ratios R_w. The solid lines indicate lognormal fits to N vs s_{TEM}.

In order to evaluate the size distribution of individual NP crystallites, dark-field images were used (see Fig. 3.2(c) and (d)). The resulting histograms are displayed in Fig. 3.5, and the mean size $\langle s\rangle_{TEM}$ and the standard deviation σ_{TEM} are listed in Table 3.1. With $0.28 \leq \sigma s/\langle s\rangle_{\mathrm{SEM}} \leq 0.55$ the size distribution appears quite large, which is partially due to the low number of particles that were measured, but could also be related to agglomeration and sintering of nanoparticles during calcination [183]. The $LaCoO_3$ NP used for further analysis are listed in Table 3.1.

The NP size values obtained from XRD and TEM for $LaCoO_3$ given in Table 3.1 are the same within experimental error, which is to be expected as both methods are sensitive to the crystalline volume. The large experimental error on $\langle s\rangle_{\mathrm{TEM}}$ is a consequence of very few particles having been measured. In TEM, only very few very small regions can be analysed, and agglomeration makes it difficult to measure the particle size of individual crystallites in dark-field images. The TEM analysis under-estimates the nanoparticle size for all samples. This is an effect of assuming spherical shape for the nanoparticles, although they seem to be more faceted in reality (see Fig. 3.4).

Table 3.1: Physical properties, i.e. average size $\langle s\rangle$ determined from TEM and XRD, with the Gaussian fit standard deviation σ_{TEM} and Δs_{XRD} from the Williamson-Hall fit, respectively, structural parameters a, $d_{\text{Co-O}}$, $\theta_{\text{Co-O-Co}}$, and V_{uc} as obtained from Rietveld refinement, as well as the average magnetic moment $\langle m\rangle$(5K,7T) for various water-to-surfactant molar ratios R_w.

R_w	$\langle s\rangle_{\mathrm{TEM}}$ (nm)	σ_{TEM} (nm)	$\langle s\rangle_{\mathrm{XRD}}$ (nm)	Δs_{XRD} (nm)	a (Å)	$d_{\text{Co-O}}$ (Å)	$\theta_{\text{Co-O-Co}}$ (°)	V_{uc} (Å^3)	S/V (nm^{-1})	$\langle m\rangle_{(5K,7T)}$ (μ_{B}/Co)
5	26.6	9.3	37	7	5.440	1.931	164.1	335.8	0.16	0.08
8	5.4	2.1	19.5	4	NA	NA	NA	NA	0.31	0.11
8	12.1	4.6	19	3	5.440	1.933	163.5	336.0	0.32	0.12
12	7.2	4.0	9.5	2	5.441	1.936	163.3	337.5	0.63	0.18
15	NA	NA	12	2	5.433	1.933	162.9	335.0	0.50	0.15
15	11.6	6.5	12	2	5.436	1.936	161.8	335.5	0.50	0.15
30	5.9	1.7	13.5	2.5	NA	NA	NA	NA	0.44	0.15

3.1.2 $La_{1-x}Sr_xMnO_3$

3.1.2.1 Crystal quality

The crystal structure of $La_{1-x}Sr_xMnO_3$ NPs can be refined in the rhombohedral space group $R\bar{3}c$ and does not display any impurity phases. A typical XRD diffractogram is shown exemplarily in Fig. 3.6 for a sample prepared with $R_w = 7$. Rietveld refinement was carried out to extract lattice parameters $d_{\text{Mn-O}}$ and $\theta_{\text{Mn-O-Mn}}$ from the diffractogram (solid line in Fig. 3.6). The results are listed in Table 3.2.

Fig. 3.7 summarizes the results of TEM studies on two of the $La_{1-x}Sr_xMnO_3$ NP samples, synthesized with $R_w = 4$ and $R_w = 7$. Figs. 3.7(b) and (e) show that the nanoparticles are fully crystalline. Fig. 3.7(b) shows a thin amorphous shell, whereas the sample shown in Fig. 3.7(e) has no amorphous shell, but both sample batches exhibit low defect density: no stacking faults or dislocations can be identified. In the case of $La_{1-x}Sr_xMnO_3$ no stacking faults can be induced under e-beam irradiation. In contrast to $LaCoO_3$, the $La_{1-x}Sr_xMnO_3$ nanoparticles show atomically sharp facets with no remaining curvature. Although some particles, like the one shown in Fig. 3.7(e) appear slightly elongated, most have an aspect ratio close to 1. The lattice spacings indicated in Fig. 3.7(b) and (e) agree with the results from Rietveld refinement of XRD patterns.

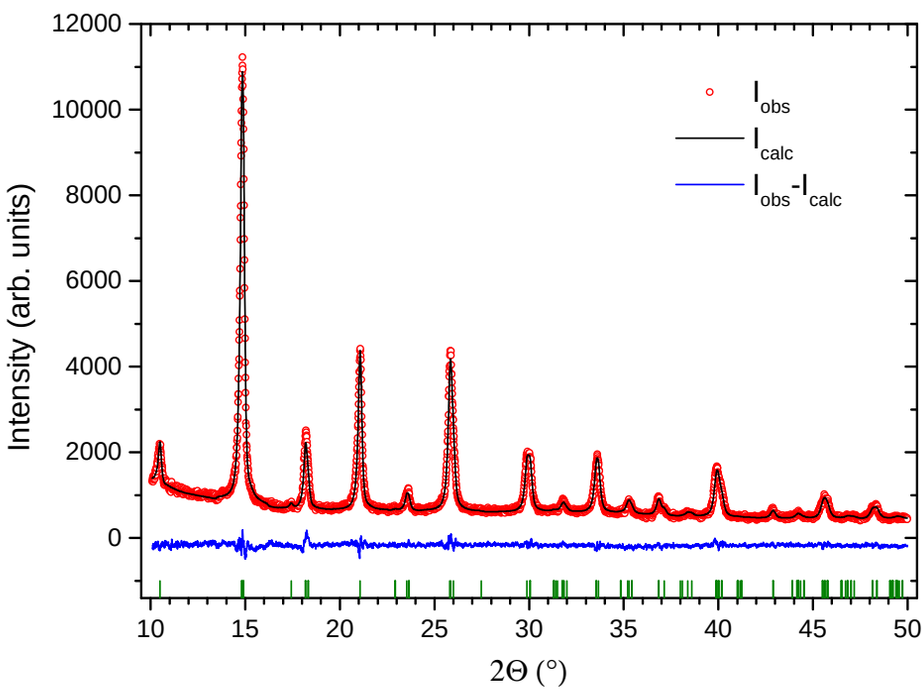

Figure 3.6: XRD of a $La_{0.63}Sr_{0.37}MnO_3$ NP sample with $R_w = 7$ (open circles), Rietveld refinement (black line), and their difference (blue line). The refined position of the peaks is marked by green bars.

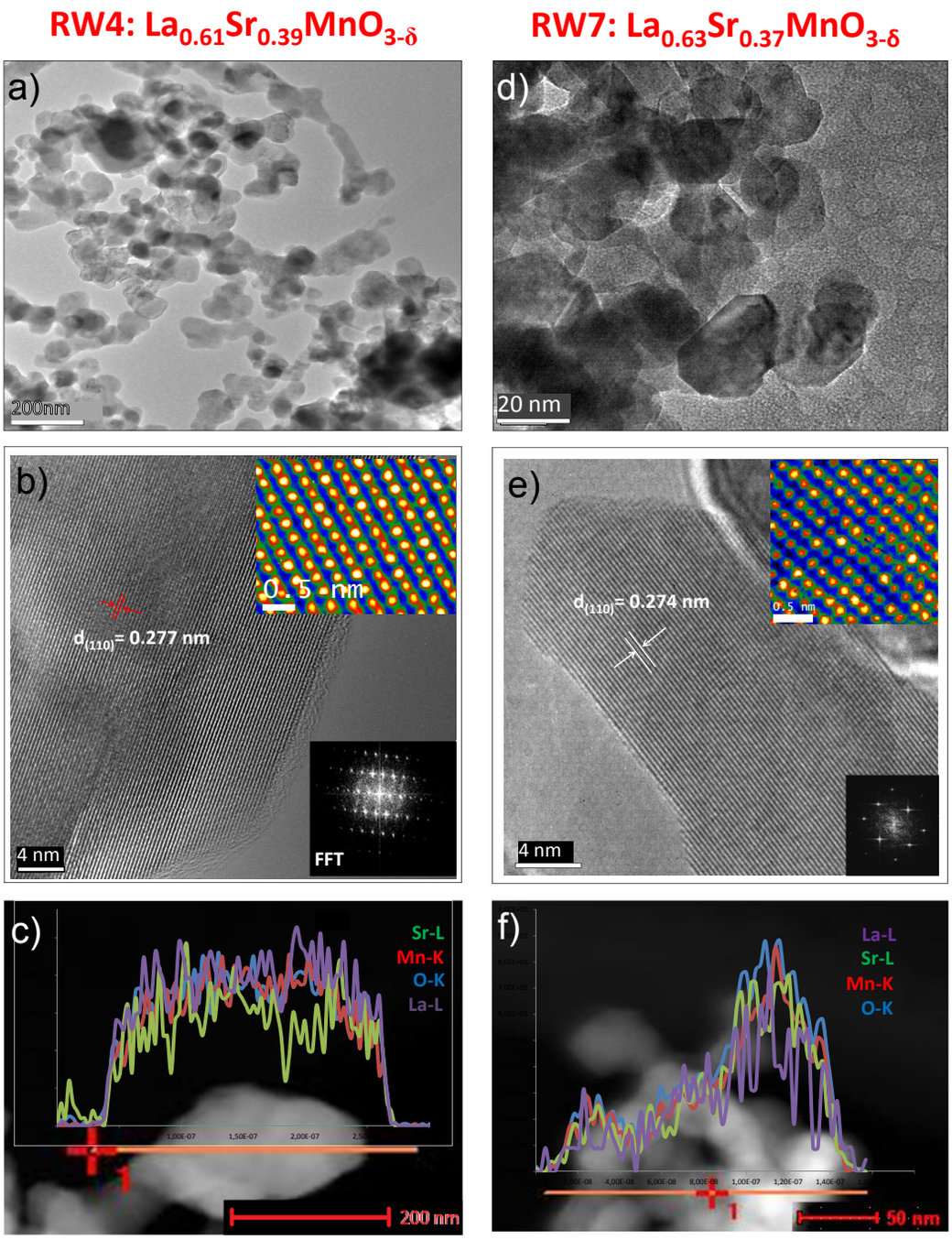

Figure 3.7: (a) and (d) Transmission electron microscopy images (TEM), (b) and (e) high-resolution TEM images with electron diffraction at the same location, and (c) and (f) the normalized element-specific intensity of energy-dispersive X-ray spectroscopy line scans for NP batches with $R_w = 4, x = 0.39$ ((a)–(c)) and $R_w = 7, x = 0.37$ ((d)–(f)).

3.1.2.2 Chemical composition

From the Rietveld refinement of XRD spectra, the strontium concentration x of the sample could be extracted, as well, and is listed in Table 3.2. Due to the peak broadening induced by the small size of the NPs, the accuracy of x is limited to ±5%. The parameter x varies between $0.34 \leq x \leq 0.47$ for different batches, although the initial concentration in the microemulsion was $x = 0.25$ (see section 2.1.1.2). The reason for this discrepancy is discussed in section 4.1.2. Although the variation in x of the calcined samples is significant, one has to bear in mind that the phase diagram of $La_{1-x}Sr_xMnO_3$ is uniform both structurally and magnetically for this range of x (see Fig. 1.6): there are no x-dependent phase transitions at any temperature from $0 \leq T \leq 300$ K for $La_{1-x}Sr_xMnO_3$ with $0.34 \leq x \leq 0.47$ [26, 110, 111]. The magnetic phase diagram shows uniformly ferromagnetic behaviour at $T \leq T_C$ and paramagnetic for $T \geq T_C$, without any indication of charge order for $0.34 \leq x \leq 0.47$ [110, 127]. Therefore, the $La_{1-x}Sr_xMnO_3$ NP samples remain comparable despite the variation of x.

The Sr concentration given in the formula unit at the top of each column in Fig. 3.7 is obtained from EDX and has an uncertainty of ± 3.5% and ±2.7% for samples with $R_w = 4, x = 0.39$ (first column) and $R_w = 7, x = 0.37$ (second column), respectively. These values agree with the results obtained from XRD Rietveld refinement presented in Table 3.2. The bottom row of Fig. 3.7 shows the normalized intensity of Sr–, Mn–, O– and La–related EDX peaks as a function of position along NP agglomerates. For all three samples, the elemental composition is uniform within experimental accuracy for the small volume of sampled material. Hence, the observed variation of x is only between batches, but within each batch, x appears to be homogeneous for all NPs.

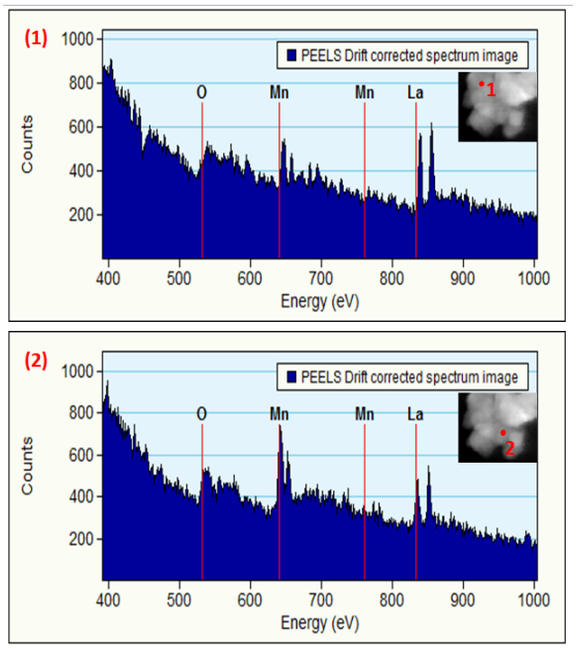

Figure 3.8: Electron energy loss spectra (EELS) for two different points (shown in the insets) in a $La_{1-x}Sr_xMnO_3$ sample with $\langle s \rangle = 52$ nm.

XAS spectra were collected in order to study the oxygen vacancy concentration and measure the effective hole concentration x_{eff} by analysing the Mn^{3+}/Mn^{4+} ratio. However, for $La_{1-x}Sr_xMnO_3$ it was impossible to fit the NEXAFS spectrum due to peak broadening and overlap between Mn^{3+} and Mn^{4+} L edges. Moreover, the double-exchange coupling can lead to an average oxidation state of Mn ions somewhere between Mn^{3+} and Mn^{4+}, resulting in a single absorption edge [212]. However, Co is much easier to reduce [218] hence the oxygen deficiency is expected to be lower in $La_{1-x}Sr_xMnO_{3-\delta}$ compared to $LaCoO_{3-\delta}$. As δ in $LaCoO_{3-\delta}$, $\delta_{LCO} = 0.04 \pm 0.01$, as obtained from NEXAFS, the parameter δ in $La_{1-x}Sr_xMnO_{3-\delta}$ is expected to be $\delta_{LSMO} \leq 0.04 \pm 0.01$, and probably not related to the size as is the case for $LaCoO_{3-\delta}$. Electron energy-loss spectra for two different points in a $La_{1-x}Sr_xMnO_3$ sample with $\langle s \rangle = 52$ nm are shown in Fig. 3.8. At an accuracy of ± 0.1, both spectra show stoichiometric $La_{1-x}Sr_xMnO_3$. Consistently, the EELS spectra taken at different points within one sample indicate that the oxygen stoichiometry is uniform across the samples within experimental accuracy, and is $\delta \leq 0.1$.

3.1.2.3 Nanoparticle size

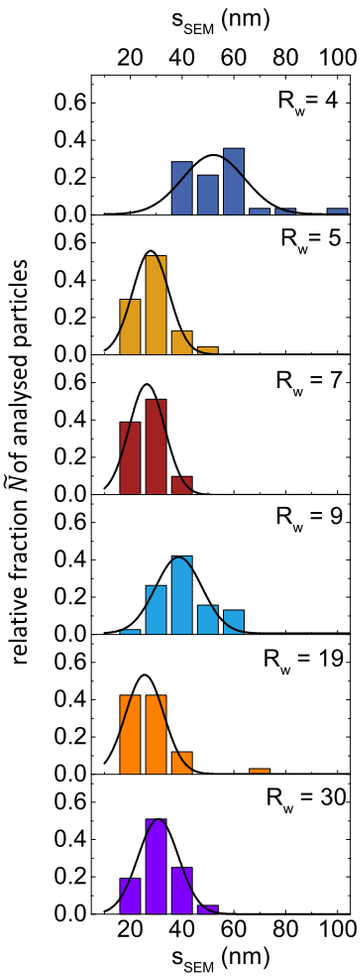

Figure 3.9: Fraction $\tilde{N}$ of NPs vs s_{SEM} as obtained from SEM for different $La_{1-x}Sr_xMnO_3$ sample batches synthesized with different water-to-surfactant ratio R_w. Histograms are obtained assuming spherical particle shape. The solid lines indicate Gaussian fits to $\tilde{N}$ vs s_{SEM}.

Fig. 3.7(a) shows the morphology of $La_{1-x}Sr_xMnO_3$ nanoparticles. Similarly to $LaCoO_3$ nanoparticles, there is some agglomeration, but no sintering and the crystallite size agrees well with the size from XRD, as shown in Table 3.2. The histograms in Fig. 3.9 show the number of NPs, normalized to the total number of $La_{1-x}Sr_xMnO_3$ nanoparticles, ($\tilde{N}$) as a function of particle size s_{SEM} for samples prepared with different R_w. Gaussian fits to $\tilde{N}$ vs s_{SEM} are also shown in Fig. 3.9 with the parameters listed in Table 3.2. The NP size obtained from XRD and SEM for $La_{1-x}Sr_xMnO_3$ are the same within experimental error, which confirms single-crystal particles as shown in Fig. 3.7(b) and (e). Here, SEM analysis over-estimates the nanoparticle size, because it cannot differentiate between crystallites and particles. It is possible, that a few non-single-crystal nanoparticles were measured, increasing the average particle size. But SEM also tends to slightly over-illuminate particles, if the interaction volume of electron beam and matter is larger than the NP size, part of the surroundings of the NPs will emit electrons, which will appear to be part of the NP under measurement in the image analysis. Both the assumption of spherical shape and the low number of analysed particles limit the accuracy of $\langle s \rangle_{\mathrm{SEM}}$. With $\sigma s/\langle s \rangle_{\mathrm{SEM}} \leq 0.25$ the size distribution is near the achievable lower limit for microemulsion synthesis of complicated oxides ($0.2 \leq \sigma s/\langle s \rangle \leq 0.5$ [219]) despite high temperature calcination [183]. The reason for lower $\sigma s/\langle s \rangle_{\mathrm{SEM}}$ for $La_{1-x}Sr_xMnO_3$ compared to $LaCoO_3$ is most likely the larger size of $La_{1-x}Sr_xMnO_3$ NP. The extremely small NP size for $LaCoO_3$ results in a large surface curvature and thus surface diffusion is accelerated, which increases the tendency to sinter and grow even at lower calcination temperatures, resulting in a broadening of the size distribution.

Table 3.2: Physical properties, i.e. average size $\langle s \rangle$ determined from SEM and XRD, with the Gaussian fit standard deviation σ_{SEM} and Δs_{XRD} from the Williamson-Hall fit, respectively, structural parameters a, $d_{\mathrm{Mn\text{-}O}}$, and $\theta_{\mathrm{Mn\text{-}O\text{-}Mn}}$ as obtained from Rietveld refinement, as well as Sr concentration x, and Curie temperature T_{C} for various water-to-surfactant molar ratios R_w used during synthesis.

R_w	$\langle s \rangle_{\mathrm{SEM}}$ (nm)	σ_{SEM} (nm)	$\langle s \rangle_{\mathrm{XRD}}$ (nm)	Δs_{XRD} (nm)	a (Å)	$d_{\mathrm{Mn\text{-}O}}$ (Å)	$\theta_{\mathrm{Mn\text{-}O\text{-}Mn}}$ (°)	S/V (nm^{-1})	x	T_{C} (K)
4	52	11.9	33	5	5.501	1.957	164.6	0.18	0.39	331
7	26	6.9	28	2	5.50	1.959	163.42	0.21	0.37	304
9	39	9.0	24	4	5.517	1.968	162.59	0.25	0.34	ND
19	26	7.4	20	3	5.497	1.962	162.61	0.30	0.47	269
25	34	5	23	3	5.491	1.958	162.67	0.25	0.30	ND
30	31	7.8	18	5	5.503	1.963	163.01	0.33	0.38	278

3.2 Structural changes

Following Rietveld refinement, the variation of structural parameters a, c, $d_{\text{M-O}}$, $\theta_{\text{M-O-M}}$, and V_{uc} is studied as a function of size, where M=(Co,Mn), and V_{uc} the unit-cell volume.

3.2.1 $LaCoO_3$

For $LaCoO_3$, the results of the Rietveld refinement are shown in Fig. 3.10. As mentioned in the introduction, the most important parameter to control the magnetic moment in $LaCoO_3$ is the Co-O bond length, $d_{\text{Co-O}}$, as it influences the crystal-field splitting. Fig. 3.10(c) shows clearly the linear increase of $d_{\text{Co-O}}$ with increasing S/V. Whereas the lattice parameter a is almost constant for all nanoparticle sizes, the c-axis parameter expands by up to 0.7% as the NP size decreases. The same increase is observed in the unit-cell volume V_{uc}. The relative expansion achieved in Ref. [76, 77] is of the same magnitude, but at only 38% of the S/V value. In conclusion the synthesis technique seems to have a large influence on the size-dependent expansion of the unit-cell volume. Fig. 3.10 (d) shows that $\theta_{\text{Co-O-Co}}$ decreases as the surface-to-volume ratio increases, indicating stronger octahedra tilt. This is similar to the results of Ref. [60], who have applied pressure to $LaCoO_3$ single crystals and measured a decrease of $d_{\text{Co-O}}$ and an increase of $\theta_{\text{Co-O-Co}}$, as pressure increases. In that sense, reducing the NP size produces an effective negative pressure.

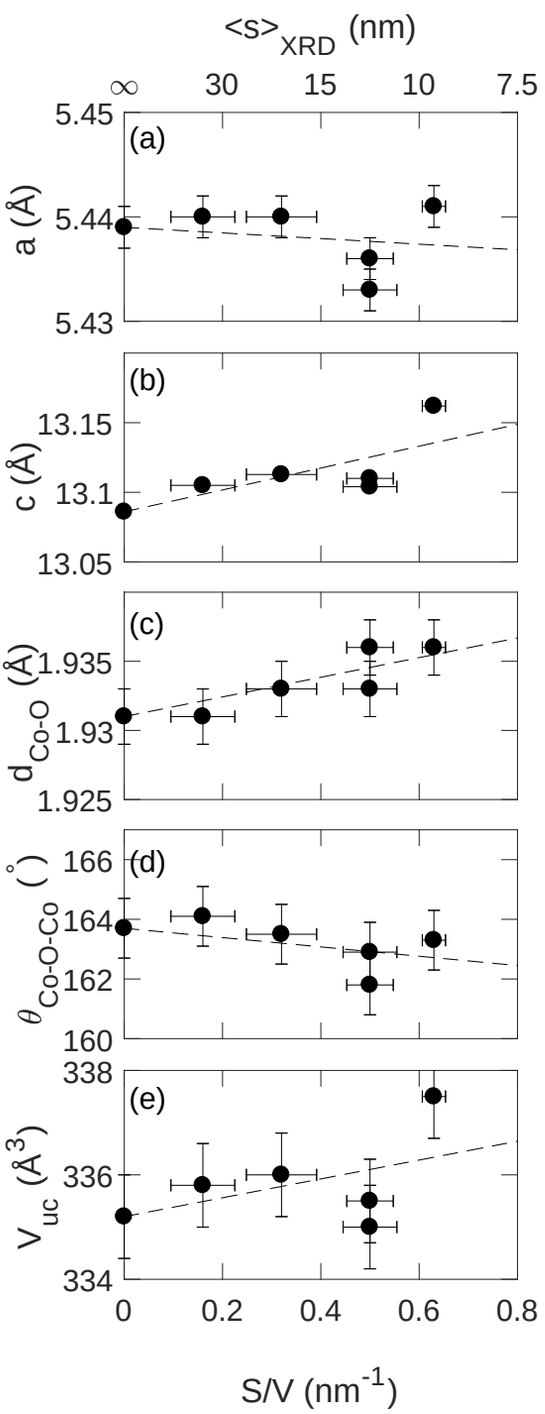

Figure 3.10: Lattice parameters (a) a, (b) c, (c) $d_{\text{Co-O}}$, (d) $\theta_{\text{Co-O-Co}}$, and (e) V_{uc} as functions of the surface-to-volume ratio S/V for $LaCoO_3$ nanoparticles. Linear fits through values for bulk $LaCoO_3$ are equally shown.

3.2.2 $La_{1-x}Sr_xMnO_3$

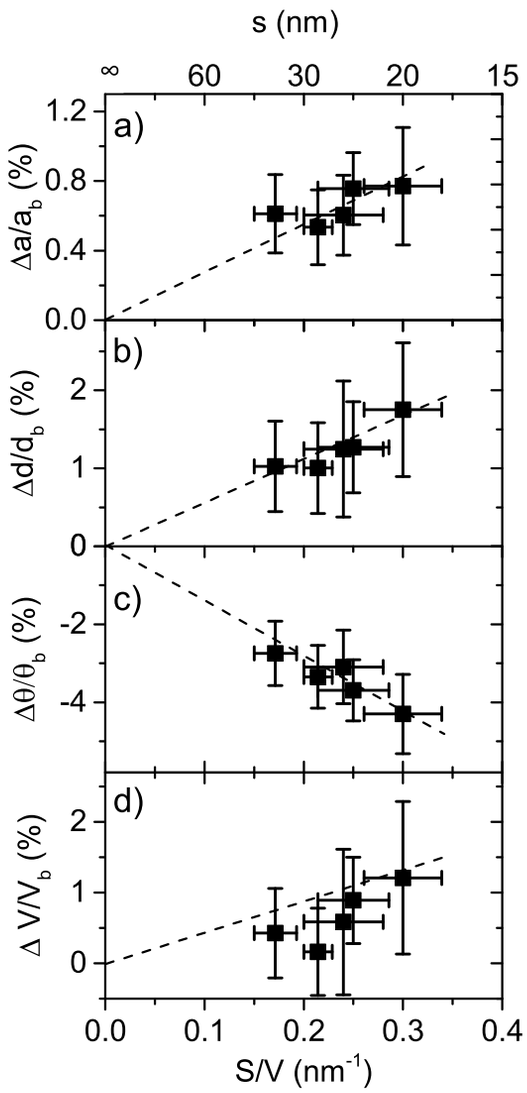

Figure 3.11: The relative changes $\Delta Y/Y_\mathrm{b}$ of the rhombohedral lattice parameter a, the Mn-O bond length $d_{\text{Mn-O}}$, the Mn-O-Mn bond angle $\theta_{\text{Mn-O-Mn}}$, and the unit-cell volume V_uc, compared to the bulk values having the same Sr concentration x as a function of particle size $\langle s\rangle_{\text{XRD}}$ (upper scale) and surface-to-volume ratio S/V (lower scale). Typical values for nanoparticles with $x = 0.37$ and $S/V = 0.21$ are: $a = 5.498$ Å, $d_{\text{Mn-O}} = 1.959$ Å and $\theta_{\text{Mn-O-Mn}} = 163°$. The dashed lines are linear extrapolations to the bulk, i.e. $\Delta i = 0$ and $S/V = 0$.

As mentioned above, the Sr concentration x is not identical for all $La_{1-x}Sr_xMnO_3$ nanoparticle batches, and the structural properties a, $d_{\text{Mn-O}}$, and $\theta_{\text{Mn-O-Mn}}$ for sample batches with different R_w vary significantly. In order to identify the impact of particle size on the structural properties, one has to extricate the influence of the Sr concentration x on the crystal structure. With increasing Sr concentration, a decrease of the parameters a [110, 220–222] and Mn-O bond length $d_{\text{Mn-O}}$ [223] have been reported for bulk $La_{1-x}Sr_xMnO_3$, whereas $\theta_{\text{Mn-O-Mn}}$ increases with increasing x towards 180° [220, 224, 225]. In order to disentangle the effects of Sr concentration and particle size on structural properties, the lattice-parameter differences between NPs (np) and bulk (b) having the same Sr concentration x are normalized to the bulk value, i.e., ($\frac{\Delta a}{a_\mathrm{b}} = [a(x,\mathrm{np}) - a(x,\mathrm{b})]/a(x,\mathrm{b})$, $\frac{\Delta d}{d_\mathrm{b}} = [d(x,\mathrm{np}) - d(x,\mathrm{b})]/d(x,\mathrm{b})$, $\frac{\Delta\theta}{\theta_\mathrm{b}} = [\theta(x,\mathrm{np}) - \theta(x,\mathrm{b})]/\theta(x,\mathrm{b})$), assuming that the variation of the lattice parameters with $\langle s\rangle$ is the same for $0.3 \le x \le 0.47$. For simplicity, the variation of structural properties with respect to bulk is labelled $\Delta Y_i/Y_{i,\mathbf{b}}$, with $i = a, d_{\text{Mn-O}}, \theta_{\text{Mn-O-Mn}}, V_\mathrm{uc}$. In Fig. 3.11 the relative changes $\Delta Y_i/Y_{i,\mathrm{b}}$ were plotted against the surface-to-volume ratio S/V. A linear extrapolation of the relative change $\Delta Y_i/Y_{i,\mathrm{b}}$ to $S/V = 0$, i.e., for bulk-like infinitely large particles, is also indicated in Fig. 3.11. The data shown in Fig. 3.11 indicate the dominant role of the surface for the lattice changes at the nanoscale, irrespective of x. As for $LaCoO_3$, the primary difference is the relative increase of $d_{\text{Mn-O}}$ by up to 1.7% and the decrease of $\theta_{\text{Mn-O-Mn}}$ by 5%, as S/V increases from 0 to 0.3 nm^{-1}. Plotting the relative changes $\Delta Y_i/Y_{i,\mathrm{b}}$ versus S/V as deduced from TEM or SEM measurements results in qualitatively the same behaviour.

3.3 Magnetic properties

3.3.1 $LaCoO_3$

3.3.1.1 Size-dependent spin state

Fig. 3.12 contrasts NEXAFS spectra of nanoparticles with $\langle s \rangle$ = 9.5 nm and $\langle s \rangle$ = 37.7 nm ((a) and (b), respectively), measured at 60 K. The multiplet fits are also shown. The pre-peak at 777.4 eV, marked with an asterix, is the signature for octahedrally coordinated Co^{2+} ions, a result of oxygen deficiency, which is tabulated in Table 3.3.

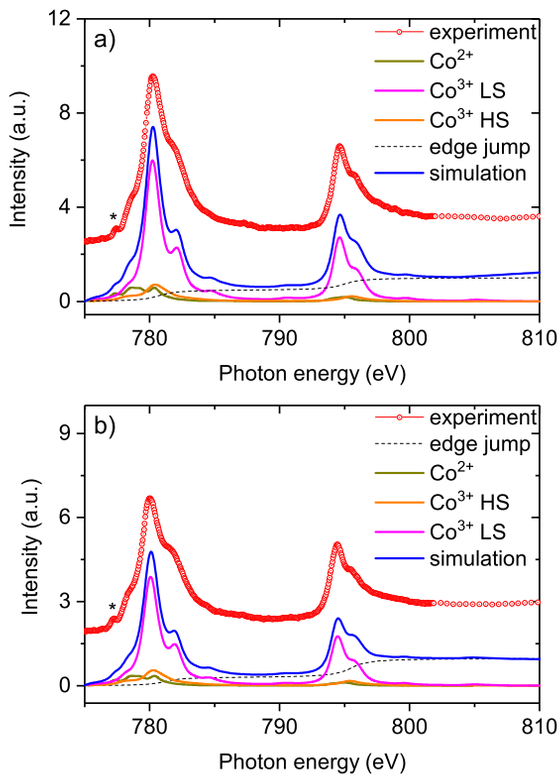

Figure 3.12: Near-edge X-ray absorption fine structure spectra (red), the contributions of Co^{2+} in octahedral coordination (olive), Co^{3+} in the high-spin (orange) and low-spin (pink) states, and the simulated spectrum (blue) at T = 60 K for $LaCoO_3$ nanoparticle samples with a) $\langle s \rangle$ = 9.5 nm and b) $\langle s \rangle$ = 37 nm.

Comparing spectra (a) and (c), the shoulder at 778.6 eV is clearly visible for nanoparticle samples (a) and (b). The shoulder is a signature of Co^{3+} HS [47]. For all samples, a second shoulder at 782 eV is observed, which is the second part of the HS signal, superposed with the LS signal centred at 780 eV. Additionally, the second part of the spectrum at about 795 eV can be used to separate the HS and LS contributions. The HS peak is at 796.3 eV, whereas the LS one is at 794.7 eV, with a shoulder at about 796 eV. Fitting the theoretical spectra to the experimental data yielded the HS and LS concentrations shown inside the

plots in Fig. 3.12 and documented in Table 3.3. The oxygen deficiency parameter δ is obtained directly from the concentration of Co^{2+}, as described in Section 3.1.1.2 on page 37.

Table 3.3: The concentrations of Co^{3+} high-spin (HS) and Co^{3+} low-spin (LS) as well as Co^{2+} and the corresponding parameter δ in $LaCoO_{3-\delta}$ for two $LaCoO_3$ NP samples, with $\langle s \rangle$ = 9.5 nm and $\langle s \rangle$ = 37 nm, respectively.

	HS (%)	LS (%)	Co^{2+}	δ
9.5±2 nm				
300 K	24±2	68±2	8±2	0.040±0.01
60 K	18±2	74±2	8±2	0.040±0.01
37±7 nm				
300 K	20±2	71±2	9±2	0.045±0.01
60 K	13±2	78±2	9±2	0.045±0.01

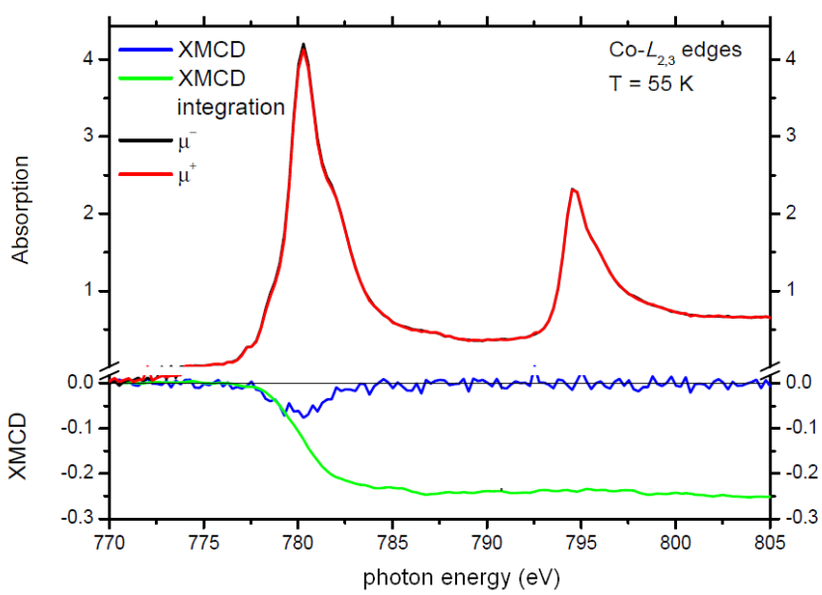

Figure 3.13: Co-$L_{2/3}$ absorption edges measured with left and right circularly polarized light (black and red curves, respectively). Their difference is the X-ray magnetic circular dichroism (XMCD, blue line), with the XMCD integration (green line). The resultant orbital and spin magnetic moments calculated from the sum rules are displayed, as well.

On one of the samples it was possible to conduct XMCD measurements at applied field $\mu_0 H$ = 4 T, which is shown in Fig. 3.13. The analysis according to Equation 2.30 yields an orbital moment of m_{orb} = 0.038 μ_B/Co and a spin moment of m_{spin} = 0.056 μ_B/Co. The

ratio of the contributions is therefore $m_{orb}/m_{spin} = 0.68$, which is somewhat higher than measured for bulk: $m_{orb}/m_{spin} = 0.5$ [51]. This increase in orbital contribution in XMCD has been observed for nanoparticles with respect to single crystals. Ref. [226], for example, shows that the orbital contribution depends on the nature of adsorbed molecules on the surface of $Fe_{1-x}O_3$ nanoparticles. Similarly, an increased orbital moment was found for CoO and $(Mn_xFe_{1-x})_3O_4$ nanoparticles due to decreased coordination and consequently stronger spin-orbit coupling at the surface [227, 228]. Disorder can also increase the orbital magnetic moment [229]. The total moment at $\mu_0 H = 4$ T is $m_{total} = m_{orb} + m_{spin} = 0.094\ \mu_B$/Co, which is slightly larger than the results from SQUID measurements at $\mu_0 H = 1$ T and $T = 55$ K, $m_{1\,T,55\,K} = 0.08\ \mu_B/Co^{3+}$HS, at [HS]≈18% (Table 3.3). The contribution of Co^{2+} is negligible, as its intensity is lower than the noise level. XMCD measurements confirm that the orbital moment is not quenched, hence the J value for the fits of a Brillouin function to the magnetization data according to Equation 2.32 is taken as $\tilde{J} = 1$ and $g = 3.2$, as published in Refs. [51] and [65].

3.3.1.2 Magnetic properties

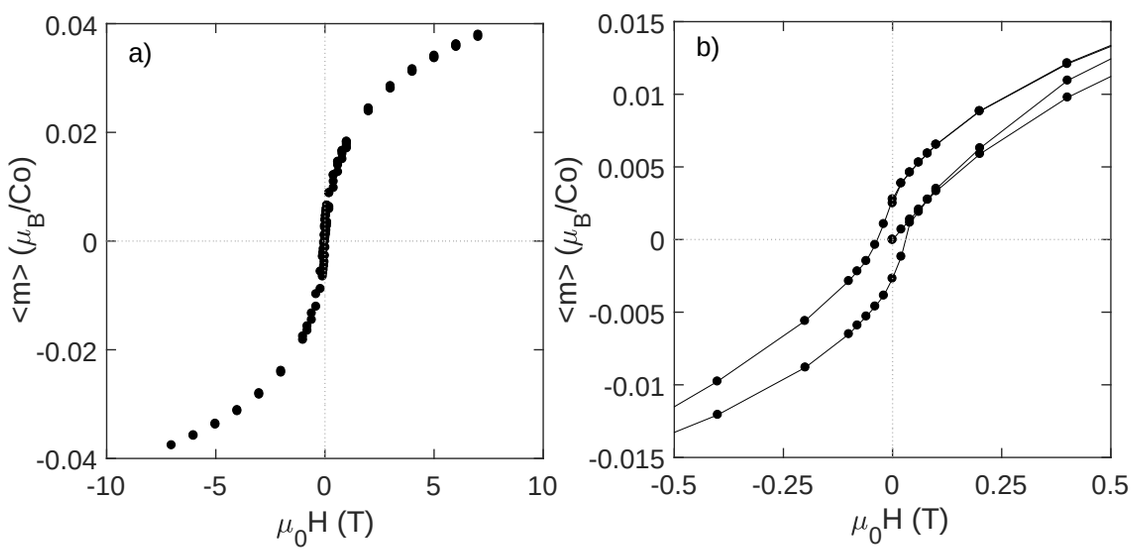

Figure 3.14: (a) Hysteresis curve measured at $T = 5$ K up to $\mu_0 H = 7$ T for a $LaCoO_3$ sample with $\langle s \rangle = 9.5$ nm, and (b) the magnified curve from (a) for $-0.5 \leq \mu_0 H \leq 0.5$ T.

Fig. 3.14 (a) shows the hysteresis curve at $T = 5$ K up to $\mu_0 H = 7$ T for a sample with $\langle s \rangle = 9.5$ nm. There is a slight anisotropy between magnetization and demagnetization with a "coercive field" of ≈ 0.04 T (Fig. 3.14 (b)), which is much lower than the coercive field observed in ferromagnetic $LaCoO_3$ thin films, where $H_C \approx 0.5$ T [1]. Nevertheless, the behaviour appears to be paramagnetic, and the anisotropy is attributed to particle-particle interactions.

At $T = 5$ K, bulk $LaCoO_3$ is expected to have all Co^{3+} ions in the LS state. Since the Co^{3+} LS state is non-magnetic, the observed magnetic moment shown in Fig. 3.14 is most likely due to Co^{3+} HS. The lowest possible temperature to measure the Co^{3+} HS concentration [HS] with NEXAFS is 60 K. At this temperature, NEXAFS yielded [HS]=18% for the $LaCoO_3$ sample with $\langle s \rangle = 9.5$ nm. With a $\mu_{\text{eff}} = 3.16$, this would result in an expected average magnetic moment of $\langle m \rangle = 0.18 \times 3.16 = 0.57 \mu_B$/Co if all the spins are aligned. The experimental value is only $\langle m \rangle$ (60 K, 7 T) $\approx 0.22\ \mu_B$/Co, which is about 30% of the expected moment at 60 K, because 7 T is not high enough to align all the spins at 60 K. Ref. [47] found half of the spins aligned in a thin film with 36% Co^{3+} HS at $T = 20$ K. The lower amount of aligned spins in NP could be due to the higher temperature or disordered surface spins [7, 10, 18, 19].

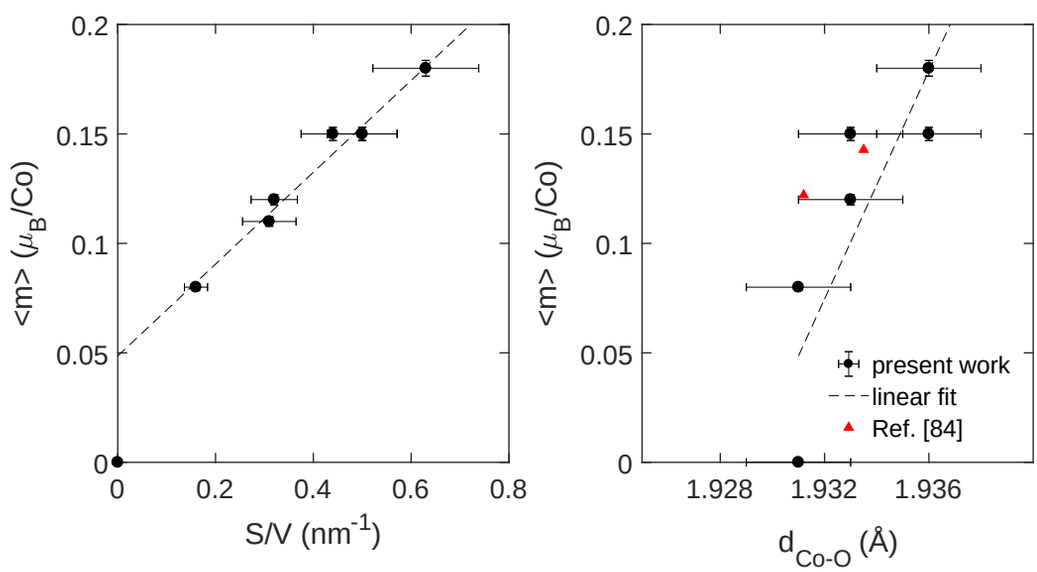

Figure 3.15: The average magnetic moment $\langle m \rangle$/Co measured at $T = 5$ K and $\mu_0 H = 7$ T as function of (a) the surface-to-volume ratio S/V and (b) the Co-O distance $d_{\text{Co-O}}$. Dotted lines are linear fits to the experimental data (the fit in (b) takes into account the offset due to Co^{2+} derived from the linear fit in (a)). For comparison, data published in Ref. [76] is shown in (b) (red triangles).

To compare the magnetic moment of NPs with different sizes (different S/V), the average magnetic moment per Co ion at $\mu_0 H = 7$ T and $T = 5$ K ($\langle m \rangle$ (7 T, 5 K)/Co) is analysed as a function of the surface-to-volume ratio S/V in Fig. 3.15(a). At 5 K, extrapolating the linear fit to $\langle m \rangle$ vs. S/V in Fig. 3.14(a) to bulk with $S/V = 0$, a finite magnetic moment of $\langle m \rangle_b = 0.05\ \mu_B$/Co is obtained. For magnetization measurements performed at $5 \leq T \leq 40$ K, the trend of $\langle m \rangle_{7T}$ against S/V stays qualitatively the same, but the slope decreases. The intercepts, however, stay more or less constant at $\langle m \rangle$ ($S/V = 0$) $\approx 0.05 \pm 0.02\ \mu_B$/Co. This constant additional magnetic moment is therefore ascribed to Co^{2+} ions with a spin of $S = 3/2$, as their concentration does not change with temperature or S/V. With $\mu_{\text{eff}} \approx 3.9\ \mu_B$/Co for Co^{2+} HS, and a concentration of Co^{2+} of 8% according to the NEXAFS results at 60 K, the magnetic moment of 0.05 μ_B/Co at $T = 5$ K

can be achieved if 16% of all Co^{2+} spins are aligned with the external magnetic field. It is reasonable to assume that most of the Co^{2+} ions are located near the surface due to their association with oxygen vacancies, hence most spins are likely disordered.

As shown in Fig. 3.10(c), the decrease of the NP size seems to induce an elongation of the Co-O bond length $d_{\text{Co-O}}$, which could stabilize the magnetic Co^{3+} HS state by decreasing the crystal field splitting. Therefore, Fig. 3.15(b) shows the average magnetic moment per Co ion at $\mu_0 H = 7$ T and $T = 5$ K ($\langle m \rangle$ (7 T, 5 K)/Co) as a function of the Co-O distance $d_{\text{Co-O}}$. The apparent correlation between $\langle m \rangle$/Co and $d_{\text{Co-O}}$ indicates that the magnetic signal emerges due to a higher population of Co^{3+} HS with increasing $d_{\text{Co-O}}$. The linear fit shown in Fig. 3.15(b) takes into account the constant addition of $m_{Co^{2+}} = 0.05$, i.e. the magnetization is not zero for the bulk value of $d_{\text{Co-O}}$. For comparison, the data published in Ref. [76] are added: within experimental accuracy, the $\langle m \rangle$ (7 T, 5 K)/Co vs $d_{\text{Co-O}}$ data agree for NP samples synthesized by microemulsion (present work) and sol-gel (Ref. [76]).

Comparing data from the present study to literature values from Table 1.2, a 20% smaller magnetization is achieved for NP samples in this study compared to literature values at the same nanoparticle size, but the unit-cell volume expansion is also 50% less in $LaCoO_3$ nanoparticles synthesized by microemulsion. This is probably due to higher crystal quality in the present study, very low oxygen deficiency and absence of impurity phases in the present samples. Co^{2+} was not considered quantitatively in Refs. [76, 77, 96–98]. Figs. 3.10 (a) and (b) clearly show linear relationships between $\langle m \rangle$ and S/V and between $\langle m \rangle$ and $d_{\text{Co-O}}$. The slopes are listed in Table 3.4 for data from the present study and from Ref. [76, 77]. Values of the magnetization and selected lattice parameters in Refs. [95–97] are comparable to the ones in Ref. [76, 77], but $d_{\text{Co-O}}$ is not reported.

Table 3.4: Correlation between surface-to-volume ratio S/V, Co-O bond length $d_{\text{Co-O}}$, and average magnetic moment $\langle m \rangle$ for $LaCoO_3$ NP synthesized by microemulsion and values from Ref. [76, 77].

	this study	Ref. [76, 77]
$\mathrm{d}d_{\text{Co-O}}/\mathrm{d}(S/V)$ [Å nm]	0.008 ±0.007	0.034 ±0.023
$\mathrm{d}\langle m \rangle/\mathrm{d}(S/V)$ [μ_B/Co nm]	0.27 ±0.04	0.6 ±0.2
$\mathrm{d}\langle m \rangle$ (5 K)/$\mathrm{d}d_{\text{Co-O}}$(300 K) [$\mu_B$/Co Å^{-1}]	15 ($\mu_0 H = 7$ T) ±7	18 ($\mu_0 H = 5$ T) ±8

The quantitative relationship between $d_{\text{Co-O}}$ and $\langle m \rangle$ is the same within experimental error for NPs synthesized by microemulsion in the present study and for NPs produced by sol-gel and varying calcination temperatures in Ref. [76, 77]. This is shown in Fig. 3.15(b), where the data points from Ref. [76, 77] agree with the data points from the present study within experimental accuracy. This shows that $d_{\text{Co-O}}$ is the sole parameter controlling the magnetic moments in $LaCoO_3$ NPs, and to some extent in epitaxial thin films [1, 69]. The relationship between S/V and $d_{\text{Co-O}}$, and therefore also the relationship between S/V and $\langle m \rangle$, on the other hand, lacks consistency. Possible reasons for this will be discussed further in section 4.2.

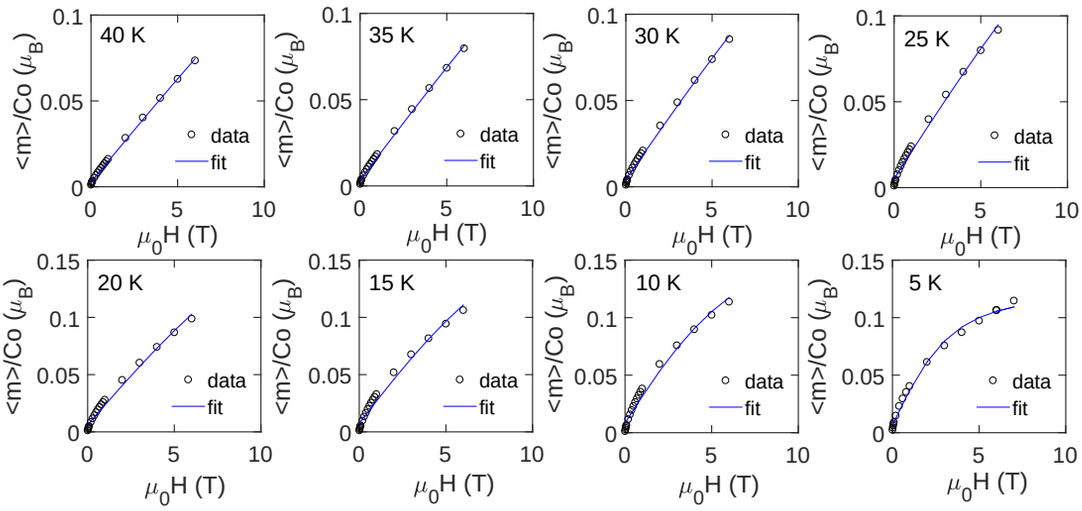

Figure 3.16: Brillouin fits at different temperatures for an $LaCoO_3$ NP sample with $\langle s \rangle$ = 19.5 nm. The diameter of the data points correspond to an experimental error of $\pm 0.004 \mu_B$.

The virgin magnetization curves measured up to $\mu_0 H = 7$ T at $5 \leq T \leq 40$ K can be described using Equation 2.32. The results are shown exemplarily for a sample with $\langle s \rangle = 19.5$ nm in Fig. 3.16. The fitted curves agree well with experimental data for $40 \geq T \geq 5$ K. It is noted here that the fits look equally good if J is chosen as $J = 2$ and $g = 2$, as would be the case for totally quenched orbital moment. However, the XMCD measurements show a significant contribution of m_{orb} (Fig. 3.13), therefore $\tilde{J} = 1$ and $g = 3.2$ is used.

The fitting parameters $N_{Co^{3+}}$ and B_i were analysed as functions of temperature and S/V, as shown in Fig. 3.17-3.18. Fig. 3.17 (a) shows the evolution of the Co^{3+} HS concentration ([HS]) as a function of temperature for samples with different S/V. There is a monotonic increase of the Co^{3+} HS population with increasing temperature for all samples, just as expected. In bulk $LaCoO_3$ there is also an increase of the HS population as the unit cell increases due to thermal expansion and the thermal excitation is large enough to overcome the energy barrier between LS and HS states [48]. The HS concentration is largest for the smallest NPs ($\langle s \rangle = 9.5$ nm) with the largest $S/V = 0.63$. The value of $N_{Co^{3+}}$ varies linearly with S/V for all temperatures (see Fig. 3.17 (b)) and extrapolation to $S/V = 0$ yields the $N_{Co^{3+}}$ values for bulk $LaCoO_3$ at different temperatures. These extrapolated values are also plotted in Fig. 3.17 (a), and are clearly lower than any of the nanoparticle curves. However, the behaviour of the sample with $\langle s \rangle = 37$ nm ($S/V = 0.16$) is close to that of the bulk.

Despite considerable efforts [59, 60, 230], simulations of the concentration of Co^{3+} HS ([HS]) as a function of temperature in $LaCoO_3$ fail to represent the experimental data at low temperatures ($T \leq 50$ K). The extrapolated values from Fig. 3.17(b) show 2% HS concentration down to low temperatures, although simulations find 0% [59, 230]. It is possible that the higher [HS] values for bulk $LaCoO_3$ compared to theory (Refs. [59, 230]) is a result of Co^{2+}, the concentration of which is (8 ± 2)% measured at $T = 60$ K (see

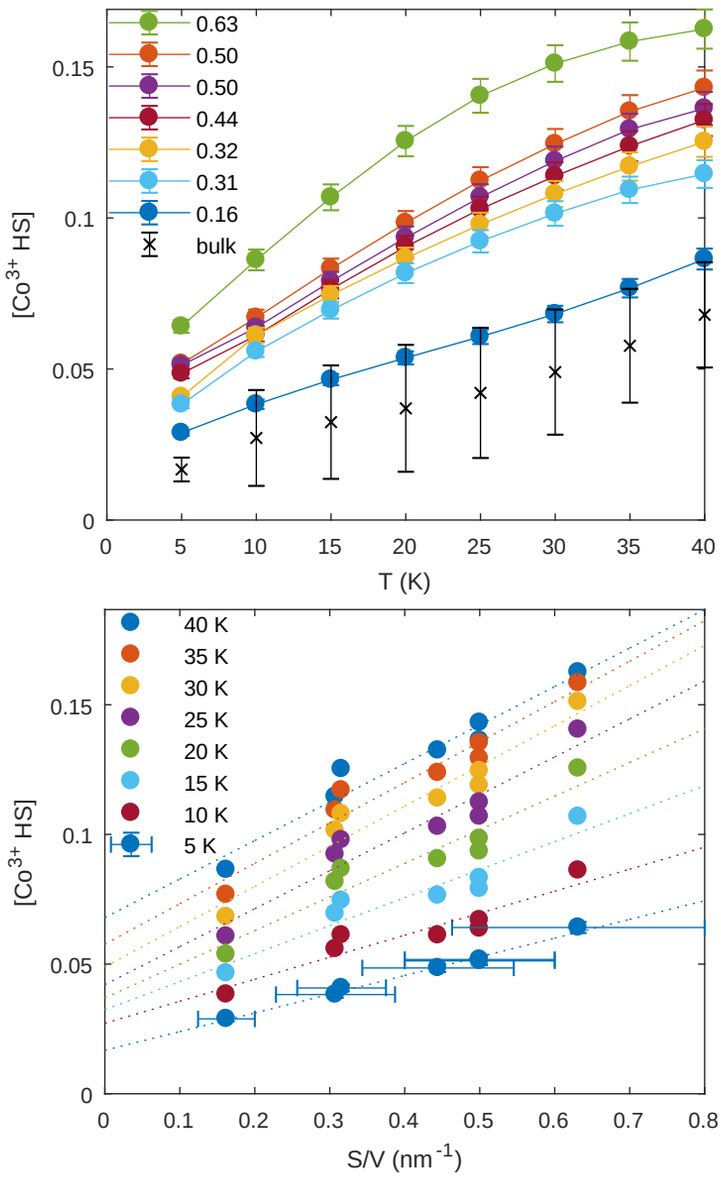

Figure 3.17: The concentration of Co^{3+} ions in the HS state ([Co^{3+} HS]) obtained from Brillouin fits (a) as a function of temperature for different S/V (solid lines are guides to the eye) and (b) as a function of S/V at different temperatures with linear extrapolations to bulk ($S/V = 0$). For clarity, the error bars are only shown on the curve measured at $T = 5$ K, as the uncertainty, mainly arising from the error in the size determination, is identical for measurements at all temperatures used.

Table 3.3). As shown in Fig. 3.15(a), this temperature-independent Co^{2+} concentration results in a constant addition of $m_{Co^{2+}} = 0.05$ for all samples. This moment can be achieved by [Co^{3+} HS] $\approx$ 2% assuming an effective moment of $\mu_{eff} = 3.15$ nm in accordance with

Table 1.1. Low-temperature measurements of [HS] are rare and subject to significant error. Ref. [51] measured about [HS]= (5 ± 5)% at 60 K, which is similar to the value extrapolated for bulk $LaCoO_3$ in Fig. 3.17: [HS]= (6.3 ± 1.5)% at 40 K.

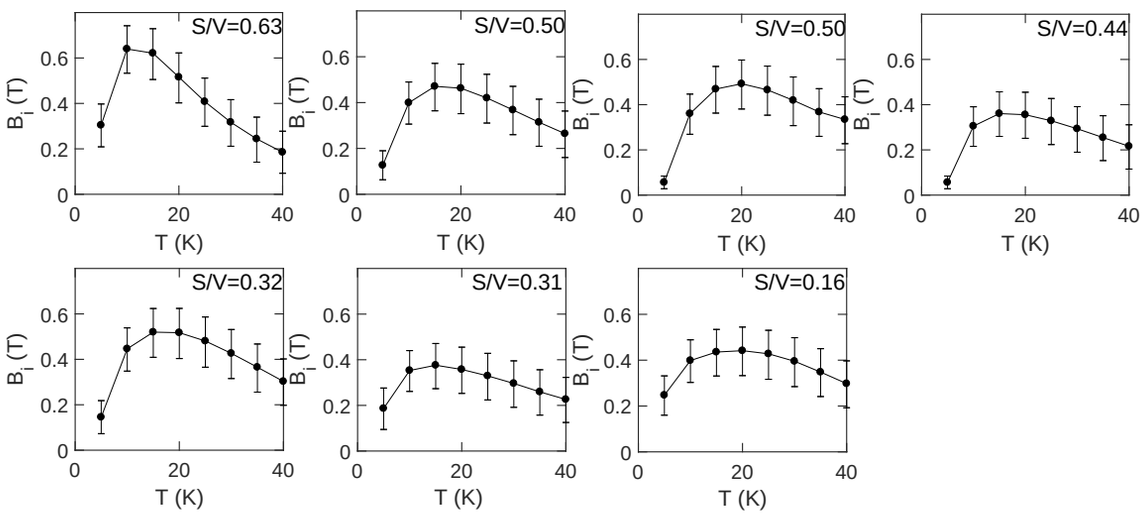

Figure 3.18: The internal field B_i as a function of temperature for nanoparticles with different surface-to-volume ratios (S/V). The solid lines are guides to the eye.

Fig. 3.18 shows the temperature dependence of the internal field B_i, as obtained from the Brillouin fit, for NP samples with different S/V. Despite the relatively large error bars, B_i is clearly not constant for temperatures ranging from $5 \leq T \leq 40$ K. Within experimental accuracy, there is no correlation of B_i with NP size. The value of B_i is between 0.1 and 0.6 T, which is too low to indicate ferromagnetism, in which case the internal field is of the order of magnitude of at least tens of T. Additionally, in ferromagnets the internal field would be expected to be constant with temperature. B_i vs temperature T shows a peak at $T = T(B_{\mathrm{i,max}})$.

Since the internal field is so small, it can be overcome by the externally applied field, which corresponds to the irreversibility field B_irr at a certain temperature $T(B_\mathrm{irr})$. At this temperature the zero-field cooled (ZFC) and field-cooled (FC) curves separate. Fig. 3.19 shows ZFC/FC curves for a sample with $\langle s \rangle = 19.5$ nm measured at different applied fields 0.06 T$\leq B_\mathrm{app} \leq$ 1 T. As shown in Fig. 3.18, the internal field varies between $0.1 \leq B_\mathrm{i} \leq 0.6$ T depending on the temperature. The irreversibility point roughly corresponds to the temperature, at which $B_\mathrm{i} = B_\mathrm{app}$. The correlation between B_i and B_app is discussed in more detail in section 4.3.1.

The field-cooled (FC) curves show that the magnetic moment starts to rise below about 80 K, which is close to the Curie temperature $T_\mathrm{C} = 85$ K [231], but there is no sign of a magnetic transition (change in curvature). The temperature, at which the magnetic moment starts to increase, labelled T^*, does not depend on NP size (S/V) or applied field $\mu_0 H$. In bulk $LaCoO_3$, the B/m signature is opposite to the one observed in the inset of Fig. 3.20: in bulk, the susceptibility decreases as the temperature decreases due to a deple-

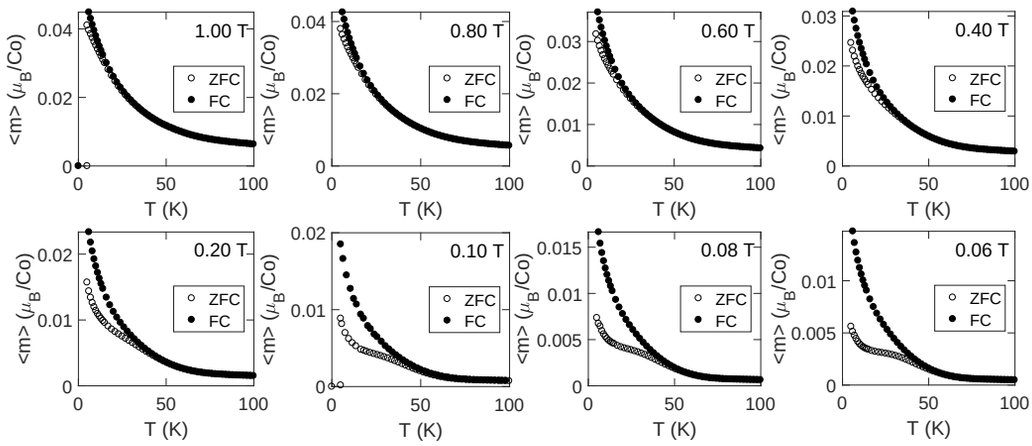

Figure 3.19: Field-cooled (FC, filled circles) and zero-field cooled (ZFC, empty circles) curves at different applied fields for a $LaCoO_3$ NP sample with $\langle s \rangle = 19.5$ nm.

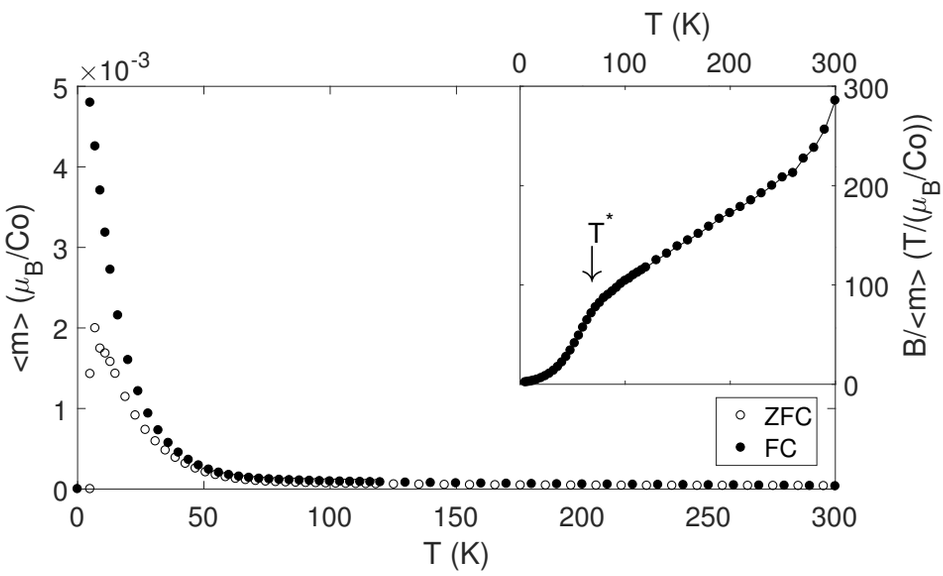

Figure 3.20: The field-cooled (FC) and zero-field cooled (ZFC) curves measured at 100 mT on a sample with $\langle s \rangle = 9.5\ nm$, and the inverse of magnetic moment divided by the applied field, $B/\langle m \rangle$ as a function of temperature T (inset).

tion of the Co^{3+} HS population. In nanoparticles, however, m/B increases significantly at $T \leq 80$ K, although the Co^{3+} HS concentration is decreasing with decreasing temperature analogue to bulk $LaCoO_3$ as shown in Fig. 3.17(a). The drop in susceptibility at $T \leq T^*$ could indicate stronger correlations of Co^{3+} HS spins below the Curie temperature. Note that due to the temperature-dependent variation in Co^{3+} HS concentration the B/m curve cannot be extrapolated to $B/m = 0$ in order to find the transition temperature.

3.3.2 $La_{1-x}Sr_xMnO_3$

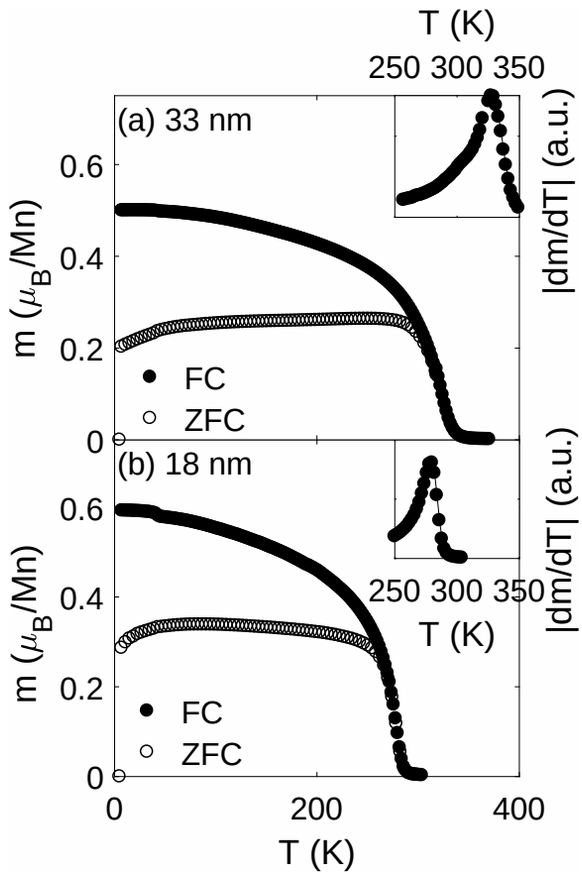

Figure 3.21: Field-cooled (FC) and zero-field-cooled (ZFC) magnetic moment *m(T)* at magnetic field strength $\mu_0 H = 10$ mT for a sample with (a) $\langle s \rangle_{\mathrm{XRD}} = 33$ nm and (b) $\langle s \rangle_{\mathrm{XRD}} = 18$ nm. The insets show where the temperature of the maximum is used to identify T_C ($|\mathrm{d}m/\mathrm{d}T|$). The Sr concentration of the two sample batches is $x = 0.39$ and $x = 0.38$, respectively.

Field-cooled and zero-field cooled measurements of the magnetization as a function of temperature were carried out at a magnetic field strength $\mu_0 H = 10$ mT. Fig. 3.21 displays exemplarily the magnetic moment $m(T)$ for NPs with mean particle sizes $\langle s \rangle_{\mathrm{XRD}} = 33$ nm and 18 nm. The Sr concentration of these two sample batches was $x = 0.39$ and $x = 0.38$, respectively, thus eliminating a major effect of the Sr concentration. Below about 350 K and 300 K, respectively, $m(T)$ starts to increase strongly with decreasing T and reaches saturation, indicating ferromagnetic order of the sample. The Curie temperatures T_C of the samples were deduced from the minimum of $\mathrm{d}m/\mathrm{d}T$ (see insets of Fig. 3.21) and are listed in Table 3.2. Obviously, comparing samples with such different average sizes but similar Sr concentration x shows that irrespective of Sr concentration x, T_C seems to be reduced significantly with decreasing particle size.

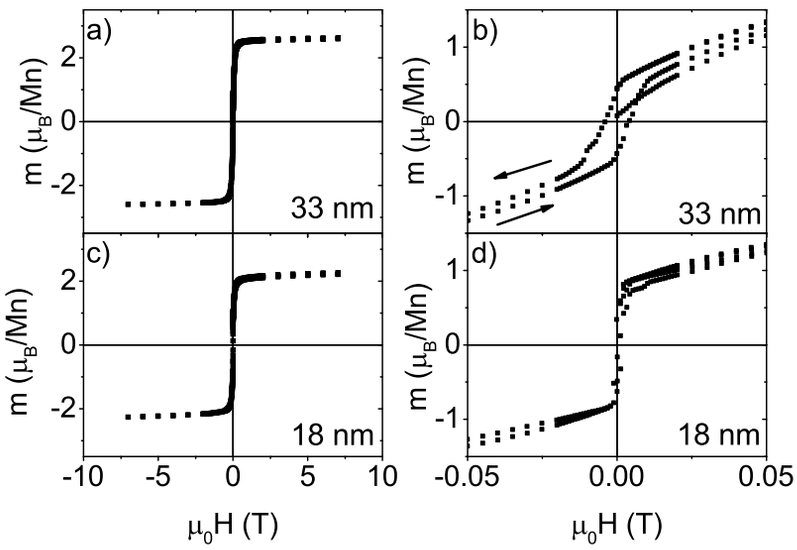

Figure 3.22: Hysteresis curves at $T = 5$ K for (a) $\langle s \rangle_{\mathrm{XRD}} = 33$ nm and (c) $\langle s \rangle_{\mathrm{XRD}} = 18$ nm. The magnified hysteresis loops at $|\mu_0 H| \leq 50$ mT show (b) multi-domain behaviour for $\langle s \rangle_{\mathrm{XRD}} = 33$ nm, and (d) single-domain structure for $\langle s \rangle_{\mathrm{XRD}} = 18$ nm. The Sr concentration of the two sample batches is $x = 0.38$ and $x = 0.39$, respectively.

Fig. 3.22 shows hysteresis curves for the same two samples with $\langle s \rangle_{XRD} = 33$ nm and 18 nm, and Sr concentration $x = 0.39$ and $x = 0.38$. Fig. 3.22(a) and (c) show the complete field sweeps at $T = 5$ K up to $\mu_0 H = 7$ T. The saturated magnetic moment amounts to about 2.5 μ_B/Mn, well below the theoretical value of about 3.5 μ_B/Mn, expected for a Mn^{3+}/Mn^{4+} mixture with $x = 0.5$. This seems to be typical of NPs and has been observed before for $La_{1-x}Sr_xMnO_3$ [19, 119]. The reduced magnetic moment is often related to the presence of a magnetically dead layer at the surface, where strong lattice distortions, reduced coordination and structural disorder lead to a highly frustrated system and prevent Mn ions from contributing to the total magnetic moment even at high applied fields [7, 10, 19, 112]. Fig. 3.22(b) and (d) display the magnified hysteresis loops for $|\mu_0 H| \leq 50$ mT. Small coercivity is observed for particle sizes $\langle s \rangle \geq 26$ nm, indicating a multi-domain magnetic structure, whereas the sample with smaller NP size ($\langle s \rangle = 18$ nm) appears to be single-domain. None of the samples show superparamagnetic Langevin behaviour, as they are larger than the critical size of $s = 16$ nm, published in Refs. [162, 174].

4 Discussion

The discussion chapter will focus on three individual aspects: firstly, the effectiveness of microemulsion synthesis will be briefly evaluated, followed by a discussion on the size-induced structural changes observed for both $LaCoO_3$ and $La_{1-x}Sr_xMnO_3$ NPs. Finally, the deviation of magnetic behaviour from bulk samples will be discussed in terms of indirect and direct dependence on NP size.

4.1 Microemulsion synthesis: size control and chemical composition

Precipitation in microemulsions was chosen as the synthesis technique in order to achieve uniform batches of $LaCoO_3$ and $La_{1-x}Sr_xMnO_3$ nanoparticles, with NP size being the only difference between batches, and stoichiometry and crystal quality being the same for all batches. It will be shortly discussed below whether this goal was reached.

4.1.1 Size control

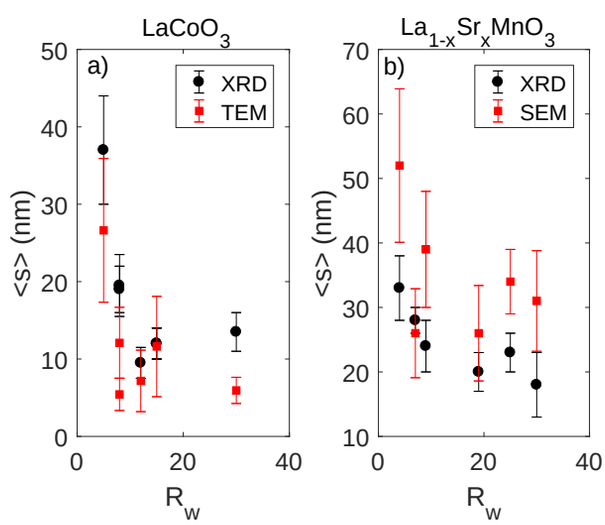

Figure 4.1: (a) $LaCoO_3$ nanoparticles and (b) $La_{1-x}Sr_xMnO_3$ nanoparticles mean size $\langle s \rangle_{XRD}$ as obtained from Williamson-Hall Analysis of XRD spectra (black) and $\langle s \rangle_{TEM}$ and $\langle s \rangle_{SEM}$ (red), for (a) and (b), respectively, as a function of the water-to-surfactant-ratio R_w.

Fig. 4.1 (a) and (b) depict the R_w-dependent NP sizes obtained from the Williamson-Hall analysis of XRD patterns and NP sizes obtained from image analysis on electron micrographs for $LaCoO_3$ and $La_{1-x}Sr_xMnO_3$ NPs, respectively. Fig. 4.1 (a) and (b) both reveal two distinct regimes: for $R_w \leq 12$ (Regime 1), the resultant NP size decreases with increasing R_w, whereas for $R_w \geq 12$ (Regime 2), no trend is observed. As the nanoparticle size is controlled by the water-to-surfactant ratio, i.e. the size of the water droplets, the chemical composition of desired products is not expected to significantly influence the nanoparticle size: according to Ref. [185] $R_w \leq 15$ should yield a stable microemulsion for $0.12M$ solutions of barium and titanium nitrate salts as the aqueous phase, but the higher precursor-salt concentration (0.8 mol/l) in the present work seems to decrease the stability region [184]. In the turbid phase no nanoreactors are formed and hence control over particle size is lost.

Regime 1 shows that the size range is larger for $LaCoO_3$ NP, because they can be calcined at lower temperatures and sintering and growth of NP is avoided. The range of nanoparticle sizes could potentially be expanded by choosing different calcination temperatures, as was done in Refs. [76, 77, 95–97], but only at the cost of changing the crystal quality as a function of calcination temperature. A minimum calcination temperature of 900°C is required to crystallize $La_{1-x}Sr_xMnO_3$, which does not allow the synthesis of NP with $\langle s \rangle_{XRD} \leq 19$.

According to theory, in Regime 1 the nanoparticle size is expected to decrease if R_w decreases, since the reduction of the water-to-surfactant ratio is expected to result in lower diameter micromicelles, which reduces the resultant nanoparticle size. However, Fig. 4.1 shows the opposite trend: the largest nanoparticle size is obtained for the lowest R_w, both for $LaCoO_3$ and $La_{1-x}Sr_xMnO_3$. The reason behind this reversal of trend is not yet fully understood, but in Regime 1 additional effects such as non-linear reaction dynamics seem to play a major role in controlling resultant NP size [180, 182, 183]. The relationship of R_w and NP size $\langle s \rangle$ must be largely determined empirically [180].

4.1.2 Chemical composition of $La_{1-x}Sr_xMnO_3$

Unexpectedly, the Sr concentration x varies considerably for different NP samples of $La_{1-x}Sr_xMnO_3$ despite identical precursor concentrations ($x_{\text{initial}} = 0.25$) (see Table 3.2). The highest x value observed in the NPs is $x = 0.47 \pm 0.04$. In Regime 1, where microemulsions are stable, x tends to be higher for smaller R_w. Thus, the following explanation seems to be plausible: The strongly positive La^{3+} ion can be immobilized at the water-surfactant interface by the charged hydrophilic head of the surfactant [180]. In this case, no hydroxide precipitation occurs for those La^{3+} ions, and the relative amount of Sr increases. If the surfactant concentration increases, i.e. R_w, is reduced, more La is immobilized and therefore lost, and the nucleated particles show an excess of Sr. In line with this conjecture, the Sr concentration within each sample batch was found to be homogeneous by EELS and TEM-EDX, even if there is a small variation Δs of NP sizes within one batch. This is likely due to the fact that the particle-size variation within a batch develops during calcination, whereas the Sr content is fixed at the nucleation stage in the microemulsion.

4.2 Structural changes

As shown in Chapter 3, both $LaCoO_3$ and $La_{1-x}Sr_xMnO_3$ nanoparticles show size-dependent increase of the lattice parameters and M-O atomic distances, whereas the bond angle $\theta_{\text{M-O-M}}$ decreases as S/V increases. Systematic studies on oxide nanoparticles reveal a general trend of unit-cell expansion as $\langle s \rangle$ decreases (S/V increases) [9, 20, 28, 29, 232–237], but the mechanism is still under debate. Here, the differences between $LaCoO_3$ and $La_{1-x}Sr_xMnO_3$ are compared, and a mechanism of size-induced lattice expansion is suggested.

4.2.1 Unit-cell expansion – comparison between $LaCoO_3$ and $La_{1-x}Sr_xMnO_3$

Comparing $LaCoO_3$ to $La_{1-x}Sr_xMnO_3$ nanoparticles in Fig. 4.2, it can be seen that all the structural parameters Y_i deviate increasingly from bulk values $Y_{i,\text{b}}$ with decreasing NP size, i.e., increasing S/V, for both materials. However, the relative changes $\Delta Y_i/Y_{i,\text{b}}$ are much larger for $La_{1-x}Sr_xMnO_3$ than for $LaCoO_3$. A $LaCoO_3$ NP sample with $\langle s \rangle$ = 19 nm shows an increase in unit-cell volume $\Delta V_{\text{uc}}/V_{\text{uc,b}}$ of 0.3%. In contrast, a unit-cell expansion of 1% was measured for a $La_{1-x}Sr_xMnO_3$ sample with $\langle s \rangle$ = 20 nm. Similarly for all $\Delta Y_i/Y_{i,\text{b}}$, the relative changes are much larger for $La_{1-x}Sr_xMnO_3$ compared to $LaCoO_3$. The maximum increase of the Mn-O distance is about 2% and the greatest reduction of the bond angle amounts to 5% for $La_{1-x}Sr_xMnO_3$ with a minimum mean size of $\langle s \rangle$ = 20 nm. On the other hand, the maximum increase of the Co-O distance $\Delta d_{\text{Co-O}}/d_{\text{Co-O,b}}$ is only 0.26% for $LaCoO_3$ with a size as small as $\langle s \rangle$ = 9.5 nm. The values of $\text{d}(\Delta d_{\text{M-O}}/d_{\text{M-O,b}})/\text{d}S/V$ are (0.37±0.15)%/nm^{-1} and (4±1.5)%/nm^{-1} for $LaCoO_3$ and $La_{1-x}Sr_xMnO_3$, respectively. Interestingly the size-dependent relative expansion of the Co-O bond length in $La_{0.5}Sr_{0.5}CoO_3$ was found to be (1.2±0.2)%/nm^{-1}, i.e. smaller than $La_{1-x}Sr_xMnO_3$, but significantly larger than the pure $LaCoO_3$ compound [238, 239]. $La_{1-x}Sr_xCoO_3$ has a mixture of Co^{3+} and Co^{4+}, analogous to $La_{1-x}Sr_xMnO_3$ [47]. A direct comparison between $La_{1-x}Sr_xMnO_3$ and the parent compound $LaMnO_3$ is difficult, as decreasing the NP size of orthorhombic $LaMnO_3$ leads to a size-dependent reduction of the orthorhombic distortion, accompanied by a shrinkage of the *a* and *b* lattice parameters and the unit-cell volume [240]. However, the microstrain associated with the decrease of the orthorhombic distortion is 0.33%/nm^{-1}, which is closer to the values measured for the Co-O bond strain in rhombohedral $LaCoO_3$ than the ones for $La_{1-x}Sr_xMnO_3$ NPs in the present project. Unfortunately, the Mn-O bond length was not assessed separately in Ref. [240].

Several mechanisms for size-induced unit-cell expansion have been discussed in the literature: First of all, there seems to be a dependence of structural changes in nanoparticles on the synthesis procedure [28, 241]: microemulsion synthesis seems to lead to lattice expansion in CeO_2 NP, whereas directly precipitated NP have a contracted unit cell. This is explained by a lower defect density in CeO_2 obtained from direct precipitation. Using the same calcination temperature for different NP sizes as was done in the present study, reduces the possibility of different defect densities for different batches and leads to a

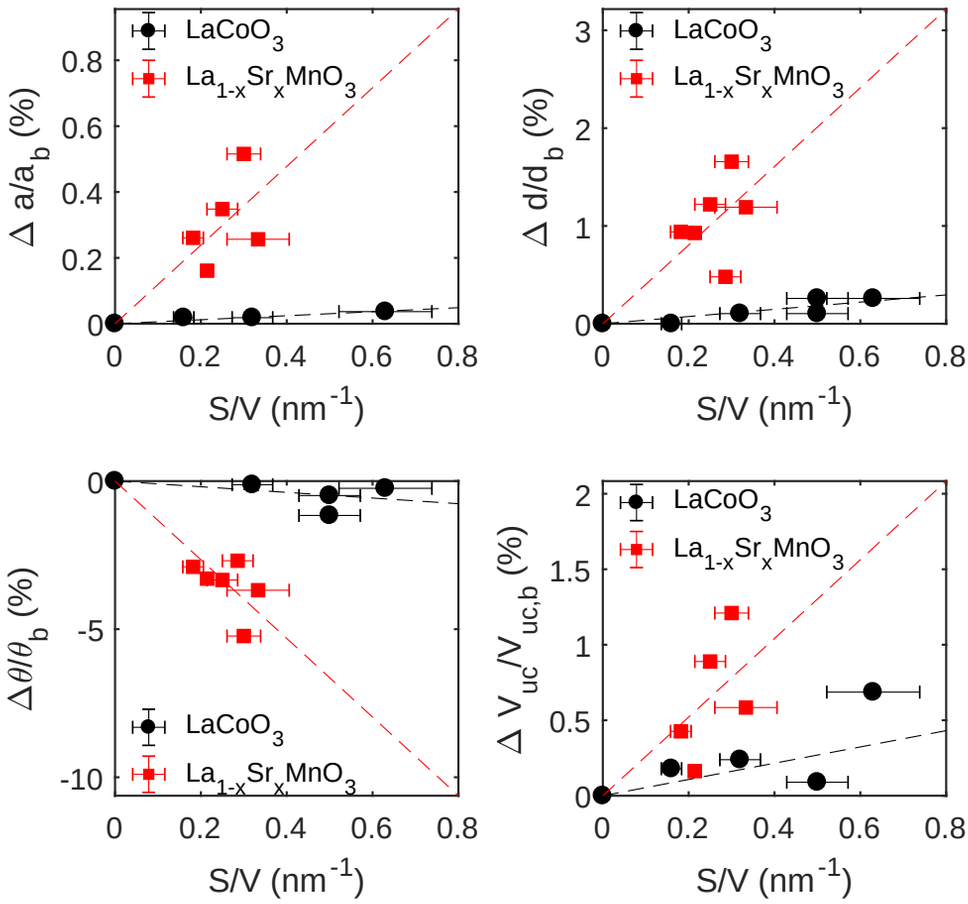

Figure 4.2: The relative changes $\Delta Y_i/Y_{i,\mathrm{b}}$ of (a) the rhombohedral lattice parameter a, (b) the metal-oxygen bond length $d_{\text{M-O}}$, (c) the M-O-M bond angle $\theta_{\text{M-O-M}}$, and (d) the unit-cell volume V_{uc}, compared to the bulk values as a function of surface-to-volume ratio S/V, for $LaCoO_3$ (black circles) and $La_{1-x}Sr_xMnO_3$ (red squares). For $La_{1-x}Sr_xMnO_3$, the changes are related to bulk values with the same Sr concentration x. The dashed lines are extrapolations to the bulk, i.e. $\Delta Y_i = 0$ and $S/V = 0$.

linear increase of the lattice parameters with increasing S/V ratio, which suggests an effect based on the surface.

Considering defects, it is well known that oxygen vacancies (V_{O}) can be formed at the surface of oxides [31, 215, 241, 242]. Therefore, any increase in S/V is expected to result in significantly higher $[V_{\mathrm{O}}]$. This can lead to a size-dependent increase of V_{uc} and $d_{\text{M-O}}$ in perovskites [146, 243, 244]. However, the multiplet fitting of NEXAFS results yield an oxygen vacancy concentration $[V_{\mathrm{O}}]$ of only 1.3% and 1.5%, for $LaCoO_3$ NP samples with $\langle s \rangle = 9.5$ nm and $\langle s \rangle = 37$ nm, respectively. There is also no strong influence of S/V on $[V_{\mathrm{O}}]$ (see Table 3.3), which suggests that the influence of S/V on V_{uc} and $d_{\text{M-O}}$ is probably not related to $[V_{\mathrm{O}}]$.

Moreover, in $La_{1-x}Sr_xMnO_3$ a high concentration of oxygen vacancies is inconsistent with the magnetic properties: by charge neutrality, a high concentration of oxygen vacancies would result in a reduction of the ratio Mn^{4+}/Mn^{3+}, effectively reducing the hole doping x. With respect to the $La_{1-x}Sr_xMnO_3$ phase diagram shown in Fig. 1.6, an increase of T_C would be expected for NP with $x \geq 0.4$, and a decrease of T_C for NP with $x \leq 0.4$, if x reduces as a function of size. However, the NP sample with $x = 0.47$ displays a strongly reduced T_C with respect to bulk, just as NPs with $x \leq 0.4$. It is not only the trend of T_C vs S/V, that is inconsistent with $[V_O]$ being the origin of the size-induced structural modifications and the decrease of T_C, but also the magnitude of T_C reduction: To achieve a V_O-related reduction of T_C by 10% at $x = 0.39$, δ in $La_{1-x}Sr_xMnO_{3-\delta}$ is expected to be 0.09 according to Fig. 1.6. However, the measured V_O concentration is only $\delta \leq 0.05$ (see Section 3.1.2.2). Hence, one can rule out the influence of oxygen vacancies on structural modifications at the nanoscale, in agreement with the considerations in Ref. [29].

Intrinsic reasons for the generally observed unit-cell expansion, such as surface energy, have also been considered: Ref. [29] has suggested a model based on the surface energy, where the volumetric expansion $\Delta V/V = -\Delta p/B$, with B the bulk modulus of the material and $\Delta p = \frac{2}{R} f_s$, where f_s is the surface stress. However, the simulated results over-estimate the expected expansion by a factor of 2 compared with experimental results [9]. The discrepancy is most likely due to the value of the bulk modulus B being dependent on the crystallite size [29], as has been shown for example for ZnO [245]. The bulk modulus was not adjusted to size in Ref. [9]. Additionally, pristine nanoparticle surfaces were considered for estimating f_s, while the broken bonds at the surface are usually saturated, e.g. by hydroxy groups [246], which lowers the effective surface stress.

Another way to decrease the surface energy is by crystalline reconstruction: This possibility was investigated using TEM HR images. Measuring the lattice spacing d_{hkl} perpendicular to NP facets both for $LaCoO_3$ and $La_{1-x}Sr_xMnO_3$ samples, and comparing the value of d_{hkl} with the value from XRD, it is possible to identify the Miller indices of the NP facets parallel to the electron beam. For example, a sample with $\langle s \rangle = 12$ nm shows, that the most frequent facets are the trigonal (006) with $d_{006} = 2.16 \pm 0.003$ Å and an occurrence of 15%, and the (110) planes with $d_{110} = 2.71 \pm 0.003$ Å and an occurrence of 13%. This suggests the presence of oxygen vacancies, which according to calculations performed by Ref. [242] prefers equal prevalence of (110) and (100) facets in thermodynamic equilibrium and is in agreement with NEXAFS measurements showing a Co^{2+} concentration of about 8%. The lattice spacings from XRD, TEM HR image analysis and TEM electron diffraction are the same within experimental accuracy. Assuming a clean NP surface, atomistic simulations considering the surface energy show that the relaxation of the (100) surface results in sinusoidal displacement of the Co-O plane some 3.5 nm into the bulk [242]. The main displacement is moving O ions from the Co-O plane to the outer La-O plane by 1.6 Å [215]. In a pseudo-cubic consideration, i.e. neglecting the rotation of the $[CoO_{6/2}]^{3-}$ octahedra, that would correspond to a change in $\Delta d_{\text{Co-O}}/d_{\text{Co-O,b}} \approx 0.13\%$ at the topmost plane, which corresponds to just half of the maximally observed $\Delta d_{\text{Co-O}}/d_{\text{Co-O,b}} = 0.26\%$ for $\langle s \rangle = 9.5$ nm. The experimentally observed expansion is an average value for the entire batch of NPs, whereas the theoretically computed $\Delta d_{\text{Co-O}}/d_{\text{Co-O,b}} = 0.13\%$ is only found at the surface, and decreases into the

bulk. More recent simulations show that the thermodynamically stable surfaces are the hexagonal ($\bar{1}14$) with O_2 termination, (001) with LaO_2 termination and ($1\bar{1}2$) LaO p(1×1) facets [247]. The second one of these, (001), shows an inward relaxation of cations, and oxygen ions relax outwards, with a bond length difference of only up to 0.175 Å [248]. Therefore, surface reconstruction alone is not sufficient to explain the observed unit-cell expansion.

Instead, surface adsorbates are considered: It has been shown that oxide nanoparticles frequently show a thin layer of hydroxide at the surface due to chemisorption [231, 249]. Ref. [231] has considered the adsorption of H_2O at surface oxygen vacancies. The adsorbed water molecule transfers one proton to a surface O^{2-} ion, resulting in two OH^- ions bound to two separate Co^{3+} ions. The valence state of the Co^{3+} ion remains unchanged, but the ion is now coordinated with five oxygen and one OH^- ion. This effect lowers the electron density at the surface of the nanoparticles compared to a surface with exposed O^{2-} ions. Additionally, the Co-OH bond is weaker than the Co-O bond, which results in an increase in bond length. For $La_{1-x}Sr_xMnO_3$ an additional effect is possible: at the Mn^{3+} ion, the energy of the electrons can be lowered by lifting the degeneracy of the e_g levels by the Jahn-Teller (JT) effect (see page 7), leading to localization of the electron. The double-exchange mechanism leads to delocalization, i.e. sharing of the e_g electron between two $Mn^{3.5}$ ions, which counteracts the JT effect. Mn ions at the surface are missing an oxygen ion to bind to, which probably leads to a slightly different coordination or adsorption of water, forming a hydroxy bond. The resulting localization of the electron could lead to an increase in bond length via electron-phonon coupling [41, 149]. As the increase in bond length is present everywhere at the surface, an incrase in S/V could result in the observed increase of $d_{\text{Mn-O}}$. Ref. [250] show that the Mn-O bond length in $La_{1-x}Ca_xMnO_3$ decreases by about 20% when cooling through the Curie temperature, i.e. going from a localized insulating system to the delocalized double-exchange coupled system. Although it is likely that the decrease is weaker in $La_{1-x}Sr_xMnO_3$ [41], this additional influence on the lattice strain by electron-phonon coupling could help understand the difference between size-induced lattice expansion in $LaCoO_3$ and $La_{1-x}Sr_xMnO_3$ NPs. Additionally, the localization of e_g electrons at the surface could result in the lowering of the saturated magnetic moment described in Section 3.3.2 on page 57.

Co^{3+}, on the other hand, is not JT active in the LS or HS states and at the low concentration of Co^{3+} HS in the NPs studied in the present thesis, the electrons cannot delocalize throughout the lattice. Therefore there is no significant change in electron configuration at the surface of NPs, and the increase in bond length is only related to the electron-pulling effect of the hydroxide group at the Co^{3+}. This conjecture is also consistent with the observation that size-induced lattice expansion in $La_{1-x}Sr_xCoO_3$ [238] is larger than in $LaCoO_3$ (see page 61), due to double exchange between Co^{3+} and Co^{4+} in bulk and possible localization of the electron at the surface, potentially resulting in size-dependent lattice expansion compared to bulk $La_{1-x}Sr_xCoO_3$. The difference in unit-cell expansion between $La_{1-x}Sr_xMnO_3$ and $La_{1-x}Sr_xCoO_3$ could be due to the difference in electron-phonon coupling.

The Llattice-expansion mechanism based on surface adsorption could also explain the lack of consistency in literature with respect to the quantitative influence of NP size on lattice parameters, as surface adsorption is difficult to control and can lead to ageing

effects. In the present study, XRD and SQUID measurements were performed immediately after calcination, hence one can assume a small influence of hydroxides. If more time elapses between calcination and measurement, the unit-cell expansion can be larger, as published in Refs. [76, 77, 96, 97].

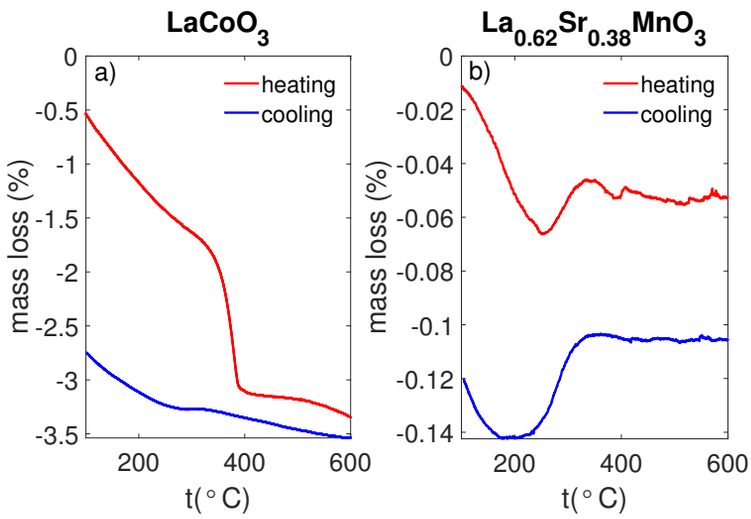

Figure 4.3: Thermogravimetry curves for (a) $LaCoO_3$ and (b) $La_{1-x}Sr_xMnO_3$. Heating (red curve) and cooling (blue curve) were both performed at 10°C/min.

In order to compare the adsorption in $LaCoO_3$ and $La_{1-x}Sr_xMnO_3$ nanoparticles, two samples with comparable nanoparticle size ($\langle s \rangle = 19$ nm and $\langle s \rangle = 20$ nm, respectively) were analysed in thermogravimetry. The results are shown in Fig. 4.3. Fig. 4.3 (a) shows the decrease of mass with increasing temperature for $LaCoO_3$: up to about 300°C the mass of the sample decreases by about 1.5% due to release of adsorbed water and other species. The ensuing sharp drop in mass, which is completed at about 390°C, is due to deoxylation of chemisorbed hydroxy groups at the Co^{3+} ions [109, 251]. Although similar deoxylation processes could be expected for hydroxide groups at the La^{3+} ion, the deoxylation of LaOOH is expected at $t \geq 500$°C [252, 253], where no mass loss is observed. The drop in mass at 390°C is about 1.2%, which is one order of magnitude higher than for polycrystalline samples [254]. This is to be expected as water adsorbs to the surface and nanoparticle samples have a much higher surface-to-volume ratio. Since 18 g of mass is lost for each mole of desorbed water, the mass loss can be converted to (17±2)mol%. The following relationship can be used to estimate the fraction of Co ions at the NP surface of a perfectly spherical nanoparticle [255]:

$$\frac{N_S}{N_{\text{total}}} = \frac{3a}{2R} \tag{4.1}$$

with a being the lattice constant and R the spherical particle radius. For the sample with $\langle s \rangle = 19$ nm this yields (13±3)% of all Co ions located at the surface. Taking into consideration that the nanoparticles are not perfectly spherical, their surface is larger than anticipated in Equation 4.1. Therefore, it can be assumed that at least all surface

Co ions were fully saturated with hydroxides. The continuous desorption up to 300°C, is partially reversible even at fast cooling rates. However, as shown in Fig. 4.3(a), the cooling curve does not show the same step at about $t = 390°$ C, i.e. the decomposition of these surface hydroxides is irreversible in this experiment. It can take about 40 hours in moist atmosphere for oxides to convert fully back to hydroxides [253], but the cooling rate in the present experiment is only 10°C/min. However, hydroxides are re-adsorbed from air, if the sample is left to stand for a week: Repeating the TGA experiment on the same sample directly after the first heat treatment results in no mass loss at $t = 390°$ C, but after a week the same sample shows the same mass loss as shown in Fig. 4.3(a).

In hexagonal CoO(OH) the Co-O bond length is 1.94 Å [256]. This is 0.5% larger than the value for $d_{\text{Co-O}}$ in $LaCoO_3$. In the case of a sample with $\langle s \rangle = 9.5$ nm and assuming a spherical shape, the ratio of $N_S/N_{\text{total}} = 0.17$. From the mass loss in thermogravimetry one can assume that all 17% of Co ions at the surface have an elongated bond length. Due to elastic strain, probably more than the surface layer will be affected. Considering that atomic relaxation at pristine $LaCoO_3$ surfaces decays to zero only within a distance r_0 of 3.5 nm into the material [215], it is likely that the weakening of the Co-O bond occurs over the same range. Therefore, each NP can be pictured as having a strained shell of 3.5 nm thickness. In a gross over-simplification, a linear decay from $d_{\text{Co-O}}$ at the surface to the bulk $d_{\text{Co-O,b}}$ at a distance of 3.5 nm from the surface can be assumed, which leads to progressively reducing Co-O bond length from the surface through the thickness of the strained shell. $d_{\text{Co-O}}$ can then be expressed as a function of the radial distance from the centre of a NP (r) in the following way:

$$d_{\text{Co-O}}(r,s) = \begin{cases} d_{\text{Co-O,b}} & \text{if } 0 \le r \le s/2 - r_0 \\ d_{\text{Co-O,b}} + m \times (r - (s/2 - r_0)) & \text{if } s/2 - r_0 \le r \le s/2 \end{cases} \tag{4.2}$$

where $m = (d_{\text{Co-OH}} - d_{\text{Co-O,b}})/(3.5\text{ nm})$, and $s/2$ is the particle radius. Using $\mathrm{d}V = 4\pi r^2 \mathrm{d}r$, i.e. a spherical shell with infinitesimal thickness, and integrating troughout the strained shell of 3.5 nm thickness (r_0), the average Co-O bond length as a function of the nanoparticle size s, $\langle d_{\text{Co-O}} \rangle (s)$ is estimated as follows:

$$\langle d_{\text{Co-O}} \rangle (s) = \frac{V_{\text{int}} \times d_{\text{Co-O,b}} + \int_{s/2-r_0}^{s/2} d_{\text{Co-O}}(r,s) \times 4\pi r^2 \mathrm{d}r}{V_{\text{total}}} \tag{4.3}$$

with V_{int} and V_{total} the unstrained and the total NP volume, respectively.

Applying Equation 4.2 to NP samples with $\langle s \rangle = 9.5$ nm and $\langle s \rangle = 19$ nm the average Co-O bond length is $d_{\text{Co-O}} \approx 1.937$ Å and $d_{\text{Co-O}} \approx 1.935$ Å, respectively. For the sample with $\langle s \rangle = 9.5$ nm this corresponds to $\Delta d_{\text{Co-O}}/d_{\text{Co-O,b}} \approx 0.3\%$, which in view of the approximations used is surprisingly close to the experimental value of (0.26±0.1)%. For a sample with $\langle s \rangle = 19$ nm, $\Delta d_{\text{Co-O}} = 0.2\%$, compared to the experimental value of (0.1±0.1)%, with only an agreement of a factor of two only.

A similar estimation can be done for $La_{1-x}Sr_xMnO_3$: The Mn-OH bond length in MnOOH is about $d_{\text{Mn-OH}} = 2.34$ Å [257]. The relaxation distance of surface reconstruction effects is close to 1 nm [258]. Using Equations 4.2–4.3, the expected strain for a

nanoparticle with $\langle s \rangle = 18$ nm is $\Delta d_{\text{Mn-O}}/d_{\text{Mn-O,b}} \approx 1.1\%$, which is within the uncertainty of the experimental value of $\Delta d_{\text{Mn-O}}/d_{\text{Mn-O,b}} = 1.8 \pm 0.9\%$.

In contrast to $LaCoO_3$, $La_{1-x}Sr_xMnO_3$ shows very little change in mass upon heating (Fig. 4.3 (b)). The continuous desorption process reduces the sample mass by only 0.06%. There seems to be a slight increase in mass at 350°C, which is attributed to the presence of SrO [259] and seems to be fully reversible. An irreversible mass loss is registered at about 400°C, and is associated with the decomposition of weakly bound hydroxides bound to Mn^{2+} ions at the nanoparticle surface [260–263]. Since the change in mass is only 0.01 wt%, i.e. in the case of water desorption 0.15 mol%, the majority of hydroxides bound to Mn^{3+} and Mn^{4+} ions possibly remain stable up to higher temperatures. The ratio of formation enthalpies of CoO(OH) to MnO(OH) is 0.72 [264], and the deoxylation temperature of CoO(OH) is 390°C in Fig. 4.3, the estimated deoxylation temperature for MnO(OH) is $\approx$ 390/0.72 = 540°C. This only considers Mn^{3+} ions, but since the average valence is higher in $La_{1-x}Sr_xMnO_3$, it is quite possible that the desorption temperature is pushed to higher values. Unfortunately it cannot be measured at $t \geq 600$°C, because at that temperature significant oxygen uptake [265] and decomposition reactions commence [254] which makes it difficult to separate effects. Alternatively, there are only very few strongly bound hydroxy groups present in the first place, and lattice expansion in $La_{1-x}Sr_xMnO_3$ is due only to the effective negative pressure due to surface energy described above on page 63. In that case, the more pronounced size-dependent lattice expansion in $La_{1-x}Sr_xMnO_3$ due to intrinsic surface-induced pressure could be related to higher surface energy for clean surfaces, compared to surfaces where the dangling bonds are saturated, as is the case in $LaCoO_3$ (see Fig. 4.3).

To analyse the influence of surface adsorption on the lattice parameters further, XRD was carried out on the sample with $\langle s \rangle = 19$ nm shown in Fig. 4.3 before and after TGA treatment, i.e. once with a hydroxide shell and once after deoxylation. The lattice parameters change according to Table 4.1.

Table 4.1: The Co-O bond length $d_{\text{Co-O}}$ and average magnetization at T 5 K and $\mu_0 H = 7$ T $\langle m \rangle_{5\text{ K},7\text{ T}}$ of the sample with $\langle s \rangle = 19$ nm, before and after heat treatment at 600°C shown in Fig. 4.3.

	before heat treatment	after heat treatment
$d_{\text{Co-O}}$ (Å)	1.930 ± 0.003	1.918 ± 0.003
$\langle m \rangle_{5\text{ K},7\text{ T}}$ (μ_B/Co)	0.140 ± 0.004	0.132± 0.004

Within error, the value before heat treatment agrees with $d_{\text{Co-O}}$ measured directly after calcination ($d_{\text{Co-O}} = 1.933$, see Table 3.1). It is possible that both the surface concentration of hydroxides and the concentration of oxygen vacancies increases due to ageing. However, both effects are expected to result in a larger unit cell, and hence larger $d_{\text{Co-O}}$, which is not the case. In particular, the $d_{\text{Co-O}}$ value after calcination is reduced significantly below the bulk value. While the difference between measurements before and after heat treatment (TGA) can be understood in terms of desorption of hydroxides,

the lowering below the bulk value remains unclear, but could possibly be related to healing of crystalline defects.

The average magnetic moments of $\langle m \rangle_{5\,\mathrm{K},7\,\mathrm{T}} = 0.14\ \mu_\mathrm{B}/\mathrm{Co}$ and $0.13\ mu_\mathrm{B}/\mathrm{Co}$ were measured before and after heat treatment, respectively, showing the same paramagnetic behaviour as observed after calcination. The reduction in magnetic moment can be related to the reduction in $d_{\mathrm{Co\text{-}O}}$ according to Fig. 3.15(b). However, the small reduction in magnetic moment associated with the large reduction in $d_{\mathrm{Co\text{-}O}}$ suggests additional effects due to heat treatment, which are not yet understood. More systematic studies including $LaMnO_3$ and $La_{1-x}Sr_xCoO_3$ NPs are required to verify the mechanism of size-induced lattice expansion.

4.3 Magnetic properties

The structural changes described in Section 3.2 have a profound effect on both $LaCoO_3$ and $La_{1-x}Sr_xMnO_3$ nanoparticles. While bulk $LaCoO_3$ is non-magnetic and the reduction of size induces a magnetic moment by stretching the Co-O bond, bulk $La_{1-x}Sr_xMnO_3$ is a ferromagnet governed by double exchange between Mn^{3+} and Mn^{4+}. Therefore, stretching the Mn-O bond in the latter case will have the effect of weakening the magnetic coupling.

4.3.1 Influence of unit-cell expansion and strain on magnetic properties of $LaCoO_3$ nanoparticles

It has been shown in the introduction that the magnetic properties of $LaCoO_3$ are sensitive to structural parameters. In particular, the ground-state magnetic moment depends critically on the rhombohedral distortion δy. As a size dependent expansion of the unit cell has been demonstrated in section 3.2.1, a modification of the magnetic behaviour is expected.

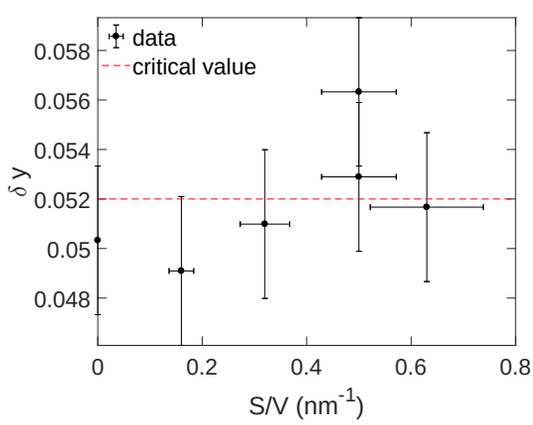

Figure 4.4: Evolution of structural parameter δy as a function of surface-to-volume ratio S/V. The red dashed line marks the critical value of $\delta y = 0.052$, below which the ground state of $LaCoO_3$ is magnetic according to Ref. [44].

Using Equation 1.5 δy is calculated between 0.049 ± 0.003 and 0.056 ± 0.003 (see Fig. 4.4). Below $\delta y = 0.052$ DFT calculations result in a magnetic ground state of $LaCoO_3$ with $\mu_{\text{eff}} = 1.3\mu_B$/Co [44]. The data presented in Fig. 4.4 was measured at room temperature, and as the thermal expansion of $LaCoO_3$ is non-linear [48], the low-temperature structural parameters are unknown. Within experimental accuracy most samples have $\delta y \approx 0.052$. If anything, there is an increase in δy with decreasing NP size. This is in contradiction to previously discussed data. It cannot be ruled out, that NP size influences the thermal expansion behaviour, too.

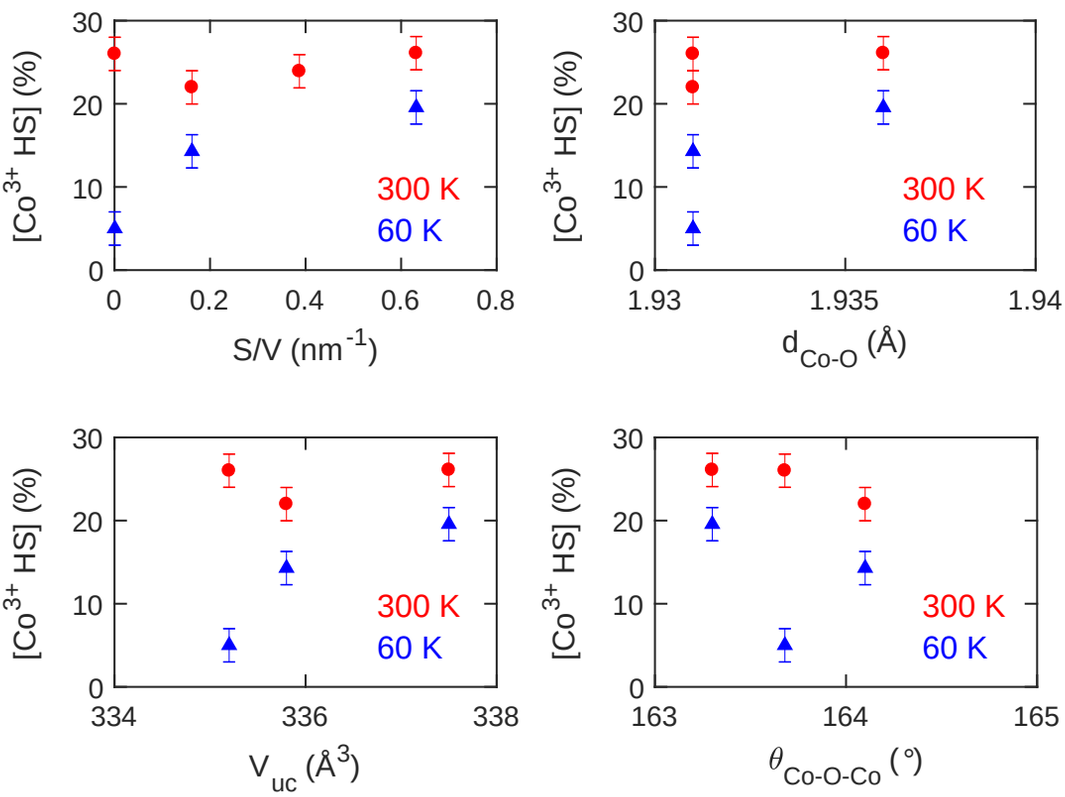

Figure 4.5: Concentration of $LaCoO_3$ in the high-spin state (HS) at 300 K (red circles) and 60 K (blue triangles) as obtained from multiplet fittings to near-edge X-Ray absorption fine structure (NEXAFS) spectra as functions of (a) the surface-to-volume ratio S/V (accuracy given in Table 3.1), (b) the Co-O atomic distance d_{Co-O} (accuracy: ± 0.002 Å), (c) the unit-cell volume V_{uc} (accuracy: ± 0.8 Å^3) and (d) the Co-O-Co bond angle $\theta_{Co-O-Co}$ (accuracy: ± 0.5 °).

As outlined in Section 2.3.2.1, multiplet simulations to the near-edge X-ray absorption fine structure (NEXAFS) spectra allows for the calculation of the concentration of $LaCoO_3$ HS ions as well as the concentration of Co^{2+}, which is related to δ in $LaCoO_{3-\delta}$. The results are given in Table 3.3. Fig. 4.5 (a)-(d) shows the concentration of Co^{3+} HS at 60 K and at 300 K as functions of S/V, $d_{\text{Co-O}}$, V_{uc}, and $\theta_{\text{Co-O-Co}}$. For data measured at $T = 60$ K,

there is a relationship between [HS] and S/V, as well as between [HS] and V_{uc}. This is to be expected as V_{uc} depends on S/V as discussed above, and the expansion of the unit cell stabilizes the HS state. The most significant contribution to the expansion of the unit cell is the elongation of $d_{Co\text{-}O}$, which accommodates the larger atomic radius of Co^{3+} HS. However, there is no significant difference between the $d_{Co\text{-}O}$ values for bulk and the sample with $\langle s \rangle = 37$ nm, i.e. $S/V = 0.16$. This could be a precision effect, as the increase of [HS] from 13% to 18% at $T = 60$ K is significant when increasing $d_{Co\text{-}O}$ from 1.931 Å to 1.936 Å. On the other hand, there is no correlation between [HS] and $\theta_{Co\text{-}O\text{-}Co}$, which supports the claim that size-induced increase of the interatomic distance results in stabilization of the [HS] state, as this mechanism is not very sensitive to $\theta_{Co\text{-}O\text{-}Co}$. At $T = 300$ K the difference in [HS] is negligible for NP and bulk, despite significant changes in unit-cell volume and Co-O distance. This has also been observed in thin films [1, 69] and heavily Ni-doped $LaCoO_3$ [266]: the tensile strain seems to mainly prevent the HS→LS transition at low temperatures.

Considering the mechanism suggested by Ref. [231], the coordination of Co^{3+} at the surface with five O^{2-} and one OH^- ions can be compared to the coordination of Co^{3+} in Sr_2CoO_3Cl, which has Co^{3+} in the high-spin state. Consequently, the adsorption of H_2O could double the surface concentration of Co^{3+} HS ions. The sample with $\langle s \rangle = 9.5$ nm has roughly 17% of its ions at the surface, and a Co^{3+} HS concentration of 18% at 60 K. The sample with $\langle s \rangle = 37$ nm on the other hand has 4% surface ions, and a Co^{3+} HS concentration of 13% at 60 K. Particularly in the latter case, the surface would have to be completely HS, and some of the bulk as well, to account for [HS]=13%. Assuming that this is not favoured [50, 267] due to structural strain (the atomic radius of Co^{3+} HS is larger than that of Co^{3+} LS), intermixing of HS and LS is expected in a surface layer of finite thickness. Within this thickness, the HS concentration most probably would exceed the percolation threshold, i.e. a ferromagnetic phase would form. There is no indication for ferromagnetism in the magnetization data shown exemplarily in Fig. 3.20 or Fig. 3.14. Therefore, strong clustering of Co^{3+} HS ions is excluded.

One can compare NEXAFS data with the values obtained from Brillouin fits to the virgin magnetization data displayed in Fig. 3.17 (a). As outlined in Section 3.3.1.2, the [HS] values obtained from the Brillouin fits might be constantly higher, as the Co^{2+} contribution can accounted for by a constant addition of 0.02 to the Co^{3+} HS concentration. For comparison with NEXAFS, this value will be subtracted. Here only up to 14% of the Co^{3+} ions are HS at 40 K, for a sample with $\langle s \rangle = 9.5$ nm. NEXAFS analysis, described in 3.3.1, yields a concentration of Co^{3+} in the high-spin state of (18±2)% at 60 K and for $\langle s \rangle = 9.5$ nm. Although it was not possible to measure NEXAFS at lower temperatures, extrapolating the curve for $S/V = 0.61$ to $T = 60$ K yields a value of (15 ± 3)%, which agrees with the results of the multiplet simulation. For the second sample analysed by NEXAFS, the [HS]=(13±2)% at 60 K, whereas the extrapolated value from the fits yields (10 ± 2)%, i.e. it agrees as well within experimental error.

In summary, the combination of NEXAFS measurements and analysis of magnetization data measured with SQUID magnetometry lead to the conclusion that there is no magnetic phase separation in $LaCoO_3$ nanoparticles. Most importantly, using two-phase models to fit the measured SQUID data, i.e. a ferromagnetic and a paramagnetic phase, the

resultant Co^{3+} HS concentration peaks at 30 K and [HS]=10% only at 40 K for the smallest nanoparticle sample. The first effect is in contradiction to the literature on bulk $LaCoO_3$, indicating monotonic increase of [HS] with temperature, whereas the second effect is in contradiction to the NEXAFS results on the same NP sample. Note that a single magnetic phase as fitted in the present study is in contrast to Refs. [76, 77, 96–99], all of which assume phase separation into ferromagnetically ordered domains and antiferromagnetic or non-magnetic regions. The ferromagnetic phase is assumed based on the presence of magnetic hysteresis. Actually, for NP with $\langle s \rangle \leq 20$ nm, one would assume single-domain behaviour without hysteresis. In Ref. [96], one can clearly see a widening of the hysteresis loop as the NP size increases, i.e. as the calcination temperature increases, which visibly leads to higher particle density. The anisotropy in this work could be an effect of increased particle-particle interaction rather than due to ferromagnetic domains. If the hysteresis was an indication for ferromagnetism, the coercivity would be expected to increase as the nanoparticle size decreases, and then vanish completely as small nanoparticles are likely single-domain. Therefore, the presence of magnetic anisotropy cannot be taken as proof for long-range ferromagnetism, particularly as one of the NP samples shows an increase in coercivity after TGA, although the size has not changed. Most importantly, as outlined above, neither the low concentration of Co^{3+} HS (which was not determined by any of the researchers cited above), nor the magnetic behaviour justifies magnetic phase separation. Moreover, the published data [76], [96] can be described by Equation 2.33, i.e. a Brillouin function with an internal field B_i, as shown in Fig. 4.6. The parameters corresponding to the best fit are tabulated in Table 4.2:

Table 4.2: The values of [Co^{3+} HS] and B_i fitted to data from literature and from the present thesis.

Ref.	T(K)	size (nm)	S/V (nm^{-1})	V_{uc} (Å)	[Co^{3+} HS]	B_i(T)
[76]	2	25	0.24	337.38	0.05 ±0.01	0.03 ±0.02
	2	32	0.19	336.18	0.04 ±0.01	0.01 ±0.005
[96]	5	60	0.1	336.83	0.07 ±0.02	0.18 ±0.09
	5	80	0.08	336.53	0.03 ±0.01	0.14 ±0.07
this project	5	9.5	0.63	337.5	0.06 ±0.02	0.31 ±0.08
	5	19	0.32	336.0	0.04 ±0.01	0.17 ±0.06
	5	37	0.16	335.8	0.03 ±0.01	0.24 ±0.07

Comparing these results to the data presented in the present thesis, the values for [Co^{3+} HS] are higher in Refs. [76] and [96]. As these studies have not taken Co^{2+} into consideration, but the presence of oxygen vacancies is very likely, the comparison will be done without subtracting the Co^{2+} contribution from the data measured on the samples prepared in this thesis. Although according to Table 3.1 there are no samples with the same sizes as in Table 4.2, one can use Fig. 3.17(b) to estimate the corresponding values. For example, at $T = 5$ K, the extrapolation predicts a [Co^{3+} HS] value of ≈ 0.02 for $s = 60$ nm, i.e. about 1/3 of what was measured in Ref. [96]. On the other hand, the

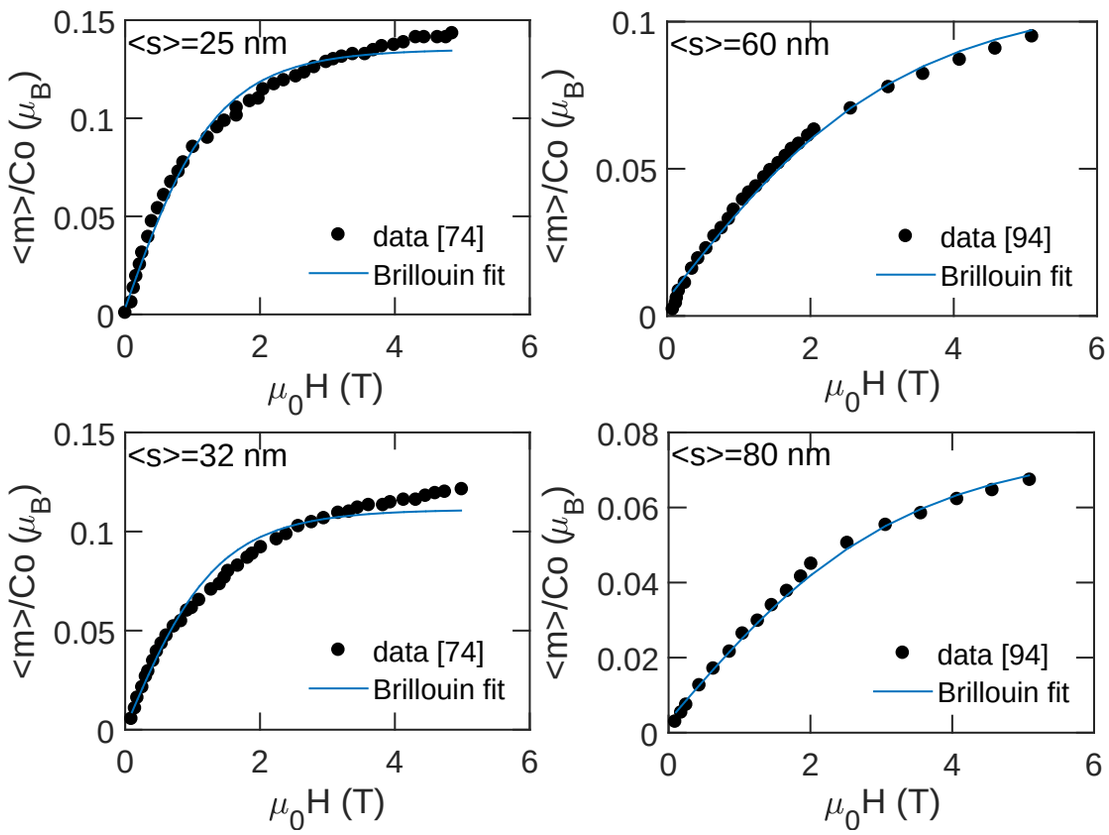

Figure 4.6: Brillouin fits to data extracted from Ref. [76], measured at $T = 2$ K (left) and Ref. [96], measured at $T = 5$ K (right), with different average NP size.

unit-cell volume in Ref. [96] for NP samples with $\langle s \rangle = 60$ nm is 336.8 Å, which is just slightly smaller than the unit-cell volume for the sample with $\langle s \rangle = 9.5$ nm in the present study, with a corresponding fitted [Co^{3+} HS] concentration of 0.063 ±0.002. Clearly, this value is much closer to the value given in Table 4.2 for the sample with $\langle s \rangle = 60$ nm. It was not possible to measure hysteresis curves at $T = 2$ K, but extrapolating the curve for the sample with $S/V = 0.63$ in Fig. 3.17(a) seems to indicate [Co^{3+} HS]≈ 0.04 at 2 K. This sample has the same unit-cell volume as the sample with $\langle s \rangle = 25$ nm in Ref. [76], which according to Table 4.2 has a [Co^{3+} HS]≈ 0.05. Hence, the relationship between unit-cell expansion and Co^{3+} HS concentration seems to be the same in this work and in Refs. [96] and [76], although the difference in synthesis procedure seems to lead to a variation in the relationship between S/V and $\Delta V_{uc}/V_{uc,b}$. This observation is in agreement with the analysis of magnetic moment in relation to NP size and Co-O distance $d_{Co\text{-}O}$, as stated in Table 3.4: The relationship between structural properties and magnetic properties seems to be the same in the present work and in Refs. [76, 96, 97], but the influence of NP size on structural parameters is not consistent (Table 4.2).

In epitaxially strained thin films, Pinta, Fuchs et al. have shown [Co^{3+} HS]=75% at $T \approx 100$ K [1], and $V_{uc} = 336$ Å^3 [69]. The unit-cell volume corresponds to the unit-cell

volume of the NP sample with $S/V = 0.32$, which at $T = 40$ K has [Co^{3+} HS]=12.5%, and is paramagnetic in contrast to the ferromagnetic thin films in Ref. [1]. The different behaviour despite comparable structural parameters is most likely due to the different strain states: in epitaxial thin films, the strain by definition is anisotropic, whereas in nanoparticles, the strain is most likely isotropic. This leads to tetragonal distortions in thin films [1], which is not observed in NP samples. Although the oxygen octahedra around the Co^{3+} ions apparently are not distorted anisotropically [94], the direct comparison of unit-cell volumes is not possible.

The values for B_i for data taken from Refs. [76] and [96] is of the same order of magnitude as the values obtained in the present study, but unfortunately no temperature-dependent data was published to allow a detailed comparison. Nonetheless it becomes clear that data measured on $LaCoO_3$ NPs previously can well be interpreted as a single paramagnetic system, with a small internal field, instead of a two-phase system. Moreover, comparing structure-dependent magnetization, the apparent discrepancies in size-induced magnetization vanish. This can be taken as confirmation of the assumption that the stabilization of the HS state is a consequence of lattice expansion, but at the same time, it is also an indication that synthesis procedure greatly influences the extent of lattice expansion. Finding an unambiguous relationship between nanoparticle size and Co-O atomic distance is therefore a project for future studies.

As mentioned above, accurate fits require the assumption of an internal field B_i. Apparently, the spin-spin interaction leads to short-range magnetic order, resulting in an internal magnetic field of small magnitude. For nanoparticles, the magnetic field generated by a nanoparticle can influence the spins of a neighbouring NP [268]. The weakness of the interaction compared to fully ferromagnetic materials can be attributed to the low number of atomic magnetic moments. The two aspects of B_i - its nature and its variation with temperature - are discussed below.

Fig. 4.7 shows the variation of B_i with temperature for samples with increasing S/V. In the same plot, the irreversibility fields B_{irr} and corresponding temperatures $T(B_{irr})$ are shown, i.e. the temperatures, at which the difference in m_{ZFC} and m_{FC} is 5% ($\Delta m/m_{FC} = 0.05$) at different applied fields $\mu_0 H$. Clearly, two regimes are identified: at $T \leq T(B_{i,max})$, the irreversibility field deviates strongly from $B_i(T)$ data (shaded regions), but for $T \geq T(B_{i,max})$, qualitatitve agreement is achieved. This regime shows monotonically decreasing irreversibility fields with increasing temperature, and correspondingly decreasing B_i with increasing temperature. This correlation indicates short-range magnetic order, which competes against temperature-induced disorder. Consequently, the irreversibility temperature approaches zero as the applied field increases towards infinity, as an infinitely high field can orient all spins even if the material has been cooled down in zero applied field.

In the low-temperature region, B_i decreases with decreasing temperature. The peak could indicate the influence of two competing effects: At low temperatures, the temperature-dependent Co^{3+} HS concentration dominates: The internal field increases as the concentration of Co^{3+} HS increases with temperature according to Fig. 3.17(a). At higher temperatures, on the other hand, the dominant effect is increasing thermal fluctuations, so that the internal field as well as the irreversibility field decrease with increasing temperature. The point where the two effects contribute equally, is expected at $T(B_{i,max})$,

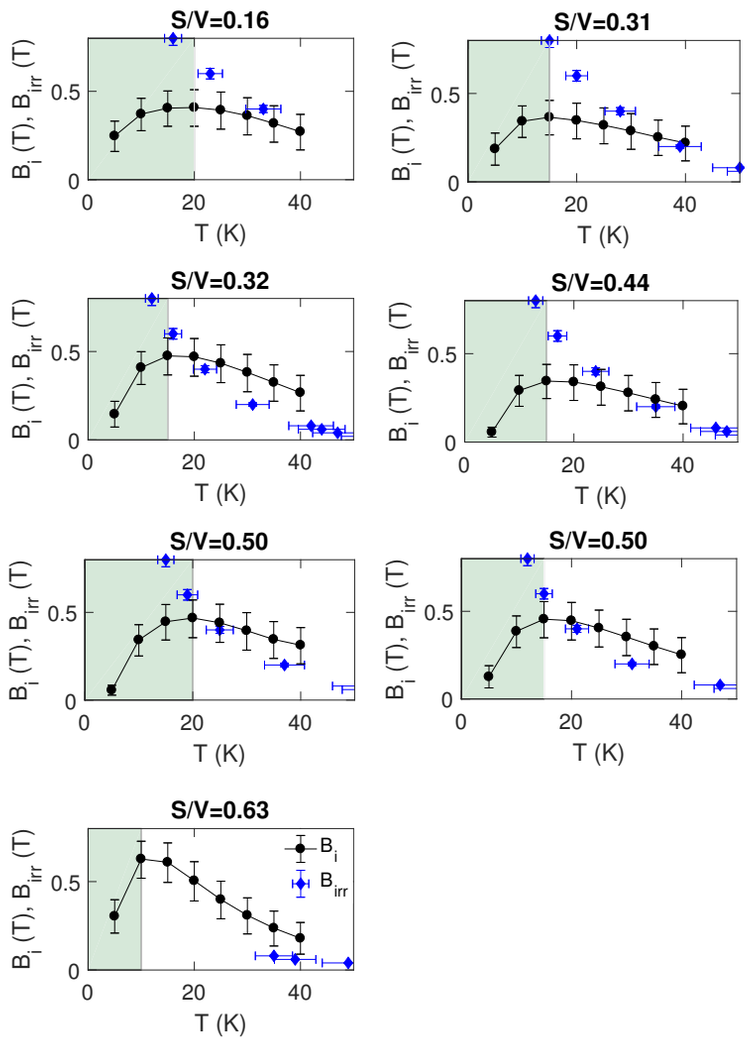

Figure 4.7: The values of B_i vs. T (black, lines are guides to the eye), the irreversibility field B_irr against the temperature at which the difference between field-cooled and zero-field cooled magnetization ($\Delta m/m_\mathrm{ZFC}$) is 5% (blue) for nanoparticle samples with different S/V. The shading separates the two different regimes (see text).

which is lower for samples with generally higher [Co^{3+} HS], i.e. higher S/V: Plotting $T(B_\mathrm{i,max})$ as a function of S/V in Fig. 4.8 shows that the maximum of the internal field shifts to lower temperatures if S/V increases.

There seems to be a critical [Co^{3+} HS] to establish correlations between magnetic moments. Once these correlations are established, thermal energy competes with these correlations. Therefore, in samples with larger S/V, the "critical" concentration $[Co^{3+}\ \mathrm{HS}]_\mathrm{crit}$ is reached at lower temperatures (see Fig. 3.17(a)). According to Fig. 3.17(a), a temperature of $\approx$ 15 K is required to achieve [Co^{3+} HS]=9% (i.e. 7% taking into account the Co^{2+} con-

tribution) for samples with $S/V = 0.5$, which corresponds to $T(B_{\mathrm{i,max}})$ for these samples according to Fig. 4.8.

As the atomic radii of ions in HS and LS state differ, elastic reasons as well as entropy of mixing [50] lead to a uniform distribution of the Co^{3+} HS ions in the lattice. Consider a Co^{3+} ion in the HS state. It has six neighbouring Co^{3+} ions. For ferromagetic superexchange coupling, two Co^{3+} ions in the HS state have to be next-nearest neighbours along a straight line, connected by two oxygen ions and a Co^{3+} ion in the LS state. Each Co^{3+} ion therefore has six of these next-nearest neighbours. The probability for six nearest neighbours being in the low-spin state and at least one of the six Co^{3+} ions connected in a straight line to the nearest neighbours being in the high-spin state can be calculated as:

$$\binom{6}{0} \times 0.07^0 \times 0.93^6 \times \binom{6}{1} \times 0.07^1 \times 0.93^5 = 0.189$$

i.e. at a HS concentration of 7% 18.9% of all Co^{3+} HS ion in the bulk of the particle are coupled to at least one other Co^{3+} HS ion ferromagnetically. $T(B_{\mathrm{i,max}})$ has an accuracy of ±4 K, which according to Fig. 3.17(a) leads to an accuracy of $[Co^{3+}\ \mathrm{HS}]_{\mathrm{crit}}$ of ±1.5% for the samples with $\langle s \rangle = 9.5$ nm and therefore the number of Co^{3+} ions, which are coupled at $[Co^{3+}\ \mathrm{HS}]$=$[Co^{3+}\ \mathrm{HS}]_{\mathrm{crit}}$ is approximately 18.9% $^{+0.3\%}_{-1.2\%}$. The probability for two of the six next-nearest neighbours being in the HS state is only 3.9%, which is not enough for long-range order, as long-range order is only established, if each Co^{3+} in the HS state is coupled to two other Co^{3+} in the HS state.

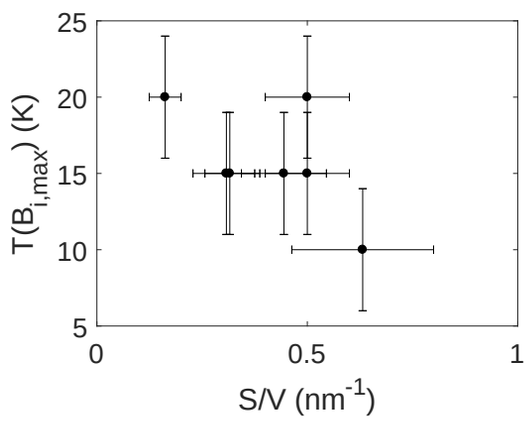

Figure 4.8: The temperature at which the fitted value of B_{i} is maximum as a function of surface-to-volume ratio S/V.

The suggested mechanism above also corresponds to the observation of the inverse susceptibility (see inset Fig. 3.20): At high temperatures the inverse susceptibility (approximated here by $B/\langle m \rangle$) decreases linearly in a purely paramagnetic fashion, but with the slight modification of continuously varying $[Co^{3+}\ \mathrm{HS}]$. Below $T = T^* \approx 80$ K spin-spin correlations start to be stronger than the thermal energy, hence the susceptibility increases. As the temperature drops below $T = T(B_{\mathrm{i,max}})$, the $[Co^{3+}\ \mathrm{HS}]$ becomes so low that the distance between spins controls susceptibility, which increases more slowly at

low temperatures. As Co^{2+} cannot couple to Co^{3+} due to the spin blockade effect, it is not expected to contribute to B_i or B_{irr}.

In summary, the combination of SQUID and NEXAFS analysis leads to the following interpretation of $LaCoO_3$ NP behaviour: Increasing the surface-to-volume ratio most likely results in complete coverage of the surface with hydroxides from adsorbed water. This is assumed to lead to an increase of the unit-cell volume and the Co-O bond length $d_{Co\text{-}O}$ with respect to bulk $LaCoO_3$. The increase of $d_{Co\text{-}O}$ decreases the crystal-field splitting and hence results in a higher concentration of Co^{3+} HS, which leads to a magnetic moment, that linearly increases with S/V. As the Co^{3+} HS concentration remains below the percolation threshold for all temperatures $T \leq T_C$, no ferromagnetism can be expected. At $T \geq T_C$, no ferromagnetism can be expected either, even if the [HS] concentration exceeds the percolation threshold. $LaCoO_3$ NPs show paramagnetic behaviour with very weak correlations between Co^{3+} spins.

4.3.2 Reduction of T_C in $La_{1-x}Sr_xMnO_3$

The reduction of T_C of $La_{1-x}Sr_xMnO_3$ NPs in comparison to bulk material is very likely related to the observed structural changes in NP occurring with decreasing particle size.

As mentioned in the introduction, the ferromagnetic exchange in $La_{1-x}Sr_xMnO_3$ is mediated by the double-exchange mechanism between Mn^{3+} and Mn^{4+} via O orbitals. Hence, overlap between Mn $3d$ and O $2p$ orbitals is essential for ferromagnetic exchange. The degree of pd hybridization therefore strongly depends on structural properties. For example, the one-electron band width ω is roughly proportional to $\frac{\cos(\theta)}{d^{3.5}}$(Ref. [269]). Fig. 4.9 shows the relative change of T_C between NPs and bulk material for the same Sr concentration x, i.e. $\frac{\Delta T_{C,NP}}{T_{C,b}}$, and the relative change of ω, i.e., $\frac{\Delta\omega}{\omega_b}$, as a function of S/V. Similarly to the structural properties discussed above, the same size-dependent behaviour $\partial(\Delta T_C)/\partial(S/V)$ is assumed for all samples with $0.3 \leq x \leq 0.5$. Except for the sample with $S/V = 0.3$ ($\langle x\rangle_{XRD} = 20$ nm), the Sr concentration is very similar with $0.37\pm0.02 \leq x \leq 0.39\pm0.02$ and T_C is expected to be equally 357 K for all three samples. Therefore, it is very likely that the clear difference in relative reduction of T_C shown in Fig. 4.9(a) is entirely due to NP size. Despite the limited experimental accuracy, the trend is quite clear: the reduction of T_C goes in line with the decrease of ω, i.e., the increase of d and the decrease of θ [270]. However, Fig. 4.9 reveals that the decrease of T_C with decreasing band width is two times larger than expected from this model.

This finding suggests the presence of an intrinsic size effect, as the size of a 3D Heisenberg ferromagnet approaches the spin-spin correlation length ξ at T_C, which can suppress T_C to lower values. In $La_{0.67}Ca_{0.3}MnO_3$ thin films, the T_C reduction was found to scale as $1 - \frac{T_{C,n}}{T_{C,b}} \propto s^{-\zeta}$ with $\zeta = 1$ (Ref. [5]). Herein, a 10% reduction in T_C is observed for a film thickness of 20 nm due to the finite-size effect, which roughly corresponds to the reduction in T_C left to account for beyond the reduction due to less effective double exchange. Unfortunately, the small number of data points and limited accuracy do not allow a fit to the finite-size effect. Nevertheless, a combination of reduction of T_C due to reduced double exchange and due to the finite-size effect is probably responsible for the T_C reduction in nanoparticles. This is in contrast to the findings of Refs. [124,

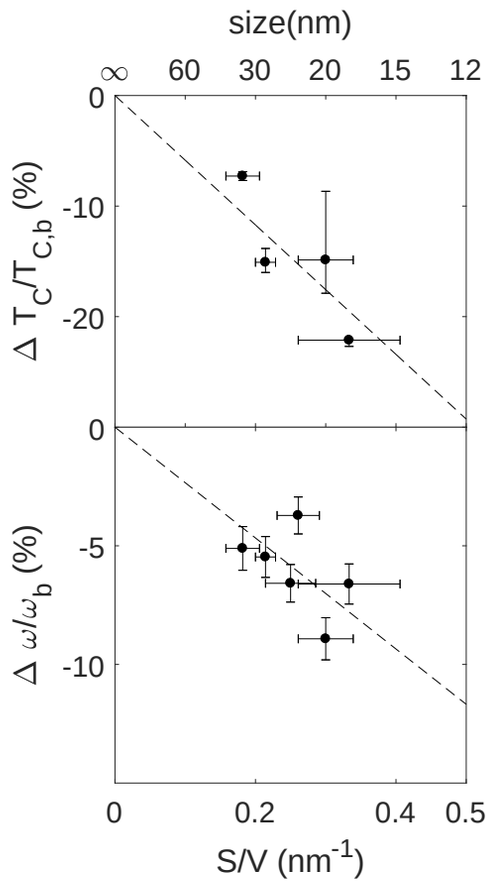

Figure 4.9: Relative change $\Delta T_C/T_{C,b}$ and the one-electron bandwidth $\Delta\omega/\omega_b$ for NP samples compared to T_C of bulk $La_{1-x}Sr_xMnO_3$ ($T_{C,b}$) and ω_b of bulk with the same Sr concentration x, respectively, vs size $\langle s\rangle_{XRD}$ (upper scale) and S/V (lower scale). The dashed lines are extrapolations to the bulk, i.e., $\Delta T_C = 0$, $\Delta\omega = 0$, and $S/V = 0$.

159], both of which attribute the reduction of T_C to the finite-size effect alone, without taking into consideration the additional weakening of double-exchange coupling based on size-induced lattice expansion.

However, it is also possible that the anomalous strain sensitivity of $La_{1-x}Sr_xMnO_3$ due to electron-phonon coupling [149] is responsible for a T_C reduction larger than predicted by double-exchange theory. Ref. [271] found that, in CMR materials, a biaxial strain of 1% could lead to a reduction of 10% in T_C, which is anomalously high due to electron-phonon coupling to the Jahn-Teller phonon. (The biaxial strain in the case of NPs is $\leq 0.04\%$.) Their calculations predict $\alpha = 1/T_C\ dT_C/d\varepsilon_B \approx 20$ with ε_B being the compressive strain $\varepsilon_B = 1/3(\varepsilon_{xx} + \varepsilon_{yy} + \varepsilon_{zz})$. The rhombohedral structure of the NP in this work does not support Jahn-Teller distortions, hence they can only be present locally or dynamically on a fast scale. With $\varepsilon_{xx} = \varepsilon_{yy} = \Delta a$ and $\varepsilon_{zz} = \Delta c$, the values $-0.3 \leq \alpha \leq -0.1$ are obtained for $0.18 \leq S/V \leq 0.33$. The direct comparison with Ref. [271] is possible because the

theoretical prediction does not differentiate between tension and compression. Since the experimental α is three orders of magnitude smaller than the theoretical α, this effect is thought to be irrelevant to the present case. This agrees with the observation that manganites with wide band gaps are well described by the double-exchange model alone [41], since the delocalization of e_g electrons via double-exchange is acting against the JT distortion by lifting the difference between Mn^{3+} and Mn^{4+}.

In summary, reducing the size of $La_{1-x}Sr_xMnO_3$ down to 20-30 nm leads to a significant lowering of T_C by up to 22% with respect to bulk crystals. The T_C reduction is most likely related to structural changes (d, θ) resulting in a negative effect on the double-exchange coupling. T_C is probably lowered additionally due to the finite size effect. The lattice deformation itself, particularly the increase of d and reduction of θ with decreasing $\langle s \rangle$, seems to be inherently correlated with the particle size $\langle s \rangle$ or S/V [270].

5 Conclusion and Outlook

In this thesis, microemulsion synthesis has been used to prepare nanoparticles (NPs) of transition-metal oxides, i.e. $LaCoO_3$ and $La_{1-x}Sr_xMnO_3$. This synthesis route yields NPs of different sizes, controlled by the water-to-surfactant ratio, while keeping the calcination temperature fixed. Therefore, the NPs of different sizes have comparable oxygen stoichiometry and crystal quality. Previous studies, on the other hand, often used calcination temperature to control the NP size, with the disadvantage that the structure of the NP may depend on that temperature due to the sensitivity of oxides to the calcination temperature.

Unfortunately, microemulsion synthesis has a number of disadvantages, limiting its use in oxide nanoparticle synthesis: most importantly, the low yield prevents certain analysis techniques, or limits the number of measurements that can be done on one batch. Additionally, microemulsion synthesis only allows a limited range of sizes, provided the calcination temperature is constant for all batches, which makes it difficult to analyse trends. One of the largest limitations, however, arises from the difficulty to control the chemical composition of nanoparticles synthesized in microemulsions: for $La_{1-x}Sr_xMnO_3$, despite the same nominal Sr concentration ($x = 0.25$) in the precursor solutions, the resultant $La_{1-x}Sr_xMnO_3$ batches varied in Sr concentration in the range $0.34 \leq x \leq 0.47$. For $LaCoO_3$, it was difficult to get the correct excess of La in the precursor solution to avoid the formation of both Co_3O_4 and La_2O_3. Therefore only seven out of seventeen batches could be used for analysis.

Detailed structural analysis has shown that the investigated perovskite oxide nanoparticles tend towards elongated atomic bonds and enlarged unit cells as the surface-to-volume ratio S/V increases. Although the mechanism behind this increase has not been fully established, surface adsorbates — in particular –OH — are probably responsible for the structural modifications. The extent of structural change seems to be related to the adsorption efficiency, which is a function of both valence and chemistry of the transition-metal ions. As S/V increases, the relative mass concentration of adsorbates is likely to increase. Therefore the lattice expansion scales linearly with S/V. However, this thesis shows that the size-dependent unit-cell expansion in $La_{1-x}Sr_xMnO_3$ is three times larger than in $LaCoO_3$ NPs with the same particle size. Most likely, this discrepancy is due to the different bond strength between –OH and Mn^{3+}/Mn^{4+} or Co^{3+}, respectively. However, the full understanding of this mechanism requires additional research.

Further studies are suggested on oxides of different crystal structure to determine the applicability of the unit-cell expansion effect, and to understand the mechanism in more detail. Additionally, the mechanism could be verified by controlled coating of NPs and analysis of the coating-dependent structural modifications. For example, transition-metal oxide NPs can be encased in SiO_2 shells, or fully covered by organic molecules, after

calcination. This could lead to different structural modifications, depending on whether the core-shell interface is negatively or positively charged or neutral.

In $LaCoO_3$, the elongation of the Co-O bond length results in a decrease of crystal field splitting and stabilizes the Co^{3+} HS state. As Co^{3+} HS is magnetic with $S = 2$, the specific magnetic moment can be controlled by the surface-to-volume ratio via the Co-O bond length. For stoichiometric, single-phase $LaCoO_3$ nanoparticles, the Co^{3+} HS concentration is too low at $\langle s \rangle \geq 9.5$ nm to develop long-range ferromagnetic order. In contrast to previous studies, the Co^{3+} HS ions are most likely homogeneously distributed throughout the nanoparticles and show purely paramagnetic behaviour. In particular, no evidence for magnetic phase separation into regions of ferromagnetic or superparamagnetic clusters (with the concentration of Co^{3+} HS exceeding 30%) and dilute, isolated Co^{3+} HS moments could be found. The weak correlations between the Co^{3+} HS spins can be modelled by a temperature-dependent internal field.

Since the bond-length modification is most likely achieved by surface adsorbates, artificial surface adsorption might be able to increase the Co-O bond length until the Co^{3+} HS concentration is high enough for long-range ferromagnetic order. Controlling the magnetic moment by the nature and amount of surface adsorbates could be an interesting prospect for future work.

The situation is slightly more complex in the ferromagnetic $La_{1-x}Sr_xMnO_3$ material with a mixture of Mn^{3+} and Mn^{4+}. The ratio of the concentration of two valence states is determined mainly by the Sr concentration x, which in the microemulsion process is not under control. Therefore, a scaling approach was employed to disentangle the effects of particle size and x on the magnetic properties. In this material, the elongation of the Mn-O bond length and the reduction of the Mn-O-Mn bond angle in the NPs with respect to the bulk result in a weakening of the double-exchange mechanism, reducing T_C. As the material orders ferromagnetically, the intrinsic size effect plays an additional role by lowering T_C further. As both effects depend on S/V, the relative decrease of T_C can be directly controlled by modifying S/V.

Acknowledgements

I am deeply grateful to the Hector-Fellow-Academy for offering me this extraordinary chance at completing a PhD project of my own design: The more than generous funding and support of the Hector Fellow Academy enabled me to conduct research into the fascinating topic of transition metal perovskite nanoparticles.

First and foremost I would like to extend my thanks to Professor von Löhneysen, who supported my project proposal to the Hector Fellow Academy and allowed me to pursue my thesis at the Institute for Solid State Physics (IFP). His keen interest in my work and his valuable support in theoretical and experimental matters made this thesis possible. Professor von Löhneysen was also the one to bring Professor Annie Powell on board. I am greatly indebted to her and her research group at the Institute of Nanotechnology (INT), with former and present co-workers Masooma Ibrahim, Nicolas Leblanc, and Amer Baniodeh, who helped me set up my experiments and offered advice any time I was hitting a dead end.

At this point, I would like to acknowledge the high-quality synthesis work done by Illia Timashkov, and his funding by the Karlsruhe House of Young Scientists. His commitment and experimental skill were a very much appreciated support in developing the $LaCoO_3$ microemulsion synthesis. I would also like to thank Illia's successor, Tianhao Zhang.

Although chemical synthesis proved to be a major challenge in this project, the characterization and interpretation of experimental results were equally demanding. My gratitude goes in particular to Dirk Fuchs for his introduction to XRD and SQUID equipment, frequent discussions and valuable input to both our paper and this thesis, and his tireless effort in helping me understand these complicated materials: I could not have wished for a more engaged supervisor. In terms of experimental work, I also have to thank a number of people who conducted and analysed experiments for me: Michael Merz, who was kind enough to provide Rietveld refinement on a series of nanoparticles and was always available for discussions, Meng-Jie Huang and the Schuppler research group for allocating beam time to my experiments, measuring and fitting NEXAFS and XMCD data, and Dorothée Vinga Szabó, Houari Amari and Christian Kübel at the INT for beautiful and informative transmission electron microscopy images, as well as EDX and EELS analyses. In this regard, I also thank Simone Dehm for graciously allowing me the use of the INT's scanning electron microscopy.

Having acknowledged technical collaboration, I would like to point out that without all the personal support this project would not have come to fruition. Firstly, I would like to thank all members of the IFP, who were welcoming, supportive and friendly at all times, but most of all my fellow PhD students. Without their friendship my time in Karlsruhe would have been a lot more lonely and a lot less enjoyable. Last but absolutely not least I want to thank my family and most importantly my partner for believing in me and supporting me at all times.

Bibliography

[1]D. Fuchs, C. Pinta, T. Schwarz, P. Schweiss, P. Nagel, S. Schuppler, R. Schneider, M. Merz, G. Roth, and H. v. Löhneysen, "Ferromagnetic order in epitaxially strained $LaCoO_3$ thin films", Physical Review B **75**, 144402 (2007).

[2]R. M. Hazen, R. T. Downs, A. P. Jones, and L. Kah, "Carbon mineralogy and crystal chemistry", Reviews in Mineralogy and Geochemistry **75**, 7–46 (2013).

[3]J. M. D. Coey, *Magnetism and Magnetic Materials* (Cambridge University Press, Cambridge, 2009).

[4]M. Fisher and M. Barber, "Scaling Theory for Finite-Size Effects in the Critical Region", Physical Revue Letters **28**, 1516–1519 (1972).

[5]M. Ziese, H. C. Semmelhack, K. H. Han, S. P. Sena, and H. J. Blythe, "Thickness dependent magnetic and magnetotransport properties of strain-relaxed $La_{0.7}Ca_{0.3}MnO_3$ films", Journal of Applied Physics **91**, 9930–9936 (2002).

[6]D. Fuchs, T. Schwarz, O. Morán, P. Schweiss, and R. Schneider, "Finite-size shift of the Curie temperature of ferromagnetic lanthanum cobaltite thin films", Physical Review B **71**, 6–9 (2005).

[7]X. Batlle and A. Labarta, "Finite-size effects in fine particles: magnetic and transport properties", Journal of Physics D: Applied Physics **35**, R15–R42 (2002).

[8]O. Petracic, "Superparamagnetic nanoparticle ensembles", Superlattices and microstructures **47**, 569–578 (2010).

[9]P. P. Rodenbough, C. Zheng, Y. Liu, C. Hui, Y. Xia, Z. Ran, Y. Hu, and S.-W. Chan, "Lattice Expansion in Metal Oxide Nanoparticles: MgO, Co_3O_4 & Fe_3O_4", Journal of the American Ceramic Society, 384–392.

[10]D. Vollath, *Nanomaterials - An Introduction to Synthesis, Properties and Applications* (Wiley-VCH, Weinheim, 2008), p. 352.

[11]A. Rusanov, "Surface thermodynamics revisited", Surface Science Reports **58**, 111–239 (2005).

[12]F. D. Fischer, T. Waitz, D. Vollath, and N. K. Simha, "On the role of surface energy and surface stress in phase-transforming nanoparticles", Progress in Materials Science **53**, 481–527 (2008).

[13]Z. Cai, Y. Kuru, J. W. Han, Y. Chen, and B. Yildiz, "Surface electronic structure transitions at high temperature on perovskite oxides: the case of strained $La_{0.8}Sr_{0.2}CoO_3$ thin films.", Journal of the American Chemical Society **133**, 17696–17704 (2011).

[14]H. Jalili, J. Han, and Y. Kuru, "New insights into the strain coupling to surface chemistry, electronic structure, and reactivity of $La_{0.7}Sr_{0.3}MnO_3$ ", The Journal of Physical Chemistry Letters **3**, 801–807 (2011).

[15]U. Aschauer, N. Vonrüti, and N. A. Spaldin, "Effect of epitaxial strain on cation and anion vacancy formation in MnO", Physical Review B **92**, 1–5 (2015).

[16]J. Ma, Y. Zhang, L. Wu, C. Song, Q. Zhang, J. Zhang, J. Ma, and C.-W. Nan, "Strain-induced modulation of oxygen vacancies and magnetic properties in $La_{0.5}Sr_{0.5}MnO_3$ thin films", MRS Communications **69**, 354–359 (2016).

[17]W. Donner, C. Chen, M. Liu, A. J. Jacobson, Y. L. Lee, M. Gadre, and D. Morgan, "Epitaxial strain-induced chemical ordering in $La_{0.5}Sr_{0.5}CoO_{3-\delta}$ Films on $SrTiO_3$", Chemistry of Materials **23**, 984–988 (2011).

[18]J. Coey, "Noncollinear spin arrangement in ultrafine ferrimagnetic crystallites", Physical Review Letters **27**, 1140–1142 (1971).

[19]S. Roy, I. Dubenko, D. D. Edorh, and N. Ali, "Size induced variations in structural and magnetic properties of double exchange $La_{0.8}Sr_{0.2}MnO_{3-\delta}$ nano-ferromagnet", Journal of Applied Physics **96**, 1202–1208 (2004).

[20]T. Tajiri, S. Saisho, M. Mito, H. Deguchi, K. Konishi, and A. Kohno, "Size Dependence of Crystal Structure and Magnetic Properties of NiO Nanoparticles in Mesoporous Silica", The Journal of Physical Chemistry C **119**, 1194–1200 (2015).

[21]S. N. Khanna and S. Linderoth, "Magnetic behavior of clusters of ferromagnetic transition metals", Physical Review Letters **67**, 742–745 (1991).

[22]B. Reddy, S. N. Khanna, and B. Dunlap, "Giant Magnetic moments in 4d clusters", Physical Review Letters **70**, 3323–3326 (1993).

[23]F. Liu, M. R. Press, S. Khanna, and P. Jena, "Magnetism and local order: Ab initio tight-binding theory", Physical Review B **39**, 6914–6924 (1989).

[24]M. R. Ranade, A. Navrotsky, H. Z. Zhang, J. F. Banfield, S. H. Elder, A. Zaban, P. H. Borse, S. K. Kulkarni, G. S. Doran, and H. J. Whitfield, "Energetics of nanocrystalline TiO_2", Proceedings of the National Academy of Sciences **99**, 6476–6481 (2002).

[25]A. Navrotsky, "Energetics of nanoparticle oxides: interplay between surface energy and polymorphism", Geochemical Transactions **4**, 34–37 (2003).

[26]J. F. Mitchell, D. N. Argyriou, C. D. Potter, D. G. Hinks, J. D. Jorgensen, and S. D. Bader, "Structural phase diagram of $La_{1-x}Sr_xMnO_{3+\delta}$: Relationship to magnetic and transport properties", Physical Revue B **54**, 6172–6183 (1996).

[27]J. Töpfer and J. B. Goodenough, "LaMnO(3+d) Revisited", Journal of Solid State Chemistry **130**, 117–128 (1997).

[28]L. Chen, P. Fleming, V. Morris, J. D. Holmes, and M. A. Morris, "Size-related lattice parameter changes and surface defects in ceria nanocrystals", Journal of Physical Chemistry C **114**, 12909–12919 (2010).

[29]P. M. Diehm, P. Ágoston, and K. Albe, "Size-dependant lattice expansion in Nanoparticles: Reality or Anomaly?", ChemPhysChem **13**, 2443–2454 (2012).

[30]S. Stankov, Y. Z. Yue, M. Miglierini, B. Sepiol, I. Sergueev, A. I. Chumakov, L. Hu, P. Svec, and R. Rüffer, "Vibrational properties of nanograins and interfaces in nanocrystalline materials", Physical Review Letters **100**, 11–14 (2008).

[31]P. Ayyub, V. R. Palkar, S. Chattopadhyay, and M. Multani, "Effect of crystal size reduction on lattice symmetry and cooperative properties", Physical Review B **51**, 6135–6138 (1995).

[32]J. Stöhr and H. C. Siegmann, *Magnetism: from fundamentals to nanoscale mechanics* (Springer, Berlin Heidelberg, 2006).

[33]R. von Helmholt, J. Wecker, B. Holzapfel, L. Schultz, and K. Samwer, "Giant negative magnetoresistance in perovskite-like $La_{2/3}Ba_{1/3}MnO_x$ ferromagnetic films", Physical Review Letters **71**, 2331–2333 (1993).

[34]S. Vasseur, E. Duguet, J. Portier, G. Goglio, S. Mornet, E. Hadová, K. Knížek, M. Maryško, P. Veverka, and E. Pollert, "Lanthanum manganese perovskite nanoparticles as possible in vivo mediators for magnetic hyperthermia", Journal of Magnetism and Magnetic Materials **302**, 315–320 (2006).

[35]E. Pollert, K. Knížek, M. Maryško, P. Kašpar, S. Vasseur, and E. Duguet, "New -tuned magnetic nanoparticles for self-controlled hyperthermia", Journal of Magnetism and Magnetic Materials **316**, 122–125 (2007).

[36]N. D. Lipham, G. M. Tsoi, and L. E. Wenger, "Synthesis and Characterization of Sr-Doped Lanthanum Manganite Nanoparticles", IEEE Transactions on Magnetics **43**, 3088–3090 (2007).

[37]N. X. Phuc, N. Tuan, N. C. Thuan, V. Tuan, and L. V. Hong, "Magnetic Nanoparticles as Smart Heating Mediator for Hyperthermia and Sorbent Regeneration", Advanced Materials Research **55-57**, 27–32 (2008).

[38]O. Kaman, E. Pollert, P. Veverka, M. Veverka, E. Hadová, K. Knízek, M. Marysko, P. Kaspar, M. Klementová, V. Grünwaldová, S. Vasseur, R. Epherre, S. Mornet, G. Goglio, and E. Duguet, "Silica encapsulated manganese perovskite nanoparticles for magnetically induced hyperthermia without the risk of overheating.", Nanotechnology **20**, 275610 (2009).

[39]E. Natividad, M. Castro, G. Goglio, I. Andreu, R. Epherre, E. Duguet, and A. Mediano, "New insights into the heating mechanisms and self-regulating abilities of manganite perovskite nanoparticles suitable for magnetic fluid hyperthermiA.", Nanoscale **4**, 3954–3962 (2012).

[40]A.-M. Haghiri-Gosnet and J.-P. Renard, "CMR manganites: physics, thin films and devices", Journal of Physics D: Applied Physics **36**, R127–R150 (2003).

[41]K. Dörr, "Ferromagnetic manganites: spin-polarized conduction versus competing interactions", Journal of Physics D: Applied Physics **39**, R125–R150 (2006).

[42]J. Mastin, M. A. Einarsrud, and T. Grande, "Structural and thermal properties of $La_{1-x}Sr_xCoO_{3-\delta}$ ", Chemistry of Materials **18**, 6047–6053 (2006).

[43]V. M. Goldschmidt, *Geochemistry* (Oxford: Clarendon Press, 1958).

[44]Y. Lee and B. N. Harmon, "Rhombohedral distortion effects on electronic structure of $LaCoO_3$", Journal of Applied Physics **113**, 17E145 (2013).

[45]D. P. Belanger, T. Keiber, F. Bridges, A. M. Durand, A. Mehta, H. Zheng, J. F. Mitchell, and V. Borzenets, "Structure and magnetism in $LaCoO_3$", Journal of Physics: Condensed Matter **28**, 025602 (2015).

[46]R. Schmidt, J. Wu, C. Leighton, and I. Terry, "Dielectric response to the low-temperature magnetic defect structure and spin state transition in polycrystalline $LaCoO_3$", Physical Review B **79**, 125105 (2009).

[47]M. Merz, P. Nagel, C. Pinta, A. Samartsev, H. v. Löhneysen, M. Wissinger, S. Uebe, A. Assmann, D. Fuchs, and S. Schuppler, "X-ray absorption and magnetic circular dichroism of $LaCoO_3$, $La_{0.7}Ce_{0.3}CoO_3$, and $La_{0.7}Sr_{0.3}CoO_3$ films: Evidence for cobalt-valence-dependent magnetism", Physical Review B **82**, 174416 (2010).

[48]P. G. Radaelli and S.-W. Cheong, "Structural phenomena associated with the spin-state transition in $LaCoO_3$", Physical Review B **66**, 094408 (2002).

[49]M. Imada, A. Fujimori, and Y. Tokura, "Metal-insulator transitions", Reviews of Modern Physics **70**, 1039–1263 (1998).

[50]T. Kyômen, Y. Asaka, and M. Itoh, "Thermodynamical analysis of spin-state transitions in $LaCoO_3$: Negative energy of mixing to assist thermal excitation to the high-spin excited state", Physical Review B **71**, 024418 (2005).

[51]M. W. Haverkort, Z. Hu, J. C. Cezar, T. Burnus, H. Hartmann, M. Reuther, C. Zobel, T. Lorenz, A. Tanaka, N. B. Brookes, H. H. Hsieh, H. J. Lin, C. T. Chen, and L. H. Tjeng, "Spin state transition in $LaCoO_3$ studied using soft X-ray absorption spectroscopy and magnetic circular dichroism", Physical Review Letters **97**, 38–41 (2006).

[52]P. Ravindran, H. Fjellvåg, A. Kjekshus, P. Blaha, K. Schwarz, and J. Luitz, "Itinerant metamagnetism and possible spin transition in $LaCoO_3$ by temperature/hole doping", Journal of Applied Physics **91**, 291–303 (2002).

[53]M. Korotin, S. Ezhov, I. Solovyev, V. Anisimov, D. Khomskii, and G. A. Sawatzky, "Intermediate-spin state and properties of $LaCoO_3$", Physical Review B **54**, 5309–5316 (1996).

[54]C. J. Benedict, A. Rao, G. Sanjeev, G. Okram, and P. Babu, "A systematic study on the effect of electron beam irradiation on structural, electrical, thermo-electric power and magnetic property of $LaCoO_3$", Journal of Magnetism and Magnetic Materials **397**, 145–151 (2016).

[55]L. Qiao, J. H. Jang, D. J. Singh, Z. Gai, H. Xiao, A. Mehta, R. K. Vasudevan, A. Tselev, Z. Feng, H. Zhou, S. Li, W. Prellier, X. Zu, Z. Liu, A. Borisevich, A. P. Baddorf, and M. D. Biegalski, "Dimensionality Controlled Octahedral Symmetry-Mismatch and Functionalities in Epitaxial $LaCoO_3/SrTiO_3$ Heterostructures", Nano Letters **15**, 4677–4684 (2015).

[56]N. Ivanova, S. G. Ovchinnikov, M. Korshunov, I. Eremin, and N. Kazak, "Specific features of spin, charge, and orbital ordering in cobaltites", Uspekhi Fizicheskih Nauk **179**, 837 (2009).

[57]K. Asai, O. Yokokura, and M. Suzuki, "Pressure Dependence of the 100 K Spin-State Transition in $LaCoO_3$", Journal of the Physical Society of Japan **66**, 967–970 (1997).

[58]M. Magnuson, S. M. Butorin, C. Sathe, J. Nordgren, and P. Ravindran, "Spin transition in $LaCoO_3$ investigated by resonant soft X-ray emission spectroscopy", Europhysics Letters **68**, 289 (2004).

[59]G. Vankó, J.-P. Rueff, A. Mattila, Z. Németh, and A. Shukla, "Temperature- and pressure-induced spin-state transitions in $LaCoO_3$", Physical Review B **73**, 024424 (2006).

[60]D. P. Kozlenko, N. O. Golosova, Z. Jirák, L. S. Dubrovinsky, B. N. Savenko, M. G. Tucker, Y. Le Godec, and V. P. Glazkov, "Temperature- and pressure-driven spin-state transitions in $LaCoO_3$", Physical Review B **75**, 064422 (2007).

[61]S. G. Ovchinnikov, Y. S. Orlov, and V. A. Dudnikov, "Temperature and field dependent electronic structure and magnetic properties of $LaCoO_3$ and $GdCoO_3$", Journal of Magnetism and Magnetic Materials **324**, 3584–3587 (2012).

[62]A. Laref, S. Laref, and S. Bin-Omran, "Electronic structure, X-ray absorption, and optical spectroscopy of $LaCoO_3$ in the ground-state and excited-states", Journal of Computational Chemistry **33**, 673–684 (2012).

[63]M. Karolak, M. Izquierdo, S. Molodtsov, and A. Lichtenstein, "Correlation-Driven Charge and Spin Fluctuations in $LaCoO_3$", Physical Review Letters **115**, 046401 (2015).

[64]M. Zhuang, W. Zhang, and N. Ming, "Competition of various spin states in $LaCoO_3$", Physical Review B **57**, 10705–10710 (1998).

[65]S. Noguchi, S. Kawamata, K. Okuda, H. Nojiri, and M. Motokawa, "Evidence for the excited triplet of Co^{3+} in $LaCoO_3$", Physical Review B **66**, 944041–944045 (2002).

[66]K. Knížek, Z. Jirák, J. Hejtmánek, and P. Novák, "Character of the excited state of the Co3+ ion in $LaCoO_3$", Journal of Physics Condensed Matter **18**, 3285–3297 (2006).

[67]Z. Ropka and R. J. Radwanski, "^{5}D origin of the excited triplet in $LaCoO_3$", Physical Review B **67**, 172401 (2003).

[68]A. Podlesnyak, S. Streule, J. Mesot, M. Medarde, E. Pomjakushina, K. Conder, A. Tanaka, M. W. Haverkort, and D. I. Khomskii, "Spin-state transition in $LaCoO_3$: Direct neutron spectroscopic evidence of excited magnetic states", Physical Review Letters **97**, 247208 (2006).

[69]C. Pinta, D. Fuchs, M. Merz, M. Wissinger, E. Arac, H. v. Löhneysen, A. Samartsev, P. Nagel, and S. Schuppler, "Suppression of spin-state transition in epitaxially strained $LaCoO_3$", Physical Review B **78**, 174402 (2008).

[70]Y. Jiang, F. Bridges, N. Sundaram, D. P. Belanger, I. E. Anderson, J. F. Mitchell, and H. Zheng, "Study of the local distortions of the perovskite system La1-xSrxCoO3 ($0 \leq x \leq 0.35$) using the extended x-ray absorption fine structure technique", Physical Review B **80**, 144423 (2009).

[71]M Rotter, Z.-S. Wang, A. T. Boothroyd, D Prabhakaran, A Tanaka, and M Doerr, "Mechanism of spin crossover in LaCoO3 resolved by shape magnetostriction in pulsed magnetic fields.", Scientific reports **4**, 7003 (2014).

[72]M. Ghiasi, M. U. Delgado-Jaime, A. Malekzadeh, R.-P. Wang, P. S. Miedema, M. Beye, and F. M. F. de Groot, "Mn and Co Charge and Spin Evolutions in $LaMn_{1-x}Co_xO_3$ Nanoparticles", The Journal of Physical Chemistry C **120**, 8167–8174 (2016).

[73]T. Ishimoto, Y. Ito, T. Tada, R. Oike, T. Nakamura, K. Amezawa, and M. Koyama, "Theoretical study on temperature effect of electronic structure and spin state in $LaCoO_3$ by using density functional theory", Solid State Ionics **285**, 195–201 (2016).

[74]O. Haas, R. P.W. J. Struis, and J. M. McBreen, "Synchrotron X-ray absorption of $LaCoO_3$ perovskite", Journal of Solid State Chemistry **177**, 1000–1010 (2004).

[75]S. Wilke, "Bond percolation threshold in the simple cubic structure", Physics Letters **96A**, 344–346 (1983).

[76]I. Fita, V. Markovich, D. Mogilyansky, R. Puzniak, A. Wisniewski, L. Titelman, L. Vradman, M. Herskowitz, V. N. Varyukhin, and G. Gorodetsky, "Size- and pressure-controlled ferromagnetism in $LaCoO_3$ nanoparticles", Physical Review B **77**, 224421 (2008).

[77]I. Fita, D. Mogilyansky, V. Markovich, R. Puzniak, A. Wisniewski, L. Titelman, L. Vradman, M. Herskowitz, V. N. Varyukhin, and G. Gorodetsky, "Pressure-induced suppression of ferromagnetic phase in $LaCoO_3$ nanoparticles", Journal of Non-Crystalline Solids **354**, 5204–5206 (2008).

[78]A. Kushima, S. Yip, and B. Yildiz, "Competing strain effects in reactivity of $LaCoO_3$ with oxygen", Physical Review B **82**, 115435 (2010).

[79]N. Biškup, J. Salafranca, V. Mehta, M. P. Oxley, Y. Suzuki, S. J. Pennycook, S. T. Pantelides, and M. Varela, "Insulating ferromagnetic $LaCoO_{3-\delta}$ films: A phase induced by ordering of oxygen vacancies", Physical Review Letters **112**, 087202 (2014).

[80]J. A. M. Van Roosmalen and E. H. P. Cordfunke, "A new defect model to describe the oxygen deficiency in perovskite-type oxides", Journal of Solid State Chemistry **93**, 212–219 (1991).

[81]M. A. Torija, M Sharma, M. R. Fitzsimmons, M Varela, and C Leighton, "Epitaxial $La_{0.5}Sr_{0.5}CoO_3$ thin films: Structure, magnetism, and transport", Journal of Applied Physics **104**, 23901 (2008).

[82]V. V. Sikolenko, E. V. Pomjakushina, and S. Y. Istomin, "Neutron diffraction studies of $La_{1-x}Sr_xCoO_3$ magnetic structure at x = 0.15 and 0.3", Journal of Magnetism and Magnetic Materials **258-259**, 300–301 (2003).

[83]J.-M. Liu and C. K. Ong, "The large magnetoresistance property of $La_{0.5}Sr_{0.5}CoO_{3-x}$ thin films prepared by pulsed laser deposition", Applied Physics Letters **73**, 1047 (1998).

[84]A. Mineshige, M. Kobune, S. Fujii, Z. Ogumi, M. Inaba, T. Yao, and K. Kikuchi, "Metal–insulator transition and crystal structure of $La_{1-x}Sr_xCoO_3$ as functions of Sr-content, temperature, and oxygen partial pressure", Journal of Solid State Chemistry **142**, 374–381 (1999).

[85]G. Prokhorov, G. G. Kaminsky, I. I. Kravchenko, and Y. P. Lee, "Transport properties of $La_{1-x}Sr_xCoO_{3-\delta}$ films ($0.15 \leq x \leq 0.5$)", Physica B: Condensed Matter **324**, 205–216 (2002).

[86]S. Madhukar, S. Aggarwal, A. M. Dhote, R. Ramesh, A. Krishnan, D. Keeble, and E. Poindexter, "Effect of oxygen stoichiometry on the electrical properties of $La_{0.5}Sr_{0.5}CoO_3$ electrodes", Journal of Applied Physics **81**, 3543 (1997).

[87]D. Baskar and S. B. Adler, "High Temperature Magnetic Properties of Sr-Doped Lanthanum Cobalt Oxide $La_{1-x}Sr_xCoO_{3-\delta}$ ", Chemistry of Materials **136**, 2624–2628 (2008).

[88]J. Prado-Gonjal, J. Gutiérrez-Seijas, I. H. Ansorregui, E. Morán, I. Terry, and R. Schmidt, "The role of defects in microwave and conventionally synthesized $LaCoO_3$ perovskite", Journal of the European Ceramic Society **36**, 1197–1206 (2016).

[89]. Макшина, Жилинская, Абукаис и. Романовский, "валентное и координационное состояния атомов кобальта в массивных и нанесенных кобальтатах лантана", Вестник Московского Университета **2**, 9–11 (2007).

[90]E. Makshina, E. Zhilinskaya, S. Siffert, G. Mazo, A. Aboukaïs, W. Grünert, and B. Romanovsky, "Nanostructured lanthanum cobaltate: oxidation and coordination states of Co atoms", Journal of Experimental Nanoscience **5**, 427–437 (2010).

[91]J. Androulakis, N. Katsarakis, and J. Giapintzakis, "Ferromagnetic and antiferromagnetic interactions in lanthanum cobalt oxide at low temperatures", Physical Review B **64**, 174401 (2001).

[92]W. S. Choi, J. H. Kwon, H. Jeen, J. E. Hamann-Borrero, A. Radi, S. MacKe, R. Sutarto, F. He, G. A. Sawatzky, V. Hinkov, M. Kim, and H. N. Lee, "Strain-induced spin states in atomically ordered cobaltites", Nano Letters **12**, 4966–4970 (2012).

[93]J.-H. Kwon, W. S. Choi, Y.-K. Kwon, R. Jung, J.-M. Zuo, H. N. Lee, and M. Kim, "Nanoscale Spin-State Ordering in $LaCoO_3$ Epitaxial Thin Films", Chemistry of Materials **26**, 2496–2501 (2014).

[94]D. Fuchs, E. Arac, C. Pinta, S. Schuppler, R. Schneider, and H. v. Löhneysen, "Tuning the magnetic properties of $LaCoO_3$ thin films by epitaxial strain", Physical Review B **77**, 014434 (2008).

[95]S. Zhou, L. Shi, J. Zhao, L. He, H. Yang, and S. Zhang, "Ferromagnetism in $LaCoO_3$ nanoparticles", Physical Review B **76**, 172407 (2007).

[96]S. Zhou, L. He, S. Zhou, Y. Guo, J. Zhao, and L. Shi, "Size-dependent structural and magnetic properties of $LaCoO_3$ nanoparticles", Journal of Physical Chemistry C **113**, 13522–13526 (2009).

[97]Q. Wei, T. Zhang, X. P. Wang, and Q. F. Fang, "Size effects on the magnetic properties of $LaCoO_3$ nanoparticles", The European Physical Journal Applied Physics **57**, 30401 (2012).

[98]S. Zhou, L. Shi, J. Zhao, H. Yang, and L. Chen, "Electron spin resonance study of bulk and nanosized $La_{0.875}Sr_{0.125}MnO_3$", Solid State Communications **142**, 634–638 (2007).

[99]A. M. Durand, D. P. Belanger, T. J. Hamil, F. Ye, S. Chi, J. A. Fernandez-Baca, C. H. Booth, Y. Abdollahian, and M. Bhat, "The unusual magnetism of nanoparticle $LaCoO_3$", Journal of Physics: Condensed Matter **27**, 176003 (2015).

[100]A. M. Durand, D. P. Belanger, C. H. Booth, F. Ye, S. Chi, J. A. Fernandez-Baca, and M. Bhat, "Magnetism and phase transitions in $LaCoO_3$", Journal of Physics: Condensed Matter **25**, 382203 (2013).

[101]A. M. Durand, D. P. Belanger, F. Ye, S. Chi, J. A. Fernandez-Baca, C. H. Booth, and M. Bhat, "Magnetism in nanoparticle $LaCoO_3$", arXiv, 1311.0240 (2013).

[102]A. Harada, T. Taniyama, Y. Takeuchi, T. Sato, T. Kyomen, and M. Itoh, "Ferromagnetism at the surface of a $LaCoO_3$ single crystal observed using scanning SQUID microscopy", Physical Review B **75**, 184426 (2007).

[103]D. Fuchs, L. Dieterle, E. Arac, R. Eder, P. Adelmann, V. Eyert, T. Kopp, R. Schneider, D. Gerthsen, and H. v. Löhneysen, "Suppression of the ferromagnetic state in $LaCoO_3$ films by rhombohedral distortion", Physical Review B **79**, 024424 (2009).

[104]M. Popa and J. M. Calderon-Moreno, "Lanthanum cobaltite nanoparticles using the polymeric precursor method", Journal of the European Ceramic Society **29**, 2281–2287 (2009).

[105]I Fita, *Private communication*, 2016.

[106]L. Wachowski, S. Zieliński, and A. Burewicz, "Preparation, stability and oxygen stoichiometry in perovskite-type binary oxides", Acta Chimica Academiae Scientiarum Hungaricae **106**, 217–225 (1981).

[107]J. Rivas, L. E. Hueso, A. Fondado, F. Rivadulla, and M. A. López-Quintela, "Low field magnetoresistance effects in fine particles of $La_{0.67}Ca_{0.33}MnO_3$ perovskites", Journal of Magnetism and Magnetic Materials **221**, 57–62 (2000).

[108]J. Hu, H. Hao, C. Chen, D. Yang, and X. Hu, "Thermogravimetric study on perovskite-like oxygen permeation ceramic membranes", Journal of Membrane Science **280**, 809–814 (2006).

[109]G. Goupil, T. Delahaye, G. Gauthier, B. Sala, and F. L. Joud, "Stability study of possible air electrode materials for proton conducting electrochemical cells", Solid State Ionics **209-210**, 36–42 (2012).

[110]A. Urushibara, Y. Moritomo, T. Arima, A. Asamitsu, G. Kido, and Y. Tokura, "Insulator-metal transition and giant magnetoresistance in $La_{1-x}Sr_xMnO_3$ ", Physical Review B **51**, 14103–14109 (1995).

[111]D. Louca and T Egami, "Lattice effect in the metal-insulator transition in CMR manganites", Physica B: Condensed Matter **241-243**, 842–844 (1998).

[112]T. Zhu, B. G. Shen, J. R. Sun, H. W. Zhao, and W. S. Zhan, "Surface spin-glass behavior in $La_{2/3}Sr_{1/3}MnO_3$ nanoparticles", Applied Physics Letters **78**, 3863–3865 (2001).

[113]A. Dutta, N. Gayathri, and R. Ranganathan, "Effect of particle size on the magnetic and transport properties of $La_{0.875}Sr_{0.125}MnO_3$", Physical Review B **68**, 054432 (2003).

[114]Y. Koksharov, V. N. Nikiforov, V. D. Kuznetsov, and G. B. Khomutov, "Magnetic resonance properties of $La_{0.8}Sr_{0.2}MnO_3$ small particles", Microelectronic Engineering **81**, 371–377 (2005).

[115]V. Krivoruchko, T. Konstantinova, A. Mazur, A. Prokhorov, and V. Varyukhin, "Magnetic resonances spectroscopy of nanosize particles $La_{0.7}Sr_{0.3}MnO_3$ ", Journal of Magnetism and Magnetic Materials **300**, e122–e125 (2006).

[116]C. Vázquez-Vázquez and M Arturo López-Quintela, "Solvothermal synthesis and characterisation of $La_{1-x}A_xMnO_3$ nanoparticles", Journal of Solid State Chemistry **179**, 3229–3237 (2006).

[117]P Dutta, P Dey, and T. K. Natha, "Effect of nanometric grain size on room temperature magnetoimpedance, magnetoresistance, and magnetic properties of $La_{0.7}Sr_{0.3}MnO_3$ nanoparticles", Journal of Applied Physics **102**, 73906 (2007).

[118]V. Dyakonov, A. Ślawska-Waniewska, J. Kazmierczak, K. Piotrowski, O. Iesenchuk, H. Szymczak, E. Zubov, S. Myronova, V. Pashchenko, A. Pashchenko, A. Shemjakov, V. Varyukhin, S. Prilipko, V. Mikhaylov, Z. Kravchenko, A. Szytuła, and W. Bazela, "Nanoparticle size effect on the magnetic and transport properties of $(La_{0.7}Sr_{0.3})_{0.9}Mn_{1.1}O_3$ manganites", Low Temperature Physics **35**, 568–576 (2009).

[119]J. Curiale, M. Granada, H. E. Troiani, R. D. Sánchez, A. G. Leyva, P. Levy, and K. Samwer, "Magnetic dead layer in ferromagnetic manganite nanoparticles", Applied Physics Letters **95**, 043106 (2009).

[120]M. H. Ehsani, P Kameli, M. E. Ghazi, F. S. Razavi, and M Taheri, "Tunable magnetic and magnetocaloric properties of $La_{0.6}Sr_{0.4}MnO_3$ nanoparticles", Journal of Applied Physics **114**, 223907 (2013).

[121]Y. W. Duan, X. L. Kou, and J. G. Li, "Size dependence of structure and magnetic properties of $La_{0.7}Sr_{0.3}MnO_3$ nanoparticles", Physica B: Condensed Matter **355**, 250–254 (2005).

[122]R. Epherre, C. Pepin, N. Penin, E. Duguet, S. Mornet, E. Pollert, and G. Goglio, "Evidence of non-stoichiometry effects in nanometric manganite perovskites: influence on the magnetic ordering temperature", Journal of Materials Chemistry **21**, 14990 (2011).

[123]M. R. Cesário, D. A. Macedo, R. M.P. B. Oliveira, P. M. Pimentel, R. L. Moreira, and D. M. A. Melo, "The synthesis, thermal stability, crystal structure and spectroscopic study of $La_{0.8}Sr_{0.2}MnO_3$ poweder obtained by the modified Pechini's method", Journal of Ceramic Processing Research **12**, 102–105 (2011).

[124]M. L. Moreira, J. M. Soares, W. M. de Azevedo, A. R. Rodrigues, F. L. A. Machado, and J. H. de Araújo, "Structural and magnetic properties of nanoparticles of $La_{2/3}Sr_{1/3}MnO_3$ ", Physica B: Condensed Matter **384**, 51–53 (2006).

[125]M. H. Ehsani, P. Kameli, M. E. Ghazi, and F. S. Razavi, "An investigation on magnetic interacting $La_{0.6}Sr_{0.4}MnO_3$ nanoparticles", Advanced Materials Research **829**, 712–716 (2013).

[126]M. Kačenka, O. Kaman, Z. Jirák, M. Maryško, P. Žvátora, S. Vratislav, and I. Lukeš, "Magnetic properties of $La_{0.7}Sr_{0.3}MnO_3$ nanoparticles prepared in a molten salt", Journal of Applied Physics **115**, 17B525 (2014).

[127]H. Fujishiro, T. Fukase, and M. Ikebe, "Charge Ordering and Sound Velocity Anomaly in $La_{1-x}Sr_xMnO_3$ 3 ($x \geq 0.5$)", Journal of the Physical Society of Japan **67**, 2582–2585 (1998).

[128]M. Opel, "Spintronic oxides grown by laser-MBE", Journal of Physics D: Applied Physics **45**, 33001 (2011).

[129]J. B. Goodenough, "Theory of the role of covalence in the perovskite-type manganites [La,M(II)]MnO3", Physical Review **100**, 564–573 (1955).

[130]E. Pellegrin, L. H. Tjeng, F. M. F. de Groot, R. Hesper, G. A. Sawatzky, Y. Moritomo, and Y. Tokura, "Soft X-Ray magnetic circular dichroism study of the collosal magnetoresistance compound $La_{1-x}Sr_xMnO_3$ ", Journal of Electron Spectroscopy and Related Phenomena **86**, 115 (1997).

[131]S. Daengsakul, C. Thomas, I. Thomas, C. Mongkolkachit, S. Siri, V. Amornkitbamrung, and S. Maensiri, "Magnetic and cytotoxicity properties of $La_{1-x}Sr_xMnO_3$ ($0 \leq x \leq 0.5$) nanoparticles prepared by a simple thermal hydro-decomposition", Nanoscale Research Letters **4**, 839–845 (2009).

[132]V Laukhin, J Fontcuberta, J. L. García-Muñoz, and X Obradors, "Pressure effects on the metal-insulator transition in magnetoresistive manganese perovskites", Physical Review B **56**, R10009–R10012 (1997).

[133]V. Kusigerski, D. Markovic, V. Spasojevic, M. Tadic, M. Zentkova, and M. Mihalik, "Magnetic properties of nanoparticle $La_{0.7}Ca_{0.3}MnO_3$ under applied hydrostatic pressure", Journal of Nanoparticle Research **12**, 1299–1306 (2010).

[134]F. S. Razavi, G. Gross, H.-U. Habermeier, O. Lebedev, S. Amelinckx, G. Van Tendeloo, and A. Vigliante, "Epitaxial strain induced metal insulator transition in $La_{0.9}Sr_{0.1}MnO_3$ and $La_{0.88}Sr_{0.1}MnO_3$ thin films", Applied Physics Letters **76**, 155 (2000).

[135]J. M. D. Coey, M. Viret, and S. von Molnár, "Mixed-valence manganites", Advances in Physics **48**, 167–293 (1999).

[136]Y. P. Lee, S. Y. Park, V. G. Prokhorov, V. A. Komashko, and V. L. Svetchnikov, "Lattice-strain-driven ferromagnetic ordering in $La_{0.8}Sr_{0.2}MnO_3$ thin films", Applied Physics Letters **84**, 777 (2004).

[137]D. Louca, T Egami, E. L. Brosha, H Röder, and A. R. Bishop, "Local Jahn-Teller distortion in $La_{1-x}Sr_xMnO_3$ observed by pulsed neutron diffraction", Physical Review B **56**, R8475–R8478 (1997).

[138]A. Tebano, C. Aruta, S. Sanna, P. G. Medaglia, G. Balestrino, A. A. Sidorenko, R. De Renzi, G. Ghiringhelli, L. Braicovich, V. Bisogni, and N. B. Brookes, "Evidence of orbital reconstruction at interfaces in ultrathin $La_{0.67}Sr_{0.33}MnO_3$ Films", Physical Review Letters **100**, 137401 (2008).

[139]J. Heidler, C. Piamonteze, R. V. Chopdekar, M. A. Uribe-Laverde, A. Alberca, M. Buzzi, A. Uldry, B. Delley, C. Bernhard, and F. Nolting, "Manipulating magnetism in $La_{0.7}Sr_{0.3}MnO_3$ via piezostrain", Physical Review B **91**, 024406 (2015).

[140]A. Vailionis, H. Boschker, Z. Liao, J. R. A. Smit, G. Rijnders, M. Huijben, and G. Koster, "Symmetry and lattice mismatch induced strain accommodation near and away from correlated perovskite interfaces", Applied Physics Letters **105**, 131906 (2014).

[141] A. Pomar, J. Santiso, F. Sandiumenge, J. Oqueta, B. Bozzo, C. Frontera, L. Balcells, B. Martínez, and Z. Konstantinović, "Growth kinetics engineered magnetoresistance response in $La_{2/3}Sr_{1/3}MnO_3$ thin films", Applied Physics Letters **104**, 152406 (2014).

[142] X. Zhai, L. Cheng, Y. Liu, C. M. Schlepütz, S. Dong, H. Li, X. Zhang, S. Chu, L. Zheng, J. Zhang, A. Zhao, H. Hong, A. Bhattacharya, J. N. Eckstein, and C. Zeng, "Correlating interfacial octahedral rotations with magnetism in $(LaMnO_{3+\delta})N/(SrTiO_3)N$ superlattices.", Nature communications **5**, 4283 (2014).

[143] B. C. Behera, A. V. Ravindra, P. Padhan, and W. Prellier, "Raman spectra and magnetization of all-ferromagnetic superlattices grown on (110) oriented $SrTiO_3$", Applied Physics Letters **104**, 092406 (2014).

[144] S. Majumdar and S. van Dijken, "Pulsed laser deposition of $La_{1-x}Sr_xMnO_3$: thin-film properties and spintronic applications", Journal of Physics D: Applied Physics **47**, 034010 (2014).

[145] H. Boschker, J. Kautz, E. P. Houwman, W. Siemons, D. H. A. Blank, M. Huijben, G. Koster, A. Vailionis, and G. Rijnders, "High-temperature magnetic insulating phase in ultrathin $La_{0.67}Sr_{0.33}MnO_3$ films sub", Physical Review Letters **109**, 157207 (2012).

[146] A. De Léon-Guevara, P. Berthet, J. Berthon, F. Millot, A. Revcolevschi, A. Anane, C. Dupas, K. Le Dang, J. Renard, and P. Veillet, "Influence of controlled oxygen vacancies on the magnetotransport and magnetostructural phenomena in $La_{0.85}Sr_{0.15}MnO_{3-\delta}$ single crystals", Physical Review B **56**, 6031–6035 (1997).

[147] Z. Jirák, E. Hadová, O. Kaman, K. Knížek, M. Maryško, E. Pollert, M. Dlouhá, and S. Vratislav, "Ferromagnetism versus charge ordering in the $Pr_{0.5}Ca_{0.5}MnO_3$ and $La_{0.5}Ca_{0.5}MnO_3$nanocrystals", Physical Review B **81**, 024403 (2010).

[148] A. E. Teplykh, S. G. Bogdanov, E. Z. Valiev, A. N. Pirogov, Y. A. Dorofeev, A. A. Ostroushko, A. E. Udilov, and V. A. Kazantzev, "Size effect in nanocrystalline manganites $La_{1-x}A_xMnO_3$ with A=Ag, Sr", Physica B: Condensed Matter **350**, 55–58 (2004).

[149] A. Millis, "Lattice effects in magnetoresistive manganese perovskites", Nature **392**, 147–150 (1998).

[150] T Mizoroki, M Itou, Y Taguchi, T Iwazumi, and Y Sakurai, "Effects of hole doping in electronic states of $La_{1-x}Sr_xMnO_3$ probed by magnetic Compton scattering", Applied Physics Letters **98**, 52107 (2011).

[151] S. Solopan, O. V'yunov, A. Belous, T. Polek, and A. Tovstolytkin, "Effect of nanoparticles agglomeration on electrical properties of $La_{1-x}A_xMnO_3$ (A = Sr, Ba) nanopowder and ceramic solid solutions", Solid State Sciences **14**, 501–505 (2012).

[152] S. H. Monfared, G. Tang, X. Ma, and F. A. Mianji, "Nanostructure $La_{1-x}Sr_xMnO_3$ (x = 0.15 - 0.5) with improved metal-insulator performance", Materials and Manufacturing Processes, accepted Manuscript (2013).

[153] Y. Tokura, A. Urushibara, Y. Moritomo, T. Arima, A. Asamitsu, G. Kido, and N. Furukawa, "Giant magnetotransport phenomena in filling-controlled Kondo lattice system: $La_{1-x}Sr_xMnO_3$ ", Journal of Physical Society of Japan **63**, 3931–3935 (1994).

[154]C. Zener, "Interaction between the d-shells in the transition metals. II. Ferromagnetic compounds of manganese with Perovskite structure", Physical Review **82**, 403–405 (1951).

[155]A. J. Millis, P. B. Littlewood, and B. I. Shraiman, "Double exchange allone does not explain the Resistivity of $La_{1-x}Sr_xMnO_3$ ", Physical Review Letters **74**, 5144–5147 (1995).

[156]A. Sadhu and S. Bhattacharyya, "Enhanced low-field magnetoresistance in $La_{0.71}Sr_{0.29}MnO_3$ nanoparticles synthesized by the nonaqueous sol–gel route", Chemistry of Materials **26**, 1702–1710 (2014).

[157]V Markovich, I Fita, D Mogilyansky, A Wisniewski, R Puzniak, L Titelman, L Vradman, M Herskowitz, and G Gorodetsky, "Magnetic properties of nanocrystalline $La_{1-x}MnO_{3+\delta}$ manganites: size effects", Journal of Physics: Condensed Matter **19**, 346210 (2007).

[158]H. W. Eng, P. W. Barnes, B. M. Auer, and P. M. Woodward, "Investigations of the electronic structure of d0 transition metal oxides belonging to the perovskite family", Journal of Solid State Chemistry **175**, 94–109 (2003).

[159]P. A. Yadav, A. V. Deshmukh, K. P. Adhi, B. B. Kale, N. Basavaih, and S. I. Patil, "Role of grain size on the magnetic properties of $La_{0.7}Sr_{0.3}MnO_3$ ", Journal of Magnetism and Magnetic Materials **328**, 86–90 (2013).

[160]Y. F. Wang and H Yang, "Synthesis of different-sized $La_{0.7}Sr_{0.3}MnO_3$ nanoparticles via a polyacrylamide gel route and their magnetocaloric properties", Journal of Superconductivity and Novel Magnetism **26**, 3463–3467 (2013).

[161]Y. Tian, D. Chen, and X. Jiao, " $La_{1-x}Sr_xMnO_3$ (x=0,0.3,0.5,0.7) nanoparticles nearly freestanding in water: preparation and magnetic properties", Chemistry of Materials **18**, 6088–6090 (2006).

[162]H. M. Nguyen, D. H. Manh, L. V. Hong, N. X. Phuc, and Y. D. Yao, "Interacting Superparamagnetism in $La_{0.7}Sr_{0.3}MnO_3$ Nanoparticles", Journal of the Korean Physical Society **52**, 1447 (2008).

[163]T. Ahmad, K. Ramanujachary, S. E. Lofland, and A. K. Ganguli, "Reverse micellar synthesis and properties of nanocrystalline GMR materials ($LaMnO_3$, $La_{0.67}Sr_{0.33}MnO_3$ and $La_{0.67}Ca_{0.33}MnO_3$): ramifications of size considerations", Journal of Chemical Science **118**, 513–518 (2006).

[164]W. Lee, J. W. Han, Y. Chen, Z. Cai, and B. Yildiz, "Cation size mismatch and charge interactions drive dopant segregation at the surfaces of manganite perovskites.", Journal of the American Chemical Society **135**, 7909–7925 (2013).

[165]V. T. Dovgii, A. I. Linnik, S. Y. Prilipko, G. Y. Akimov, Y. F. Revenko, A. A. Novokhatskaya, T. A. Linnik, N. V. Davydeiko, V. N. Spiridonov, and A. V. Zhebel', "Magnetic properties of nanocrystalline $La_{0.52}Sr_{0.28}Mn_{1.2}O_3$", Inorganic Materials **47**, 1253–1257 (2011).

[166]I. Radelytskyi, P. Dłuzewski, V. Dyakonov, P. Aleshkevych, W. Kowalski, P. Jarocki, and H. Szymczak, "Magnetic anisotropy of $La_{0.7}Sr_{0.3}MnO_3$ nanopowders", Journal of Magnetism and Magnetic Materials **335**, 11–16 (2013).

[167]G. Venkataiah, Y. K. Lakshmi, V. Prasad, and P. V. Reddy, "Influence of Particle Size on Electrical Transport Properties of $La_{0.67}Sr_{0.33}MnO_3$ Manganite System", Journal of Nanoscience and Nanotechnology **7**, 2000–2004 (2007).

[168]J. Mera, M. Mera, C. Cordoba, O. Paredes, and O. Morán, " $La_{0.7}Sr_{0.3}MnO_3$ nanoparticles synthesized via the (Pechini) polymeric precursor method", Journal of Superconductivity and Novel Magnetism **26**, 2553–2556 (2013).

[169]K. G. Padmalekha and S. V. Bhat, "Contactless conductivity of nanoparticles from electron magnetic resonance lineshape analysis", Solid State Communications **150**, 1518–1520 (2010).

[170]G. Jonker and J. Van Santen, "Ferromagnetic compounds of manganese with perovskite structure", Physica **16**, 337–349 (1950).

[171]Moshnyaga, "Metal-Insulator Transition and Magnetoresistance in Manganite Thin Films: Lattice Strain and Disorder Effects", in *Frontiers in magnetic materials*, edited by A. V. Narlikar (Springer, Berlin Heidelberg, 2005), pp. 415–458.

[172]J. Curiale, R. D. Sánchez, H. E. Troiani, A. G. Leyva, and P. Levy, "Room-temperature ferromagnetism in $La_{2/3}Sr_{1/3}MnO_3$ nanoparticle assembled nanotubes", Applied Physics Letters **87**, 043113 (2005).

[173]N. Banerjee and S. B. Krupanidhi, "Anomalous magnetic behavior of $La_{0.6}Sr_{0.4}MnO_3$ nano-tubes constituted with 3-12 nm particles", Applied Physics A: Materials Science and Processing **111**, 605–612 (2013).

[174]A. Rostamnejadi, H. Salamati, P. Kameli, and H. Ahmadvand, "Superparamagnetic behavior of $La_{0.67}Sr_{0.33}MnO_3$ nanoparticles prepared via sol–gel method", Journal of Magnetism and Magnetic Materials **321**, 3126–3131 (2009).

[175]N. H. Nam, D. Thi, M. Huong, and N. H. Luong, "Synthesis and Magnetic Properties of Perovskite $La_{1-x}Sr_xMnO_3$ Nanoparticles", IEEE Transactions on Magnetics **50**, 3–6 (2014).

[176]J. A. Rodríguez, M. Fernández-García, J. A. Rodriguez, and M. Fernández-García, *Synthesis, Properties, and applications of oxide nanomaterials*, 1. (Wiley VCH, Hoboken, 2007), pp. 98–100.

[177]N. Grampurohit, P. Ravikumar, and R. Mallya, "Microemulsions for topical use - A review", Indian Journal of pharmaceutical education and research **45**, 100–107 (2011).

[178]K. J. Klabunde, R Richards, and J Kenneth, *Nanoscale materials in chemistry*, 2nd editio (Wiley-VCH, Hoboken, 2009), p. 165.

[179]S. Fridberg, "Microemulsions and micellar solutions", in *Microemulsions - theory and practice*, edited by L. Prince, 1. (Acadamic Press, New York, 1977) Chap. 6, pp. 133–148.

[180]B. L. Cushing, V. L. Kolesnichenko, and C. J. O´Connor, "Recent advances in the liquid-phase syntheses of inorganic nanoparticles", Chemical reviews **104**, 3893–3946 (2004).

[181]V. T. Liveri, *Controlled Synthesis of Nanoparticles in Microheterogeneous Systems*, edited by D. J. Lockwood, 1st ed. (Springer, New York, 2006), pp. 81–83.

[182]M. Lade, H. Mays, J. Schmidt, R. Willumeit, and R. Schomäcker, "On the nanoparticle synthesis in microemulsions: Detailed characterization of an applied reaction mixture", Colloids and Surfaces A: Physicochemical and Engineering Aspects **163**, 3–15 (2000).

[183]M. A. Malik, M. Y. Wani, and M. A. Hashim, "Microemulsion method: A novel route to synthesize organic and inorganic nanomaterials.", Arabian Journal of Chemistry **5**, 397–417 (2012).

[184]D. Makovec, A. Košak, and M. Drofenik, "The preparation of MnZn-ferrite nanoparticles in water–CTAB–hexanol microemulsions", Nanotechnology **15**, S160–S166 (2004).

[185]J. Wang, J. Fang, S. C. Ng, L. M. Gan, C. H. Chew, X. B. Wang, and Z. X. Shen, "Ultrafine barium titanate powders via microemulsion processing routes", Journal of the American Ceramic Society **82**, 873–881 (1999).

[186]V. Uskoković and M. Drofenik, "Four novel co-precipitation procedures for the synthesis of lanthanum-strontium manganites", Materials & Design **28**, 667–672 (2007).

[187]ChemicalBook Inc., *The chemical book - lanthanum nitrate hexahydrate*, 2014.

[188]National Center for Biotechnology Information, *PubChem Compound Database; CID=24821*.

[189]. Солопан, Еленич, Товстолыткин и. Белоус, " Влияниу особенностей синтеза наночастиц (La,Sr)MnO_3 на их свойства", Nanosystems, Nanomaterials, Nanotechnologies **12**, 189–198 (2014).

[190]R. B. Khomane and B. D. Kulkarni, "Nanoreactors for Nanostructured Materials", International Journal of Chemical Reactor Engineering **6**, A62 (2008).

[191]A. Holleman, E. Wiberg, and N. Wiberg, "Das Cobalt", in *Lehrbuch der anorganischen Chemie*, 102nd ed. (Walter de Gruyter & Co., Berlin, 2007), pp. 1682–1692.

[192]A. López-Trosell and R. Schomäcker, "Synthesis of manganite perovskite $Ca_{0.5}Sr_{0.5}MnO_3$ nanoparticles in w/o-microemulsion", Materials Research Bulletin **41**, 333–339 (2006).

[193]A. Holleman, E. Wiberg, and N. Wiberg, "Das Mangan", in *Lehrbuch der anorganischen Chemie*, 102nd ed. (Walter de Gruyter & Co., Berlin, 2007), pp. 1607 –1620.

[194]C. J. O. Connor, C. T. Seip, E. E. Carpenter, S. Li, and V. T. John, "Synthesis and reactivity of nanophase in reverse micellar solutions ferrites", Nanostructured Materials **12**, 65–70 (1999).

[195]H Kido and S Komarneni, "Preparation of $La_{1-x}Sr_xCoO_3$ (x=0.2,0.3) by two solution routes", SPIE **1307**, 1129–133 (1990).

[196]D. R. Sahu and B. K. Roul, "Synthesis of La0. 67Ca0. 33MnO3 Nanosized Powder Materials by Versatile Chemical Technique", Synthesis and Reactivity in Inorganic, Metal-Organic, and Nano-Metal Chemistry **38**, 329–334 (2008).

[197]S. A. Simakov and Y. Tsur, "Surface stabilization of nano-sized titanium dioxide: Improving the colloidal stability and the sintering morphology", Journal of Nanoparticle Research **9**, 403–417 (2007).

[198]Y Rabinovitch, C Bogicevic, F Karolak, D Tétard, and H Dammak, "Freeze-dried nanometric neodymium-doped YAG powders for transparent ceramics", Journal of Materials Processing Technology **199**, 314–320 (2008).

[199]J. Mouzon, M. Odén, O. Tillement, and Y. Jorand, "Effect of drying and dewatering on yttria precursors with transient morphology", Journal of the American Ceramic Society **89**, 3094–3100 (2006).

[200]A. Aman, Y. Chen, M. Lugovy, N. Orlovskaya, M. J. Reece, D. Ma, A. D. Stoica, and K. An, "In-situ neutron diffraction of $LaCoO_3$ perovskite under uniaxial compression. I. Crystal structure analysis and texture development sub", Journal of Applied Physics **116**, 013503 (2014).

[201]J. Rodriguez-Carvajal, "Recent developments of the program FULLPROF", CPD Newsletters **26**, 12–19 (2001).

[202]A. Guinier, *X-Ray Diffraction in crystals, imperfect crystals and amorphous bodies*, 2nd ed. (Dover Publications, Inc., New York, 1963), pp. 29–53.

[203]P. Scherrer, "Bestimmung der Größe und der inneren Struktur von Kolloidteilchen mittels Röntgenstrahlen", Nachrichten von der Gesellschaft der Wissenschaften zu Göttingen, Mathematisch-Physikalische Klasse **1918**, 98–100 (1918).

[204]A. L. Patterson, "The Scherrer formula for X-ray particle size determination", Phys. Rev. **56**, 978–982 (1939).

[205]B. Cullity, *Elements of X-Ray Diffraction*, 1. (Addison-Wesley Publishing Company, Reading, MA, 1956), pp. 259–260.

[206]G. K. Williamson and W. H. Hall, "X-ray line broadening from filed aluminium and wolfram", Acta Metallurgica **1**, 22–31 (1953).

[207]F. M. F. de Groot, "Multiplet effects in X-ray spectroscopy", Coordination Chemistry Reviews **249**, 31–63 (2005).

[208]I. Ascone, *X-ray absorption spectroscopy for beginners*, Madrid, 2011.

[209]F. M. F. De Groot, "X-ray absorption and dichroism of transition metals and their compounds", Journal of Electron Spectroscopy and Related Phenomena **67**, 529–622 (1994).

[210]K Küpper, "Electronic and magnetic properties of transition metal compounds: An x-ray spectroscopic study", Department of Physics, University Osnabrück (2005).

[211]G. V. D. Laan, "Applications of soft x-ray magnetic dichroism", Journal of Physics: Conference Series **430**, 012127 (2013).

[212]C. Kapusta, P. Fischer, and G. Schütz, "Magnetic X-ray absorption spectroscopy", Journal of Alloys and Compounds **286**, 37–46 (1999).

[213]J. Stöhr, H. A. Padmore, S. Anders, T. Stammler, and M. R. Scheinfein, "Principles of X-Ray Magnetic Dichroism Spectromicroscopy", Surface Review and Letters **05**, 1297–1308 (1998).

[214]G. Schütz, M. Knülle, and H. Ebert, "X-ray magnetic circular dichroism and its relation to local magnetic structures", in *Resonant anomalous x-ray scattering: theory and applications*, edited by G. Materlik, C. J. Sparks, and K. Fischer (North-Holland, Amsterdam, 1994), pp. 535–555.

[215]M. S. D. Read, M. Saiful Islam, G. W. Watson, F. King, and F. E. Hancock, "Defect chemistry and surface properties of $LaCoO_3$", Journal of Materials Chemistry **10**, 2298–2305 (2000).

[216]S. Chattopadhyay, N. V. Kulkarni, K. Choudhury, R. Prasad, A. Shahee, B. N. Raja Sekhar, and P. Sen, "Lattice expansion in ZnSe quantum dots", Materials Letters **65**, 1625–1627 (2011).

[217]L. I. Koroleva, D. M. Zashchirinskii, A. S. Morozov, and R. Szymczak, "Magnetocaloric effect in manganites", Journal of Experimental and Theoretical Physics **115**, 653–661 (2012).

[218]J. Kaczmarczyk, F. Zasada, J. Janas, P. Indyka, W. Piskorz, A. Kotarba, and Z. Sojka, "Thermodynamic Stability, Redox Properties, and Reactivity of Mn_3O_4, Fe_3O_4, and Co_3O_4 Model Catalysts for N_2O Decomposition: Resolving the Origins of Steady Turnover", ACS Catalysis **6**, 1235–1246 (2016).

[219]D. H. M. Buchold and C. Feldmann, "Microemulsion Approach to Non-Agglomerated and Crystalline Nanomaterials", Advanced Functional Materials **18**, 1002–1011 (2008).

[220]R. Bindu, "Structural studies of $La_{1-x}Sr_xMnO_{3+\delta}$ ($x = 0.1 - 1.0$)", European Physical Journal B **37**, 321–327 (2004).

[221]Y. Shirai, S. I. Hashimoto, K. Sato, K. Yashiro, K. Amezawa, J. Mizusaki, and T. Kawada, "Crystal structure and thermal expansion behavior of oxygen stoichiometric lanthanum strontium manganite at high temperature", Solid State Ionics **256**, 83–88 (2014).

[222]J. Dho and S. Ki, "Tetragonal lattice instability and monoclinic distortion in A-type antiferromagnetic $La_{0.4}Sr_{0.6}MnO_3$ manganites", Journal of Physics and Chemistry of Solids **75**, 1372–1375 (2014).

[223]O. Chmaissem, B. Dabrowski, S. Kolesnik, J. Mais, J. D. Jorgensen, and S. Short, "Structural and magnetic phase diagrams of $La_{1-x}Sr_xMnO_3$ and $Pr_{1-y}Sr_yMnO_3$", Physical Review B **67**, 094431 (2003).

[224]S.-P. Liu, Y. Xie, J. Xie, and G.-D. Tang, "Structural and magnetic properties of self-doped perovskite manganites $La_{0.8-x}Sr_{0.2}MnO_{3-\delta}$", Journal of Applied Physics **110**, 123714–123716 (2011).

[225]B. M. Nagabhushana, R. P. Sreekanth Chakradhar, K. P. Ramesh, C Shivakumara, and G. T. Chandrappa, "Low temperature synthesis, structural characterization, and zero-field resistivity of nanocrystalline $La_{1-x}Sr_xMnO_{3+\delta}$ ($0.0 \leq x \leq 0.3$) manganites", Materials Research Bulletin **41**, 1735–1746 (2006).

[226]N. Pérez, F. Bartolomé, L. M. García, J. Bartolomé, M. P. Morales, C. J. Serna, A. Labarta, and X. Batlle, "Nanostructural origin of the spin and orbital contribution to the magnetic moment in $Fe_{3-x}O_4$ magnetite nanoparticles", Applied Physics Letters **94**, 093108 (2009).

[227]C. Flipse, C. Rouwelaar, and F. de Groot, "Magnetic properties of CoO nanoparticles", The European Physical Journal D **9**, 479–481 (1999).

[228]V. L. Pool, C. Jolley, T. Douglas, E. A. Arenholz, and Y. U. Idzerda, "Orbital moment determination in $(Mn_xFe_{1-x})_3O_4$ nanoparticles", Journal of Applied Physics **109**, 07B532 (2011).

[229]C. Antoniak, J. Lindner, M. Spasova, D. Sudfeld, M. Acet, M. Farle, K. Fauth, U. Wiedwald, H. G. Boyen, P. Ziemann, F. Wilhelm, A. Rogalev, and S. Sun, "Enhanced orbital magnetism in Fe50Pt50 nanoparticles", Physical Review Letters **97**, 117201 (2006).

[230]R. Eder, "Spin-state transition in $LaCoO_3$ by variational cluster approximation", Physical Review B **81**, 035101 (2010).

[231]J.-Q. Yan, J.-S. Zhou, and J. B. Goodenough, "Ferromagnetism in $LaCoO_3$", Physical Review B **70**, 014402 (2004).

[232]G. Li, J. Boerio-Goates, B. F. Woodfield, and L. Li, "Evidence of linear lattice expansion and covalency enhancement in rutile TiO_2 nanocrystals", Applied Physics Letters **85**, 2059–2061 (2004).

[233]T. Tajiri, H. Deguchi, S. Kohiki, M. Mito, S. Takagi, K. Tsuda, and Y. Murakami, "Novel size effect of $LaMnO_{3+\delta}$ nanocrystals embeded in SBA-15 mesoporous silica", Journal of the Physical Society of Japan **75**, 113704 (2006).

[234]R. N. Bhowmik, R. Ranganathan, and R. Nagarajan, "Lattice expansion and noncollinear to collinear ferrimagnetic order in a $MnCr_2O_4$ nanoparticle", Physical Review B **73**, 144413 (2006).

[235]T. Tajiri, M. Harazono, H. Deguchi, M. Mito, A. Kohno, and S. Kohiki, "Synthesis and Magnetic Property of Multiferroic $BiMnO_3$ Nanoparticles in the Pores of Mesoporous Silica", Japanese Journal of Applied Physics **49**, 06GH04 (2010).

[236]T. Tajiri, N. Terashita, K. Hamamoto, H. Deguchi, M. Mito, Y. Morimoto, K. Konishi, and A. Kohno, "Size dependences of crystal structure and magnetic properties of $DyMnO_3$ nanoparticles", Journal of Magnetism and Magnetic Materials **345**, 288–293 (2013).

[237]J. Song, P. P. Rodenbough, L. Zhang, and S. W. Chan, "Size-Dependent Crystal Properties of Nanocuprite", International Journal of Applied Ceramic Technology **13**, 389–394 (2016).

[238]B. Roy and S. Das, "Size-induced metal insulator transition and glassy magnetic behavior in $La_{0.5}Sr_{0.5}CoO_3$ nanoparticles", Applied Physics Letters **92**, 233101 (2008).

[239]Z. Németh, A. Szabó, K. Knížek, M. Sikora, R. Chernikov, N. Sas, C. Bogdán, D. L. Nagy, and G. Vankó, "Microscopic origin of the magnetoelectronic phase separation in Sr-doped LaCoO3", Physical Review B **88**, 035125 (2013).

[240]P. Mondal, D. Bhattacharya, A. Maity, O. Chakrabarti, A. K. M. Maidul Islam, and M. Mukherjee, "Evolution of orbital phases with particle size in nanoscale stoichiometric LaMnO3", Journal of Applied Physics **109** (2011) 10.1063/1.3561365.

[241]A. Kalita and M. P. C. Kalita, "Size dependence of lattice parameters in ZnO nanocrystals", Applied Physics A **121**, 521–524 (2015).

[242]S. Khan, R. J. Oldman, F. Cora, C. R. A. Catlow, S. A. French, and S. A. Axon, "A computational modelling study of oxygen vacancies at $LaCoO_3$ perovskite surfaces", Physical Chemistry Chemical Physics **8**, 5207–5222 (2006).

[243]A. Zouari, C. Boudaya, and E. Dhahri, "Effect of the Oxygen Deficiency on the Structural, Magnetic and Electrical Properties in Perovskite-Like $La_{0.6}Sr_{0.4}MnO_3$", Physica Status Solidi (a) **188**, 1177–1186 (2001).

[244]S. V. Trukhanov, I. O. Troyanchuk, A. V. Trukhanov, I. A. Bobrikov, V. G. Simkin, and A. M. Balagurov, "Concentration-dependent structural transition in the $La_{0.70}Sr_{0.30}MnO_{3-\delta}$ system", JETP Letters **84**, 254 (2006).

[245]X. J. Liu, J. W. Li, Z. F. Zhou, L. W. Yang, Z. S. Ma, G. F. Xie, Y Pan, and C. Q. Sun, "Size-induced elastic stiffening of ZnO nanostructures: Skin-depth energy pinning", Applied Physics Letters **94**, 131902 (2009).

[246]S. Tsunekawa, S. Ito, T. Mori, K. Ishikawa, Z.-Q. Li, and Y. Kawazoe, "Critical size and anomalous lattice expansion in nanocrystalline $BaTiO_3$ particles", Physical Review B **62**, 3065–3070 (2000).

[247]X. Liu, Z. Chen, Y. Wen, R. Chen, and B. Shan, "Surface stabilities and NO oxidation kinetics on hexagonal-phase $LaCoO_3$ facets: a first-principles study", Catalysis Science and Technology **4**, 3687–3696 (2014).

[248]N. Iles, K. Driss Khodja, A. Kellou, and P. Aubert, "Surface structure and polarization of cubic and tetragonal $BaTiO_3$: An ab initio study", Computational Materials Science **87**, 123–128 (2014).

[249]S. Tsunekawa, K. Ishikawa, Z. Q. Li, Y. Kawazoe, and A. Kasuya, "Origin of anomalous lattice expansion in oxide nanoparticles", Physical Review Letters **85**, 3440–3443 (2000).

[250]C. Booth, F. Bridges, G. Kwei, J. Lawrence, A. Cornelius, and J. Neumeier, "Direct Relationship between Magnetism and MnO$_6$ Distortions in La$_{1-x}$Ca$_x$MnO$_3$ sub", Physical Review Letters **80**, 853–856 (1998).

[251]Y. Kobayashi and T. Mitsunaga, "Structural Phase Transition from Rhombohedral to Cubic in $LaCoO_3$", Journal of the Physical Society of Japan **69**, 3468–3469 (2000).

[252]E. Ino, K. Shimizu, and T. Yamate, "Studies on thermal decomposition process of lanthanum hydroxide", Journal of the Society of Materials Science, Japan **25**, 1165–1168 (1976).

[253]M. Méndez, Y. Cesteros, L. F. Marsal, A. Giguère, D. Drouin, P. Salagre, P. Formentín, J. Pallarès, M. Aguiló, F. Díaz, and J. J. Carvajal, "Effect of thermal annealing on the kinetics of rehydroxylation of Eu^{3+}:La_2O_3 nanocrystals", Inorganic Chemistry **51**, 6139–6146 (2012).

[254]. Шевченко, Башкиров и. Петров, " Термогравиметрические исследования высокотемпературных фазовых переходов в $LaCoO_3$ и твердых рассторах $La_{1-x}Nd_xCoO_3$, $La_{1-x}Gd_xCoO_3$", Vesci Nacyjanal'naj Akadmii Navuk Belarusi **1**, 5–8 (2007).

[255]J. Chang and E. Johnson, "Surface and bulk melting of small metal clusters", Philosophical Magazine **85**, 3617–3627 (2005).

[256]. Кондрашев и. Федорова, " Кристаллическая структура $CoHO_2$", Доклады Академии Наук СССР **19**, 229–231 (1954).

[257]T. Kohler, T. Armbruster, and E. Libowitzky, "Hydrogen Bonding and Jahn–Teller Distortion in Groutite, α-MnOOH, and Manganite, γ-MnOOH, and Their Relations to the Manganese Dioxides Ramsdellite and Pyrolusite", Journal of Solid State Chemistry **133**, 486–500 (1997).

[258]J. M. Pruneda, V. Ferrari, R. Rurali, P. B. Littlewood, N. A. Spaldin, and E. Artacho, "Ferrodistortive instability at the (001) surface of half-metallic manganites", Physical Review Letters **99**, 226101 (2007).

[259]L. Hu, C. Wang, R. M. Kennedy, L. D. Marks, and K. R. Poeppelmeier, "The role of oleic acid: From synthesis to assembly of perovskite nanocuboid two-dimensional arrays", Inorganic Chemistry **54**, 740–745 (2015).

[260]D. J. Morgan, A. E. Milodowski, S. S. Warne, and S. B. Warrington, "Atmosphere dependence of the thermal decomposition of manganite, γ-MnO.OH", Thermochimica Acta **135**, 273–277 (1988).

[261]C. González, J. I. Gutiérrez, J. R. González-Velasco, A. Cid, A. Arranz, and J. F Arranz, "Transformations of manganese oxides under different thermal conditions", Journal of Thermal Analysis **47**, 93–102 (1996).

[262]R. Pelosato, C. Cristiani, G. Dotelli, S. Latorrata, R. Ruffo, and L. Zampori, "Co-precipitation in aqueous medium of $La_{0.8}Sr_{0.2}Ga_{0.8}Mg_{0.2}O_{3-\delta}$ via inorganic precursors", Journal of Power Sources **195**, 8116–8123 (2010).

[263]M. Földvári, *Handbook of the thermogravimetric system of minerals and its use in geological practice*, Vol. 56, 4 (2011), p. 65.

[264]Z. Zeng, M. K. Y. Chan, Z. J. Zhao, J. Kubal, D. Fan, and J. Greeley, "Towards First Principles-Based Prediction of Highly Accurate Electrochemical Pourbaix Diagrams", Journal of Physical Chemistry C **119**, 18177–18187 (2015).

[265]H. Tagawa, J. Mizusaki, H. Takai, Y. Yonemura, H. Minamiue, and T. Hashimoto, "Oxygen hyperstoichiometry in perovskite-type oxide, undoped, and Sr-doped LaMnO3", in Proceedings of the 17th riso international symposium on materials science: high temperature electrochemistry: ceramics and metals, edited by F. Poulsen, N. Bonanos, S. Linderoth, M. Mogensen, and B. Zachau-Christiansen (1996), pp. 437–442.

[266]M.-J. Huang, "The electronic structure and magnetic interactions in the mixed transition-metal oxide $La(Co_Ni)O_3$ studied by x-ray absorption spectroscopies", PhD (Karlsruhe Institute of Technology, 2016).

[267]R. Nanguneri and H. Park, "Energetics of the spin-state transition in LaCoO3: Total energy calculations using DFT+DMFT", in Aps march meeting (2017).

[268]R. Prozorov, Y. Yeshurun, T. Prozorov, and A. Gedanken, "Magnetic irreversibility and relaxation in assembly of ferromagnetic nanoparticles", Physical Review B **59**, 6956–6965 (1998).

[269]W. A. Harrison, *Electronic structure and the properties of solids: The physics of the chemical bond*, 6th ed. (Dover Publications, New York, 1989).

[270]C. E. Hintze, D. Fuchs, M. Merz, A. Houari, C. Kübel, M.-J. Huang, A. Powell, and H. von Löhneysen, “Size-induced changes of structural and ferromagnetic properties in $La_{1-x}Sr_xMnO_3$ nanoparticles”, Journal of Applied Physics **121**, 214303 (2017).

[271]A. J. Millis, T. Darling, and A. Migliori, “Quantifying strain dependence in "colossal"magnetoresistance manganites”, Journal of Applied Physics **83**, 1588 (1998).